POLARIMETRIC MODELING OF DUAL FREQUENCY SAR DATA FOR CHARACTERIZATION OF THE LUNAR SURFACE
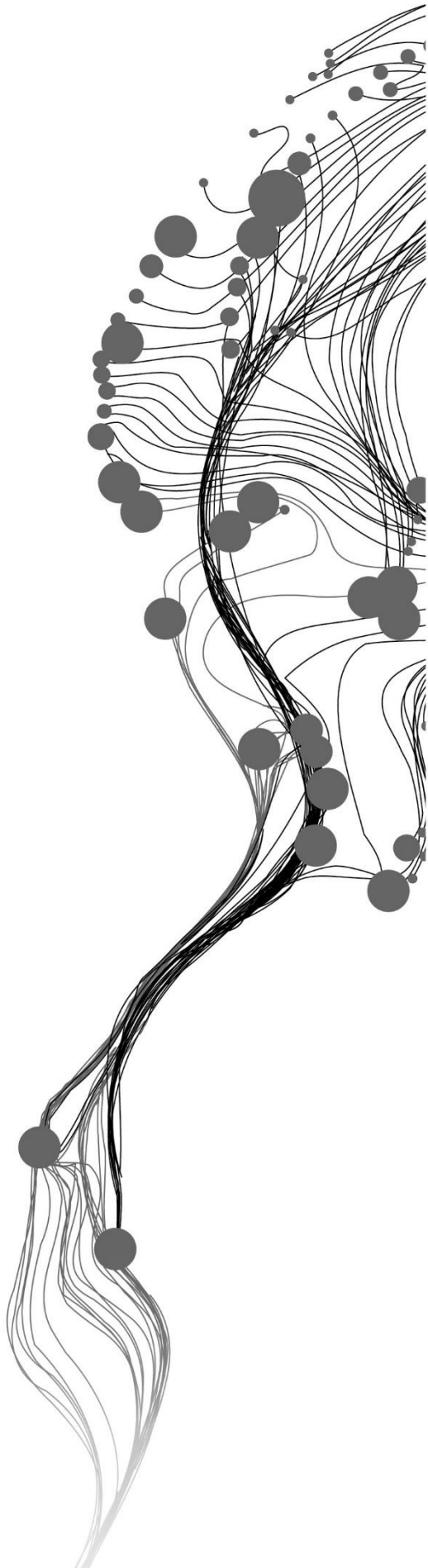
AWINASH SINGH
November, 2021

SUPERVISORS:
Dr Shashi Kumar, IIRS
Dr Ling Chang, ITC

POLARIMETRIC MODELING OF DUAL FREQUENCY SAR DATA FOR CHARACTERIZATION OF THE LUNAR SURFACE

AWINASH SINGH

Enschede, The Netherlands, November, 2021

Thesis submitted to the Faculty of Geo-Information Science and Earth Observation of the University of Twente in partial fulfilment of the requirements for the degree of Master of Science in Geo-information Science and Earth Observation.
Specialization: Geoinformatics

SUPERVISORS:
Dr Shashi Kumar, IIRS
Dr Ling Chang, ITC

THESIS ASSESSMENT BOARD:
Prof. Dr. Ir. A. Stein (Chair, ITC Professor)
Dr. Anup Das (External Examiner, Space Application Centre (SAC), Ahmedabad

ABSTRACT

Studies of the lunar surface from Synthetic Aperture Radar data have played a prominent role in the exploration of the lunar surface in recent times. This study utilizes the data of the three lunar missions Chandrayaan-1, Lunar Reconnaissance Orbiter (LRO) and Chandrayaan-2. The sensors present in these missions are Mini-SAR and Mini-RF which operates at S-band Hybrid polarimetric mode. The Mini-SAR of Chandrayaan-1 and Mini-RF of Lunar Reconnaissance Orbiter were the first to operate in S-band in Hybrid polarimetric mode whereas, the Dual Frequency Synthetic Aperture Radar (DFSAR) of Chandrayaan-2 mission and the Dual Frequency Synthetic Aperture Radar (DFSAR) is the first of its kind to operate at L-band and S-band and in a fully polarimetric mode. These are used to study the polarimetric characterization of the lunar crater Shackleton, Slater and Cabeus situated at South Pole on the moon and Hermite-A and Erlanger crater situated at the North Pole on the moon. These all craters lie in the Permanently Shadowed Region (PSR) of the lunar Sorth pole and North Pole. Because of its location within the PSR of the lunar polar region, these craters make an ideal candidate for containing water-ice deposits. This study also characterizes the Rimae Sulpicius Gallus which is a lunar rille which has pyroclastic deposits in its region. and the data used for this is of Mini-RF. This study uses Mini-RF data of Shackleton crater and Hermite-A crater, Mini-SAR data of Erlanger crater and Hermite-A crater, DFSAR data of Erlanger, Hermite-A, Cabeus and Slater crater. This study characterizes the scattering mechanisms from three decomposition techniques of Hybrid Polarimetry namely m-delta, m-chi and m-alpha decompositions and for fully polarimetric data Barnes decomposition technique was applied which is based on wave dichotomy. Eigenvector and Eigenvalue based decomposition model which H-A-Alpha decomposition was also applied to characterize the scattering behaviour of the craters. The Circular Polarization Ratio (CPR) also gave a constructive result in the crater as it showed the value to be more than unity in the craters. Identification of water-ice at the lunar polar craters can lead to future exploration of the lunar surface. Furthermore, in this study, the dielectric constant is also used to obtain the values of the dielectric constant by making use of the Gaussian model. The values of dielectric constant for Hermite-A crater from Chandrayaan-1 and LRO is similar which goes further in establishing the presence of water-ice in the region. Based on the results, it follows that the high volume scattering and high CPR, as well as the high values of dielectric constant, are caused by water-ice in the crater. The results give an interpretation of the regions which can be studied further for the identification of the lunar volatiles. It is recommended here that more in-depth analysis of other potential lunar regions be carried out, as these regions are likely to have mineral deposits, so that future manned missions can utilize these resources.

Keywords: Permanently Shadowed Region(PSR), L-band fully polarimetry; S-band hybrid polarimetry, Ice detection, lunar rille, North Pole, South Pole

Dedicated to my father…

Wherever you are in those stars.

ACKNOWLEDGEMENTS

TABLE OF CONTENTS

LIST OF FIGURES

LIST OF TABLES

1. INTRODUCTION

1.1. The Moon

Moon, the earth's only natural satellite, is the only place beyond our planet where human beings have set their footprints. Lunar surface has been predominantly of great interest because of the probable water in its regolith, in the form of water ice deposits and the research continuously being done in this area is a prime example of it(Bhattacharya et al., 2015; Meng et al., 2010; Vashishtha & Kumar, 2020).

Despite the lack of atmosphere on planets, meteorites persist constantly for millions and billions of years resulting in a layer of rubble and dust called regolith on the surface of planets. In terms of chemical properties, the regolith is similar to the nearby crater's crust, whereas in terms of its physical properties, its properties vary continuously due to impacts from micrometeorites and galactic cosmic radiation (GCR). Due to this, lava tube could be a potential site of future base settlement as these are the large subsurface channels through which once lava flowed and when lava discontinued flowing these conduit shaped tunnels resulted in the collapse of its roof emerging into a circular depression called skylights(Shukla et al., 2019; Vashishtha & Kumar, 2020). The lunar regolith contains various minerals which are present on different locations of the lunar surface. The minerals which are present in large amount are plagioclase, pyroxene, olivine, ilmenite, and spinel. The minerals which are present in less amount are cristobalite, apatite, and Iron (Fe), and Nickel (Ni)(Kumar & Kumar, 2014).

The continuous missions to the moon in the 21st century by several space agencies such as SELENE (commonly known as KAGUYA, Japan), Chang' e-1, 2, 3 and 4 (China), Lunar Reconnaissance Orbiter (LRO, USA), and Chandrayaan-1 & 2 (India) gives insightful information about the lunar surface and the finding of water in its surface is a boon to several upcoming missions. In the past few decades, there is a halt in particularly manned missions to the moon and to collect the samples but the intent of 'return to the moon' and Chang' e-5 (robotic sample return mission) gives us a hope to explore its surface that has been unexplored till now and more findings of water on the lunar surface will work as a catapult to several other space missions especially Mars and maybe future deep space missions. The presence of water in large quantities on the moon could be a dominant constituent in future missions as this can be used for drinking, cooling equipment, breathing, and making rocket fuel for future space missions.

1.2. Problem Statement and Motivation

Recent studies were done by Stratospheric Observatory for Infrared Astronomy (SOFIA) and Lunar Reconnaissance Orbiter (LRO) give an insight into the water on the sunlit moon and micro cold traps on the moon, respectively (Hayne et al., 2020; Honniball et al., n.d.). Remote sensing plays a pivotal role in providing information to the earth's surface as well as the planetary surfaces. Synthetic Aperture Radar (SAR) is not widely affected by atmospheric conditions and is prone to surface roughness, wavelength, moisture content, and dielectric properties which makes it the best possible way to study the lunar surface (Woodhouse, 2006). It was first suggested by Arnold about the possible sources of water ice at the lunar poles(Arnold, 1979). Due to the small angle of 5° in the rotation axis of the moon in relation to the ecliptic plane, where it is aligned to the ecliptic plane, most of the lunar poles are shadowed from solar radiation(Li et al., 2018). As a result of this, the surface temperatures in this region are very low and are the probable location of water ice. These areas are called as Permanently Shadowed Region (PSR) of the moon. Dielectric

characterization of the lunar surface especially the polar regions will give insightful information about the possible locations of water ice. Shackelton and Cabeus are two lunar south pole craters that were the impact site of two impact probe missions, Moon Impact Probe of the Chandrayaan-1(November 14, 2008) and Lunar Crater Observation and Sensing Satellite (LCROSS) of LRO (October 9, 2009), as there was some evidence of water in the ejecta of impact plume, gives the aspiration to explore these craters more and making these craters as a study area for this study (Colaprete et al., 2010; Sridharan et al., 2010). Along with them, the craters which are in the permanently shadowed region of the lunar poles i.e. north and south poles namely Hermite-A, Erlanger and Slater is also examined for the possible locations of water ice deposits in this study.

The data of Mini-SAR (Forerunner, S-band) and Mini-RF (S and X band) instruments of Chandryaan-1 and LRO respectively is used in this study. DFSAR (L and S-band) data of Chandrayaan-2 whose data was released recently is also be used in this study. By retrieving scattering patterns from SAR data and performing decomposition modeling, the geomorphological features can be studied and also determine their characteristics. Polarimetric SAR (PolSAR) can differentiate scattering elements in a single resolution cell. A target area is an area that contributes to three types of scattering patterns namely Surface scattering, double-bounce scattering, and volume scattering and a mixture of these scattering patterns give precise details about the physical properties of the target area. Temperature, mineral content, grain size, moisture, density, frequency, etc. are the factors that influence the electrical properties of a material. One of the most important electrical parameters of the lunar surface that provides basic data imperative for further exploration of the surface is the Dielectric constant, which can be calculated at microwave frequency using scattering coefficient (Calla OPN, Mathur Shubhra, 2014). As the real part of the dielectric constant value depends on the density of the medium, it will give better details about the constituent material of the surface. Due to this, as the real part of the dielectric constant increases, the Fresnel reflection coefficient increases, resulting in increased surface scattering. There is a decrease in penetration depth, so there is a decrease in radar energy passing through the surface, which, in turn, increases the dielectric difference between the lunar regolith and buried rocks. (Vashishtha & Kumar, 2020). Due to this, volume scattering decreases consequently. Thus, the physical features in this work is studied by evaluating scattering patterns by polarimetric decomposition techniques in combination with the dielectric constant values.

1.3. Research Objectives

The main objective of this work is to utilize the dual-frequency capability of PolSAR data for characterizing the dielectric behaviour of the regolith towards delineating the polar water ice in the permanently shadowed regions situated in the north and the south pole of the lunar surface.

1.3.1. Sub Objectives

1. To estimate Circular Polarization Ratio (CPR) value and analyze the scattering behaviour by various polarimetric decomposition techniques.
2. To compare different bands of SAR data to characterize the lunar regolith.
3. To examine the potential of Dual Frequency Synthetic Aperture Radar (DFSAR) of Chandrayaan-2(CH-2) for retrieving the polarimetric parameters of the lunar regolith.
4. To identify the possible locations of lunar rilles and to examine the capability of SAR data for surface characterization of the rilles.

1.3.2. Research Questions

The following research questions will be addressed.

        1.   Referring to sub-objective 1:

a.   What is the role of CPR in the identification of various ice deposits in the lunar craters present in the permanently shadowed region (PSR)?

b.   Which type of decomposition technique will give a detailed analysis of the characterization of the crater?

        2.   Referring to sub-objective 2:

a.   What are the different estimations of various bands to characterize the lunar regolith?

        3.   Referring to sub-objective 3:

a.   What is the role polarimetric parameters and the decomposition used in the L band?

        4. Referring to sub-objective 4:

a.   How is the identification of lunar rille take place and the role of CPR and decomposition technique in the surface characterization of the rille.

1.4.   Structure of Thesis

The thesis is divided into six chapters in total. Chapter 1 briefly discusses the introduction and the background of the work including the research objectives and the research questions. Chapter 2 gives the idea of the detailed description of the techniques involved in the work. Chapter 3 gives a detailed description of the study area and the datasets used in this work. Chapter 4 discusses the methodology used in this work. Chapter 5 explains the results derived from this work. Chapter 6 gives the conclusions of the work and recommendations which are deduced from the conclusions.

2. LITERATURE REVIEW

2.1. The Moon: A catapult in the future space missions

The moon, Luna (In Latin) the most fascinating and nearest celestial body which is the brightest and largest as seen in the clear night sky and the earth's only natural satellite whose distance is approximately 384,400 kilometres from earth, the only place outside our planet where human beings have reached and explored the surface (*In-Depth | Earth's Moon – NASA Solar System Exploration*, n.d.).Exploration of the lunar surface is quite interesting and profound to us in a lot of ways, but a question always arises to some of us, why the moon is important to us? The answer to this is thoroughly instructive as the moon is believed to be formed around 4.5 billion years ago when a mars size object, Theia hit the earth's surface and this event caused the birth of our Moon in this vast solar system. The moon's importance played a major role in its existence as it controlled the spin axis of earth from its gravity, at that time the earth's spin was much faster in comparison to the present day which was around 5 hours(Crawford, 2015). It is also believed that the moon and earth once shared the same magnetic field and must have lost it completely by 1.5 billion years ago (*Earth and Moon Once Shared a Magnetic Shield | NASA*, n.d.).

The existence and its evolution played a vital role in the existence of our planet as a large celestial body revolving around our planet made the orbit of the earth stable. Another role is of tidal effects that reduced the spin of the earth from 5 hours to around 24 hours as earlier our planet was spinning too fast. The most important is the lunar tides, from where the marine life from seas came into existence which in this case is the result of the origination of the life of the land, too (Crawford, 2015).

The moon is also a source of most of the mineralogical resources which can be used for future space missions as a good product of substitute of fuels that can be used for future deep space explorations and the colonization of mankind on the lunar surface(Bhandari & Srivastava, 2014). The recent findings of water ice content on its poles which is believed to be buried or mixed with the regolith and the water ice content findings apart from the poles also show a good hope in achieving our goals in near future and inching towards our desire for deep space exploration(Feldman et al., 2001; Hayne et al., 2020; Li et al., 2018; P. D. Spudis et al., 2013). The dependence on extraction of the minerals and the economic activity related to it has been limited to one planet. The use of lunar resources can be used for the exploration of the lunar surface and they can also be used for the scientific and the economic activity of both earth and moon as well as for the exploration of the other celestial bodies in the solar system. Recent studies talk about the potential resources on the lunar surface mainly solar wind implanted volatiles, Helium-3, water, oxygen, metals (platinum group metals), Iron and siderophile elements, titanium, aluminum, silicon, rare earth elements, thorium, and uranium (Bhandari & Srivastava, 2014). The continued exploration of the lunar surface will give a positive result in our goals that can be achieved soon.

2.1.1. Importance of the moon in the Indian space programme

The father of the Indian Space Programme, Dr. Vikram Sarabhai once said "There are some who question the relevance of space activities in a developing nation, to us there is no ambiguity of purpose" which is also relevant in the current scenario as India being the developing nation has come a long way in its space programme from its initial days of first rocket launch in 1963 to Chandryaan-2 in 2019, as well as going to the red planet, Mars in 2014 achieving its goal in the first attempt, a feat which was not accomplished by any other nation(Harvey et al., 2010). Chandrayaan-1, the first deep space exploration mission of the Indian space programme was initiated in 2008 making India one of the first developing nations to send its

orbiter to the moon to study topography, mineral, and chemical mapping of the lunar surface and search for water, too. The detection of water in the form of OH/H20 which was in abundance involving solar-wind interaction was a major achievement in this mission. The success of this mission leads to the exploration of other planetary bodies like Mars.

2.2.   Human footprints on the moon: The manned missions on the lunar surface

The thirst for exploring the lunar surface increased with the missions that were carried out in the earlier stage of exploration by different nations. Visiting the lunar surface, exploring and sample return to the earth increased the information about the lunar surface made a vast difference about the structure and geology of the lunar surface. The closeness of the moon made it possible to access the surface easily and continuously unlike any other deep-space destination. The first manned mission that was carried out in 1968 was Apollo-8, which was a crewed orbiter mission and the last was of the same era, Apollo 17 which was a crewed lander mission in 1972. There is a halt in the manned mission for almost 5 decades, but with the Artemis missions, return to the moon will be accomplished in the coming years.

Table 1 Apollo Series Description(*The Apollo Missions | NASA*, n.d.)

Mission Name	Launch Date & Landing Site	Objectives
Apollo 8	December 21, 1968	Illustrate command and service module performance in cislunar and lunar orbit. Demonstrate communications, tracking lunar distances and photographs of the proposed landing site.
Apollo 9	March 3, 1969	Test lunar module, spacecraft launch, and vehicle adapter, demonstrate extravehicular activity (EVA), and perform system functions.
Apollo 10	May 18, 1969	Verification of lunar module system in the lunar environment, refinement of the lunar gravitational potential.
Apollo 11	July 16, 1969, & Mare Tranquillitatis	Observe properties of lunar regolith, EVA to collect samples, and science experiments to investigate soil mechanics, solar winds, passive seismic, lunar dust detector, lunar surface magnetometer.
Apollo 12	November 14, 1969, & Ocean of Storms	Deploy the Apollo Lunar Surface Experiments Package (ALSEP), selenological inspection, surveys, and samplings in landing areas, development of techniques for precision-landing capabilities, further evaluations of the human capability to work in the lunar environment for a prolonged period.
Apollo 14	January 31, 1971 & Fra Mauro	Lunar field geology investigations, collection of surface material samples for return to Earth, communications tests using S-band and VHF signals to determine reflective properties of the

		lunar surface, tests to determine variations in S-band signals
Apollo 15	July 26, 1971, & Hadley-Appennius	Perform selenological inspections, surveys, and sampling of materials and surface features of the landing site.
Apollo 16	April 16, 1972 & Descartes formation	Perform geological inspection, survey, and sampling of materials and surface features in the landing site, to emplace and activate surface experiments, and to conduct inflight experiments and photographic tasks
Apollo 17	December 7, 1972	Obtain samples of highland material that were older than the Imbrium impact, heat flow experiment; lunar seismic profiling, or LSP; lunar surface gravimeter, or LSG; lunar atmospheric composition experiment, or LACE; and lunar ejecta and meteorites, or LEAM.

2.3. The chronicle of lunar exploration: Lander, Orbiter, and Impactor

The interest in exploring the Luna dates back to the first telescopic observation in August 1609, by an Englishman Thomas Harriott which was followed by Galileo in 1610. Earlier many speculations were regarding the Moon that it has life, oceans and the composition of the lunar surface is rhyolite which was still believed in the early 20th century until the exploration of the lunar surface by making observations, collecting the samples, and doing analyses on the returned samples that were collected in the Apollo era. This lead to a detailed understanding of our nearest celestial body. The first mission that was carried out was Luna-1 by the Soviet Union on January 3, 1959, which was a flyby mission in which it was discovered that the lunar surface does not have any global magnetic field. Luna-9 in 1969 became the first mission in which a spacecraft landed on any celestial body, before this the missions that were carried out were only flyby or impactors. The recent mission to the moon was of Chang'e-5 by China in November 2020 in which the samples were collected after around 44 years, the last being in 1976 by Luna-24. The description of all the moon missions is shown in Table 2. The urge to explore the lunar surface is never ending as the upcoming missions by different nation is a prime example of it. There is no need for any space race if we can go hand in hand to achieve some good results for mankind.

2.3.1. Description of Moon missions

Table 2 Lunar Exploration Timeline (Credits-Lunar and Planetary Institute)

MISSION NAME	LAUNCH TIME	OPERATION MODE
Luna 1	Jan 2, 1959	Flyby
Pioneer 4	Mar 3, 1959	Flyby
Luna 2	Sep 12, 1959	Impact
Luna 3	Oct 4, 1959	Probe
Ranger 1	Aug 23, 1961	Attempted Test Flight
Ranger 2	Nov 18, 1961	Attempted Test Flight
Ranger 3	Jan 26, 1962	Attempted Impact

Ranger 4	Apr 23, 1962	Impact
Ranger 5	Oct 18, 1962	Attempted Impact
Luna 4	Apr 2, 1963	Flyby
Ranger 6	Jan 30, 1964	Impact
Ranger 7	Jul 28, 1964	Impact
Ranger 8	Feb 17, 1965	Impact
Ranger 9	Mar 21, 1965	Impact
Luna 5	May 9, 1965	Impact
Luna 6	Jun 8, 1965	Attempted Lander
Zond 3	Jul 18, 1965	Flyby
Luna 7	Oct 4, 1965	Impact
Luna 8	Dec 3, 1965	Impact
Luna 9	Jan 31, 1966	Lander
Luna 10	Mar 31, 1966	Orbiter
Surveyor 1	May 30, 1966	Lander
Lunar Orbiter 1	Aug 10, 1966	Orbiter
Luna 11	Aug 24, 1966	Orbiter
Surveyor 2	Sep 20, 1966	Attempted Lander
Luna 12	Oct 22, 1966	Orbiter
Lunar Orbiter 2	Nov 6, 1966	Orbiter
Luna 13	Dec 21, 1966	Lander
Lunar Orbiter 3	Feb 4, 1967	Orbiter
Surveyor 3	Apr 17, 1967	Lander
Lunar Orbiter 4	May 8, 1967	Orbiter
Surveyor 4	Jul 14, 1967	Attempted Lander
Lunar Orbiter 5	Aug 1, 1967	Orbiter
Surveyor 5	Sep 8, 1967	Lander
Surveyor 6	Nov 7, 1967	Lander
Surveyor 7	Jan 7, 1968	Lander
Luna 14	Apr 7, 1968	Orbiter
Zond 5	Sep 15, 1968	Return Probe
Apollo 7	Oct 11, 1968	
Zond 6	Nov 10, 1968	Return Probe
Apollo 8	Dec 21, 1968	Crewed Orbiter
Apollo 9	March 3, 1969	Crewed Orbiter
Apollo 10	May 18, 1969	Orbiter
Luna 15	Jul 13, 1969	Orbiter
Apollo 11	Jul 16, 1969	Crewed Lander
Zond 7	Aug 7, 1969	Return Probe
Apollo 12	Nov 14, 1969	Crewed Lander

Apollo 13	Apr 11, 1970	Crewed Lander (aborted)
Luna 16	Sep 12, 1970	Sample Return
Zond 8	Oct 20, 1970	Return Probe
Luna 17/Lunokhod 1	Nov 10, 1970	Rover
Apollo 14	Jan 31, 1971	Crewed Lander
Apollo 15	Jul 26, 1971	Crewed Lander
Luna 18	Sep 2, 1971	Impact
Luna 19	Sep 28, 1971	Orbiter
Luna 20	Feb 14, 1972	Sample Return
Apollo 16	Apr 16, 1972	Crewed Landing
Apollo 17	Dec 7, 1972	Crewed Landing
Luna 21/Lunokhod 2	Jan 8, 1973	Rover
Luna 22	Jun 2, 1974	Orbiter
Luna 23	Oct 28, 1974	Lander
Luna 24	Aug 14, 1976	Sample Return
Hiten	Jan 24, 1990	Flyby, Orbiter, and Impact
Clementine	Jan 25, 1994	Orbiter
AsiaSat 3/HGS-1	Dec 24, 1997	Lunar Flyby
Lunar Prospector	Jan 7, 1998	Orbiter and Impact
SMART 1	Sep 27, 2003	Orbiter
Kaguya (SELENE)	Sep 14, 2007	Orbiter
Chang'e 1	Oct 24, 2007	Orbiter
Chandrayaan-1	Oct 22, 2008	Orbiter
Lunar-A	Cancelled	Orbiter and Penetrators
LRO	Jun 18, 2009	Orbiter
LCROSS	Jun 18, 2009	Impact
Chang'e 2	October 1, 2010	Orbiter
ARTEMIS	2010	Orbiter
GRAIL	September 8, 2011	Orbiter
Chang'e 3	December 1, 2013	Lander and Rover
LADEE	May 2, 2013	Orbiter
Delta IV-Orion (EFT-1)	September, 2014	Orbiter
SLS-Orion (EM-1)	2017	Orbiter
Constellation Altair Lander (cancelled)	2018	Lander
SELENE-2 (cancelled)	2018	Orbiter and Lander with Rover
Chang'e 4	May 20, 2018	Lander and Rover
Chandrayaan-2	2019	Orbiter and Lander
Chang'e 5	2019	Sample Return

2.3.2 Future Lunar Missions
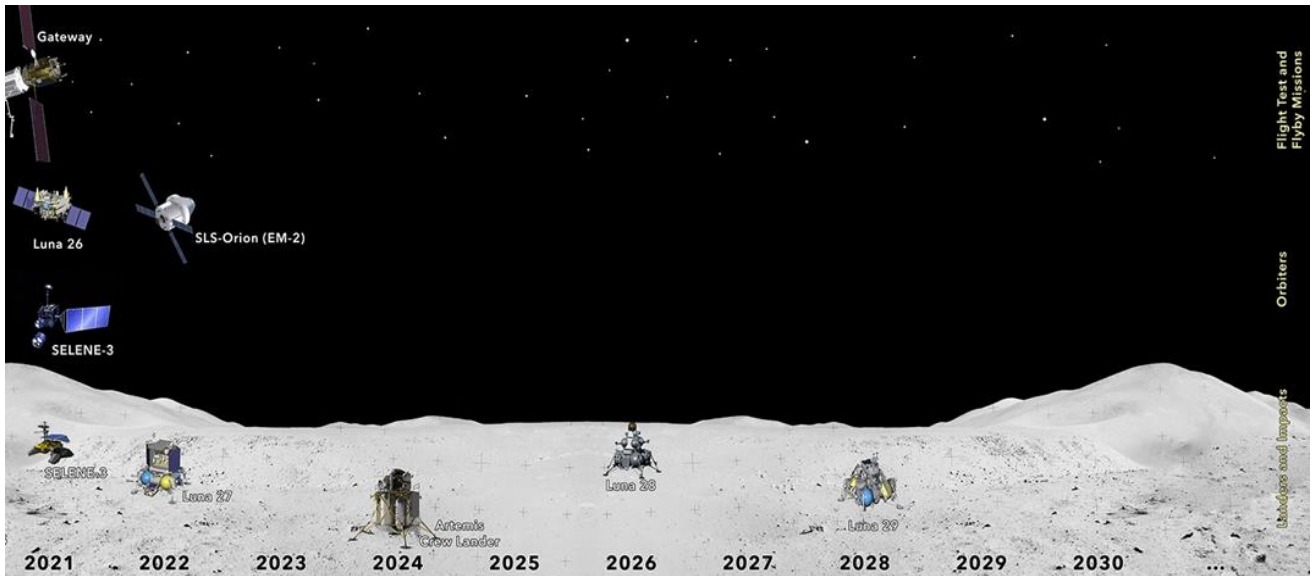
Figure 1 Future Lunar Missions (Credits-LPI)

Lunar exploration in the future will leap deep space exploration. Space agencies of various countries are actively participating in the exploration of the lunar surface like USA, Russia, China, India, Japan and South Korea by planning to send their probe which includes orbiter, lander, rover or sample return mission. The crewed mission is also panned after almost five decades from NASA for their Artemis- 3 mission which is panned in 2024. The detailed description of the future lunar mission is explained in Table 3 and an interpretation of future lunar missions is shown in Figure 1.

Table 3 Future Lunar Missions (Credits-NASA-NSSDC & LPI)

Name	Country & Agency	Expected Launch Date	Nature of Mission
Artemis 1	U.S.A & NASA	16 December, 2021	Orbiter
CAPSTONE	U.S.A & NASA	2021	Orbiter
Peregrime Mission-1	U.S.A & NASA	2021	Lander
Luna-25	Russia & Roscosmos	2021	Lander
IM-1	U.S.A & NASA	2021	Lander
LunaH-MAP	U.S.A & NASA	2021	Orbiter
Lunar FlashlIght	U.S.A & NASA	2021	Orbiter
Lunar Ice Cube	U.S.A & NASA	2021	Orbiter
LunIR	U.S.A & NASA	2021	Orbiter
Cislunar Explorers	U.S.A & NASA	2021	Orbiter
OMOTENASHI	Japan & JAXA	2021	Lander
EQUULEUS	Japan & JAXA	2021	Orbiter
SLIM	Japan & JAXA	2022	Lander
Korea Pathfinder Lunar Orbiter	South Korea & KARI	2022	Orbiter
Prime-1	U.S.A & NASA	2022	Lander

Chandrayaan-3	India & ISRO	3rd Quarter, 2022	Lander
XL-1 Lander	U.S.A & NASA	2023	Lander
VIPER	U.S.A & NASA	2023	Rover
Artemis-2	U.S.A & NASA	September,2023	Orbiter
Change'e-6	China & CNSA	2023-24	Lander, Orbiter, Sample return
Lunar Trailblazer	U.S.A & NASA	2024	Orbiter
Artemis-3	U.S.A & NASA	2024	Crewed Lander Mission
Luna-26	Russia & Roscosmos	Expected 2024	Orbiter
Chang'e-7	China & CNSA	Expected 2024	Lander, Orbiter, Rover, Sample return
Luna-27	Russia & Roscosmos, European Space Agency	2025	Lander
Luna-28	Russia & Roscosmos	2026	Lander
Chang'e-8	China & CNSA	TBD	Unknown
Luna-29	Russia & Roscosmos	2028	Lander

2.4. Lunar Surface

2.4.1. Crater Formation

Impact craters usually occur to all the celestial bodies which are solid surfaces in nature that are present in the solar system. Earth has a thick atmosphere, however, so meteoroids that enter the atmosphere are blasted off due to friction generated by the Earth's gravity when they enter(Koeberl, 2004). An impact crater is formed when energy is instantly transferred from the impactor to the target. As two bodies in a solar system approach each other at high velocity, kinetic energy is provided from the relative orbital motion of the colliding bodies and gravitational energy from the gravitational field. The impact craters can be much larger because of the collision that can be very energetic. On the moon, the only geological activity that takes place is impact cratering.

2.4.1.1. Types of Craters

The craters can be divided into four classes based on their morphology namely Micro craters or pits, Small or simple craters, large craters, and Multi ring basins. Micro craters or pits craters are formed when micrometeoroids or high-velocity cosmic dust grains may cause these craters at the sub-centimetre scale on rocky surfaces. In these craters, the centre is covered with glass and is found on astronomical bodies which do not have an atmosphere. Small or simple-shaped craters are those whose depth is approximately one-fifth of their diameter, and these craters are in bowl-shaped structures. Large craters are also called complex craters because of their structures. These crater's base area is smooth but there is a peak in its centre and the rim looks like a terrace. The diameter of these craters is from a few tens to a few hundred kilometres. In Multi ring basins, these craters cover a much larger area than the large craters as it is made up of several concentric circles and the inner ring has a hill (Jozwiak et al., 2012).

2.4.2. Lunar Pyroclastic Deposits

The pyroclastic deposits are the evident source of the early volcanism in lunar history and have metal oxides and volatiles which can be used in the future. In total, there are more than 100 mapped regions of the pyroclastic deposits on the lunar surface, and some of their range to an extent of 49,000 square km (L. M. Carter et al., 2009; Gaddis et al., 2003). They are generally related to the mare boundaries, volcanism centres, and the fractures which lie in the impact craters (L. M. Carter et al., 2009). Lunar pyroclastic deposits can be classified into two types namely Localised Dark Mantling Deposits and Regional Dark Mantling Deposits (RDMDs). The Localised Dark Mantling Deposit are related to endogenic dark haloed craters. These pyroclastic deposits are divided into three classes. Class 1 consists of highlands materials with minor olivine and volcanic glass. Class 2 is made up of fragmented mare basalts and Class 3 is of mafic materials in which olivine and pyroxene are in abundance(Lawrence & Hawke, 2008). The RDMDs are comprised of picritic glasses of volcanic origin(Lawrence & Hawke, 2008; Shearer & Papike, 1993) Based on spectral data, RDMDS are also categorized into two types. The glasses which show Fe2+ are one of the types and its example is Aristarchus Plateau (Figure 2a). The ilmenite-rich black beads or spheres of the pyroclastic region are of the second type and its example is Apollo 17 site which is the Taurus Littrow valley(Gaddis et al., 1985). The other examples include Rima Bode (Figure 2b), and Southern Mare Vaporum regions. The age of the Apollo 17 landing site which is the Taurus-Littrow valley lies back to 3.48- 3.66 Ga ago(L. M. Carter et al., 2009). Ferrous Ion (Fe2+) which are of volcanic glass beads and/or black crystallized beads were found at the Taurus Littrow, Aristarchus, and Sulpicius Gallus. The Apollo landing site also has orange glasses and crystallized beads. The pyroclastic deposits have various resource possibilities as they can be used for future lunar outposts as they are fine-grained and boulder-free. So, it will be time effective and cost-effective for the machinery. It is also stated in various studies that these deposits can also be used for producing oxygen. Other resources also include volatiles from the solar wind implanted such as H, He, He-3, C, and other noble gases which could be used for life support materials and other agricultural activities(Chin et al., 2007; Lawrence & Hawke, 2008).

(a)   (b)
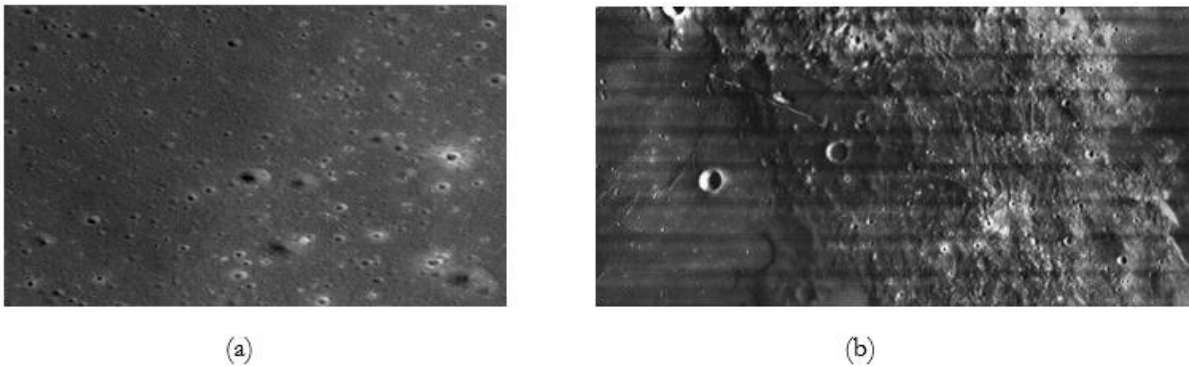
Figure 2 Lunar Pyroclastic Deposit (a) Aristarchus Plateau (b) Rima Bode (Credits-NASA/Goddard/Arizona State University/ USGS Astrogeology Science Center)

2.4.3. Lunar Rilles

The lunar surface comprises several geological structures apart from the craters which include lunar rilles. The rilles are also called Rima in Latin and its plural is Rimae. These rilles look like dried riverbeds and they are categorized into three types namely Sinuous, Straight, and Arcuate (*Rilles and Rilles: Sinuous, Straight, and Arcuate | Lunar Reconnaissance Orbiter Camera*, n.d.). The Sinuous rilles are considered to be formed by the collapsed lava tubes and it appears as a meandering river. A magma source region on the mantle would likely have created these depressions when magma reached the surface. Earlier it was considered that these channel-like features have been created by the surface or subsurface erosion of flowing water or erosion by ash flows or collapsed lava tubes or the intersection of fracture patterns. But now the better assumption is that its formation is because of the lava flow and erosion from the collapsed lava tubes(Hurwitz et al., 2013). The sinuous rille is the most common rille type feature that is found on the lunar surface. Figure 3 (a) shows an example of a Sinuous Rille which is Rima Sharp, its rille length is around 276 km. The second type is of Straight rilles which are formed by the tectonic forces. A valley floor is formed when a block of crust descends to the valley floor like the surface of the crust separates under extensional forces which are called graben. The largest straight rille is found in the Oceanus Procellarum, also known as Ocean of Storms situated on the near side which is known as Rima Sirsalis, and stretches to 400 km(*Rilles and Rilles: Sinuous, Straight, and Arcuate | Lunar Reconnaissance Orbiter Camera*, n.d.). Figure 3(b) shows an example of a Straight rille which is Rima Cauchy. The Arcuate rille is of the third type which is formed along the margins of maria within some basins as curved formations, similar to parentheses or bows (without the arrows). The Arcuate rilles are likely the result of mare basalts sagging toward the center, causing the edges to pull apart. Because of this, the rille closely resembles the circular shape of the basin (*Rilles and Rilles: Sinuous, Straight, and Arcuate | Lunar Reconnaissance Orbiter Camera*, n.d.). Figure 3(c) shows an example of arcuate rille which is Rimae Sulpicius Gallus and its total rille length is around 80 km.
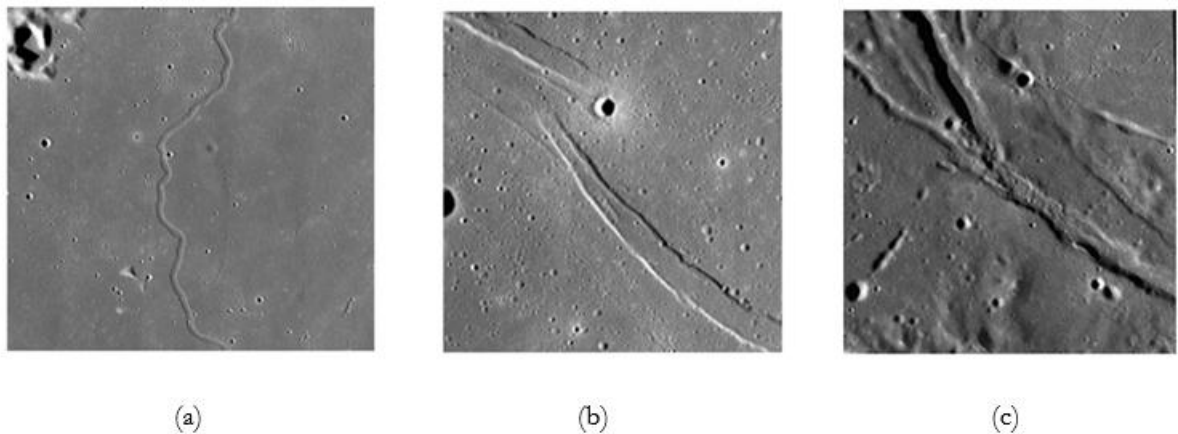
Figure 3 Lunar Rilles (a) Sinuous Rille- Rima Sharp (b) Straight Rille-Rima Cauchy (c) Arcuate Rille-Rimae Sulpicius Gallus (Credits-NASA, GSFC, Arizona State University)

2.5.   The new era of SAR based missions for the lunar surface.

2.5.1.   Chandrayaan-1

Chandrayaan-1's mission of the Indian Space research Organisation took place in 2008 and consisted of several payloads which included Mini-SAR as well. The major scientific objective of this instrument was to detect water ice in the PSRs on the lunar poles up to the depth of few meters (Bhandari & Srivastava, 2014). Mini-SAR used S-band and has a wavelength of 12.6 cm and has incidence angle of 35°. The spatial resolution of the image strips is 75 meters per pixel(L. Carter et al., 2009). Preliminary results that were concluded from Mini-SAR were that the CPR values in the north polar regions were in the range of 0.1-0.3. A group of craters was identified that showed a high CPR value between 0.6- 1.7 in the interior of the crater, but it was less in the exterior of the rim of the crater, which was around 0.2 - 0.4. In South Pole Aitken basin, the massifs which make the rim of the basin showed high CPR. The small craters of south pole namely Shoemaker and Faustini showed high CPR value, too. Apart from the non-polar regions that showed high CPR value were Sulpicius Gallus which has fine grained pyroclastic deposits near it. The craters such as Aratus and Aristarchus which are considered to be fresh craters have high CPR values. The average combined CPR of mare and highland terrain is ~0.32 ± 0.11(P. D. Spudis et al., 2013).

2.5.2.   Lunar Reconnaissance Orbiter (LRO)

The LRO was launched in 2009 and a developed version of the SAR instrument of Chandrayaan-1 mission was on board i.e., Mini-RF. Mini-RF instrument has a hybrid polarimetry architecture operating at two bands i.e., S and X band whose wavelength is 12.6 cm and 4.2 cm, respectively. It focuses on the lunar poles that were unexplored earlier for the possible locations of ice deposits, volatile, impact, and volcanic processes on the moon. It has also mapped the PSR of the lunar poles for the polar volatiles (Vondrak et al., 2010). It has also mapped the roughness of the lunar surface and it can see the ejecta that is not visible in the optical images. The major science objective of Mini-RF is that the vertical distribution of water; the form and abundance of water ice; how impacts expose and break down rocks to produce regolith on the Moon and other airless bodies; the present rate of regolith gardening; and how lunar volcanism has evolved (Sriram Saran Bhiravarasu et al., 2020).

2.5.3.   Chandrayaan-2

The DFSAR instrument aboard Chandryaan-2 is a dual-frequency monostatic system and operating at L band (24 cm) and S-band (12 cm) at an altitude of 100 km. One of the main features of this radar sensor is, it is the first L band polarimetric SAR which is utilized for the lunar studies, which will be used for deeper penetration into the regolith and it is also the first fully polarimetric SAR to orbit the moon. The instrument can also acquire imaging in single, dual, and hybrid- circular polarimetry and the resolution capacities from 2m to 75m in the slant range with incidence angles ranging from 9.6° to 36.9°(Patterson et al., 2020; Putrevu et al., 2020a). The fully polarimetric mode in this aims for unambiguous detection and the characterization and quantitative estimation of the water-ice in the permanently shadowed region of the lunar poles.

The DFSAR will also address the ambiguities detected in depicting high values of the circular polarization ratio (CPR) for water ice that was found in the earlier missions which were caused by the surface roughness. The advantage of full-polarimetric data over any arbitrary polarization state like circular, linear, and hybrid modes is that it contains more scattering information. Chandrayaan-2 DFSAR data with different incident angles 10° and 35°, steep and moderate respectively can be used to calculate the surface roughness of the regolith. The configuration of DFSAR is shown in Fig. 4 "The major scientific objectives of the DFSAR instrument are (a) Detection and estimation of water–ice deposits in the permanently shadowed regions of the moon, using dual-frequency and full-polarimetric imaging at multiple viewing angles. (b) Regolith dielectric constant and surface roughness estimation over the lunar surface using multi-frequency data. (c)

Investigation of geo-morphological features especially in the polar regions and preparation of geomorphological maps and high-resolution crater floor maps. (d) Quantitative estimation of regolith thickness and distribution over selected regions using data from dual-frequency radiometer mode"(Putrevu et al., 2015, 2020b).
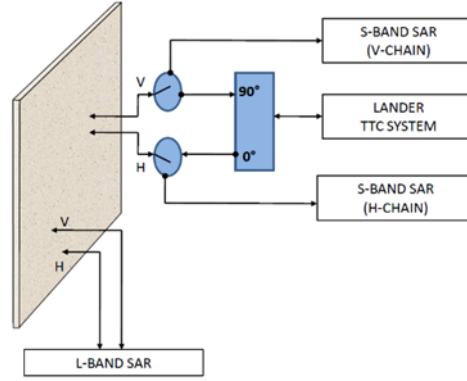
Figure 4 Chandrayaan-2 DFSAR configuration with lander communication system

2.6. Dielectric Constant

For this study, the dielectric constant is defined as a surface's response to an incident EMR, which is primarily in the microwave band. The attenuation factor for this is defined mathematically and expressed as shown in eq. 16

$$a = \exp(4\pi f \epsilon^{ll} d / c \sqrt{\epsilon^{l}}) \tag{1}$$

Where,

a= attenuation factor

f = frequency of the incident electromagnetic wave,

c = the velocity of the electromagnetic wave,

d = the thickness of the surface is denoted

and

the complex dielectric constant is $\epsilon = \epsilon' - i\epsilon''$.

The real part of a target surface's dielectric constant is just a density of the medium parameter, which is shown in the following equations 2 and 3 (Fa et al., 2011)

$$\epsilon' = (1.93 \pm 0.17)^{\rho} \tag{2}$$

$$\tan \delta = 10^{0.038S + 0.312\rho - 3.260} \tag{3}$$

ρ = density of the target medium in gm/cm^3 and S = $FeO+TiO_2$ is in wt.%.

The detailed equation parameters are derived in(Vashishtha & Kumar, 2020)

2.7. Backscatter Modelling of Radars

Based on a variety of factors such as dielectric constant, surface roughness, the wavelength of electromagnetic radiation, frequency of electromagnetic radiation, incidence angle, and type of polarization, backscatter energy can be computed. Radar backscatter coefficients are difficult to use to determine the dielectric constant. As a result, separating the contributions of each of these components and determining the value of each factor is difficult.

Using any inversion approach, any parameter, such as the dielectric constant here, can be retrieved from the equations of theoretical empirical models after generating enormous datasets from the equations. The Kirchhoff Model, the Small Perturbation Model, and the Integral Equation Model (IEM) are just a few of the electromagnetic backscattering models available for generating simulated data. The range of roughness, which differs among different models, is the criterion for these models. To generate the simulated values in this work, the latest model IEM was used. IEM is a radiation transfer model based on a theoretical (physical) model. It is suitable for different roughness conditions and spatial independence by combining the Kirchoff model and the small disturbance model (SPM). Compared with other empirical models, this method is more suitable for extraterrestrial weathering layers, because its parameters depend on the location and have a wide range of surface roughness(Shahsavarhaghighi et al., 2013)

A.K Fung was the first to design the full version of the IEM model. It depends on a more detailed description of the integral equation of the electric field(Fa & Cai, 2013)

As shown in the Integral Equations Model, σ^0 represents the like-polarized backscattering coefficient (Shukla et al., 2019).

$$\sigma_{pp}^0 = \frac{k^2}{2}\, e^{-2k_z^2\sigma_h^2} \sum_{n=1}^{\infty} \frac{\sigma_h^{2n}|I_{pp}^n|^2 W^n(-2k_x,0)}{n!} \qquad (4)$$

Where,

$$I_{pp}^n = (2k_z)^n f_{pp} e^{-\sigma_h^2 k_z^2} + \frac{k_z^n[F_{pp}(-k_x,0)+ F_{pp}(k_x,0)]}{2} \qquad (5)$$

For the parameters and f_{vv} and f_{hh} of the IEM equation, these expressions can be expressed according to the Fresnel reflection coefficient(Shukla, 2019).

$$f_{vv} = {2R_V}/{cos\theta} \;,\; f_{hh}= {-2R_h}/{cos\theta} \qquad (6)$$

$$[F_{vv}(-k_x,0) + F_{vv}(k_x,0)] = \frac{2\,sin^2\theta\,(1+R_v)^2}{cos\theta}\left[\left(1-\frac{1}{\epsilon}\right)+ \frac{\epsilon-sin^2\theta-\epsilon cos^2\theta}{\epsilon^2 cos^2\theta}\right] \qquad (7)$$

$$[F_{hh}(-k_x,0) + F_{hh}(k_x,0)] = -\frac{2\,sin^2\theta(1+R_h)^2}{cos\,\theta}\left[\frac{\epsilon-1}{cos^2\theta}\right] \qquad (8)$$

In the above equation, the complex dielectric constant is represented by ϵ, k_z denotes $k\cos\theta$, k_x denotes $k\sin\theta$

Using Equations 9 and 10 for horizontal and vertical polarizations, respectively, Fresnel reflection coefficients can be determined

$$R_h = \frac{\cos\theta - \sqrt{\epsilon - \sin^2\theta}}{\cos\theta + \sqrt{\epsilon - \sin^2\theta}} \tag{9}$$

$$R_v = \frac{\epsilon\cos\theta - \sqrt{\epsilon - \sin^2\theta}}{\epsilon\cos\theta + \sqrt{\epsilon - \sin^2\theta}} \tag{10}$$

By transforming the nth power of surface correlation function ϱ (x,y) to the Fourier transform, Wn (u,v) can be defined as shown in equation 11.

$$W^n(u, v) = \frac{1}{2\pi}\int_{-\infty}^{\infty} \rho^n (x, y) e^{-jux-jvy}dxdy \tag{11}$$

The Gaussian surface correlation function is given by equation 12

$$\rho(x, y) = e^{-\frac{x^2}{L_x^2}-\frac{y^2}{L_y^2}} \quad \text{(Gaussian)} \tag{12}$$

The correlation length in x and y is given by Lx and Ly.

2.8. Data simulations assumptions

Equations should be used to generate a large dataset for backscatter coefficient values in HH and VV polarisation for data simulation. A correlation length of 12.6 cm was assumed due to the lack of ground data that was available for the purpose of calculating parameters of IEM.. A dielectric constant has only one real component that has been changed in simulation, while the complex component has been set to 0.008 to reduce the effect it has on backscattering for which the datset is created for IEM equation. Data simulations analyzing EMR interactions with subsurface structures do not include the scattering response of slopes, boulders, walls, and sub-surface structures that are situated adjacent to topmost regolith surfaces and are based on the IEM equation.

2.9. SAR: Capability and Importance in present work

Synthetic Aperture Radar commonly known as SAR is a microwave remote sensing technique in which it can penetrate clouds and they are independent of the sun as the source and do not need any external light to operate so they can operate both in the day as well as in the night time. They are also sensitive to moisture content. These properties make them an ideal choice for studying the planetary surfaces and other celestial bodies (P. N. Calla et al., 2014). SAR has a variety of applications in earth observations as well as in planetary bodies for mapping and monitoring terrestrial surfaces.

2.9.1. SAR Polarimetry

Polarization is described using a combination of only two terms usually a vertical component and a horizontal component. It is to be taken only for the electric field vector, not the magnetic field. This is because the most common indication of electromagnetic radiation is due chiefly to the electric field. If we were to send a wave down a piece of rope, for instance, if the wave is moving up and down or to and fro for electromagnetic waves, this is known as polarization. This is only for transverse waves. In

electromagnetic waves, polarization is described by the electric field, since the magnetic field is always perpendicular to that of the electric field. (Woodhouse, 2006).
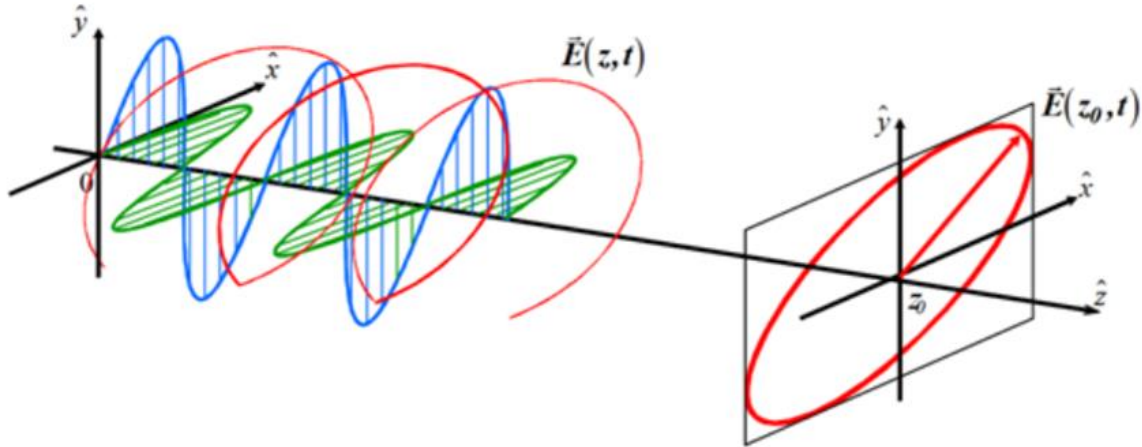
Figure 5 Description of propogation of electromagnetic wave

Figure 5 shows the horizontal and vertical components of the electric field as blue and green waves, respectively. When visualized along the direction of the wave, the electric field vector of a fully polarized wave comprises an ellipse called a polarization ellipse.

SAR polarimetry shows the capacity to separate the different scattering elements available in a single SAR resolution cell. One side of a flight path is illuminated continuously by the SAR system. It is more convenient to consider SAR systems in Horizontal (H) and Vertical (V) orientations, and the channels are namely HH which is horizontally transmitted and horizontally received, and for HV which is horizontally transmitted and vertically received. In this case, the polarised channels or co-pol channels are referred to as HH, and the cross-polarized channels as HV. Various levels of polarisation complexity can be found in SAR systems. A single polarization signal can be either HH, HV, VH or VV depending on the channel. The second one is dual polarized which can be either HH and VV or HH and VV or HV and VV. In the last one, all the four channels are present HH, HV, VH, and VV and are called Full or quad polarised.

There are different types of polarization too, namely linear polarization, elliptical polarization, and circular polarization (See Fig 6). In linear polarization, the electromagnetic waves are restricted to a single plane along the direction of propagation. Whereas, in elliptical polarization, the electric field of EM wave comprises unequal amplitudes or phase differences other than $\pi/2$. In circular polarization, the electric field of the EM wave has two linear components and has the same amplitude with a phase difference of $\pi/2$(Woodhouse, 2006).
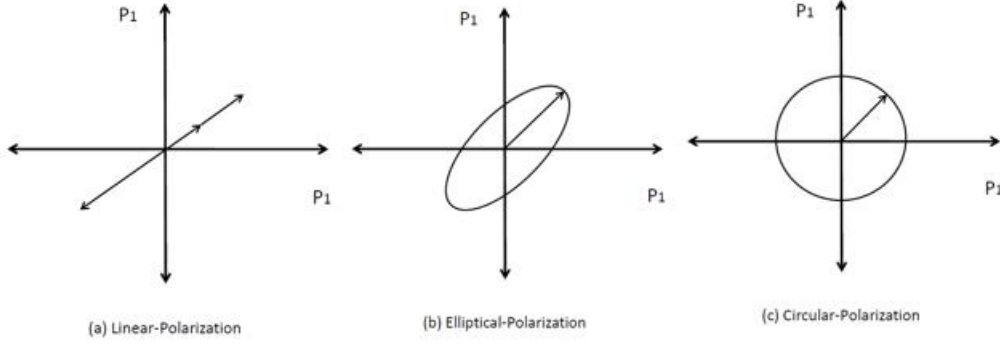
Figure 6 Polarization (a) Linear-Polarization (b) Elliptical-Polarization (c) Circular-Polarization

Hybrid polarimetry is a technique in which the transmission of circularly polarised waves takes place, and two mutually coherent polarised waves are received (P. N. Calla et al., 2014). Chandrayaan-1 and LRO are prime examples of having sensors related to hybrid polarimetry. Full polarimetry or quad pol data have all the polarization channels and provide more scattering information than any other polarization state e.g., linear, elliptical, and circular. It also causes to give more scattering information about a target in certain model-based decomposition and Eigen vector-based in comparison to m-χ decomposition or m-δ decomposition (Putrevu et al., 2015).

In order to study the lunar surface's scattering properties, Stokes parameters are needed. The polarization state of electromagnetic radiation is defined by a set of values that define the stokes parameters. There are four stokes parameters namely S_0, S_1, S_2, S_3 or S_1, S_2, S_3, S_4 shown in equation 13 The first stokes vector S_1 explains the total intensity of the wave. The second stokes vector S_2 talks about the polarization state. The third stokes vector S_3 explains the type of polarization and the fourth stokes vector S_4 is related to the rotation i.e., left-handed or right-handed. It can be explained in detail in equation 1 (P. N. Calla et al., 2014).

$$\begin{bmatrix} S_1 \\ S_2 \\ S_3 \\ S_4 \end{bmatrix} = \begin{bmatrix} < |E_H|^2 + < |E_V|^2 > \\ < |E_H|^2 - < |E_V|^2 > \\ 2Re < E_H E_V^* > \\ -2Im < E_H E_V^* > \end{bmatrix} \quad (13)$$

2.9.2. Coherency Matrix

The scattering matrix is a 2*2 matrix, which consists of four complex elements, which consists of four complex elements, in which the diagonal elements represent the co-polarised information i.e. Radar waves are polarized in the same sense when sent and received, whereas off-diagonal elements represent cross-polarized information, since the transmitted and the received waves have orthogonal polarizations(Woodhouse, 2006).

$$[S] = \begin{bmatrix} S_{HH} & S_{HV} \\ S_{VH} & S_{VV} \end{bmatrix} \quad (14)$$

A particular scattering mechanism for a pure target as its information is described by the scattering matrix. The key issue is that the Earth features are often distributed or complex, which results in a variety of

scattering responses. Accordingly, a scattering matrix will not be able to provide sufficient information to describe the surface's different physical properties in such a case.. Consequently, the second-order statistics of scattering matrix are used here, namely, the covariance and coherence matrices. By using Pauli and Lexicographic matrices, these scattering matrices from the corresponding scattering matrix is obtained(Boerner, 2004).

Eq 15 provides the lexicographic vector form for monostatic reciprocal backscattering assuming the reciprocity condition $S_{HV} = S_{VH}$.

$$K_L = \begin{matrix} S_{HH} \\ \sqrt{2}S_{HV} \\ S_{VV} \end{matrix} \qquad (15)$$

The coherency matrix is obtained as (eq. 16)

$$< [T] > = < K_P \, K_P^{\dagger} > \quad (16)$$

Where, the average over the whole data is represented by < >, the Pauli vector is represented by k_p which is given by (eq.17)

$$K_P = \frac{1}{\sqrt{2}} \begin{matrix} S_{HH} + S_{HV} \\ S_{HH} - S_{HV} \\ 2S_{HV} \end{matrix} \quad (17)$$

The coherency matrix obtained from above is given by (eq. 18)

$$< [T] > = \begin{bmatrix} |S_{HH} + S_{VV}|^2 & \{(S_{HH} + S_{VV})(S_{HH} - S_{VV})\} & 2\{(S_{HH} + S_{VV})S^*_{HV}\} \\ \{(S_{HH} - S_{VV})(S_{HH} + S_{VV})^*\} & |S_{HH} - S_{VV}|^2 & 2\{(S_{HH} - S_{VV})S^*_{HV}\} \\ 2\{S_{HV}(S_{HH} + S_{VV})^*\} & 2S_{HV}(S_{HH} - S_{VV})^* & 4\{|S_{HV}{}^2|\} \end{bmatrix} \quad (18)$$

In hybrid polarimetry, it is used to explain the physical characteristics of the target surface like surface roughness, dielectric constant, etc. In this, the signal that is received is collected in four channels and results in a wave coherency matrix, which is in the form of a 2*2 coherency matrix (eq.19) (Campbell, 2002)

$$[J] = \begin{bmatrix} < E_x E_x{}^* > & < E_x E_y{}^* > \\ < E_y E_x{}^* > & < E_y E_y{}^* > \end{bmatrix} \quad (19)$$

In the first matrix of [J], it has x and y as perpendicular bases. Whereas, the matrix denotes that the transmission is done in left circular polarization which is denoted by L and the receiving is done in H and V configuration.

2.10. Scattering of EM waves

The occurrence of scattering happens when the EMR strikes any target surface after interaction with the material of the target. In this study, mainly three types of scattering take place depending on the surface of the target i.e., lunar regolith, and are surface scattering, double-bounce scattering, and volume scattering (Figure 7) (Woodhouse, 2006). In a variety of homogeneous media, surface scattering occurs at the edges of the surface. As a result of impacting the surfaces that act as corner reflectors, double bounce scattering occurs when the incident wave is reflected in the same direction. In the lunar study, a crater's wall or floor

acts as a dihedral surface and it reflects the electromagnetic wave in the same direction. If the rocks are inclined at an angle, they can also give double-bounce scattering (Yamaguchi et al., 2005; Zou et al., 2015) In volume scattering, the electromagnetic waves are equally distributed in all directions throughout the medium, resulting in diffuse scattering (Woodhouse, 2006). Surface roughness, wavelength, and average dielectric constant affect the scattering angle caused by volume scattering. Prime examples of volume scattering are tree structures, soil surfaces, and snow covers. When it comes to the lunar surface, there can be changes in the dielectric constant depending on the medium which results in the volume scattering. Probable locations of water ice deposits can also be found at these locations as subsurface interactions result in volume scattering.
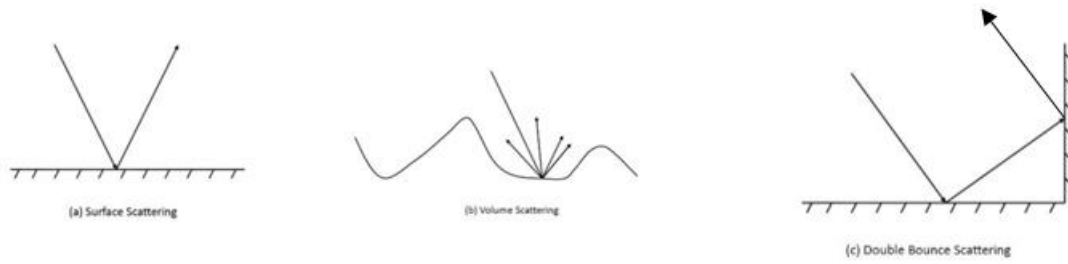
Figure 7 Types of scattering (a) Surface scattering (b) Volume scattering (c) Double-bounce scattering

2.10.1. Circular Polarization Ratio (CPR)

CPR is one of the most important parameters for measuring water ice content on the surface of the moon. According to the formula, SC is the ratio between the received power in the same sense (SC) and the transmitted power in the opposite sense (OC)(P. N. Calla et al., 2014; Mohan et al., 2011). Due to the incident radar wave bouncing multiple times, rough surfaces have a high CPR value since they generate more same-sense signals.. Usually, in surface scattering, the CPR value is less than unity. The main issue of using CPR alone is that if a high CPR value is obtained from the rough surface such that rocks, lava flows. So, in this scenario, if a radar signal is transmitted (left circular polarization) and after hitting a boulder it changes into right circular polarization (RCP) and then again rebounds to another boulder and changes the polarization from RCP TO LCP and then to the receiver (see Figure 8). This results in the double bounce scattering, and which can be a misleading result for the interpretation of water ice content (Mohan et al., 2011). The relation of CPR with the stokes parameter is given in the equation 20.

$$CPR = S1 - S4/S1 + S4 \quad (20)$$
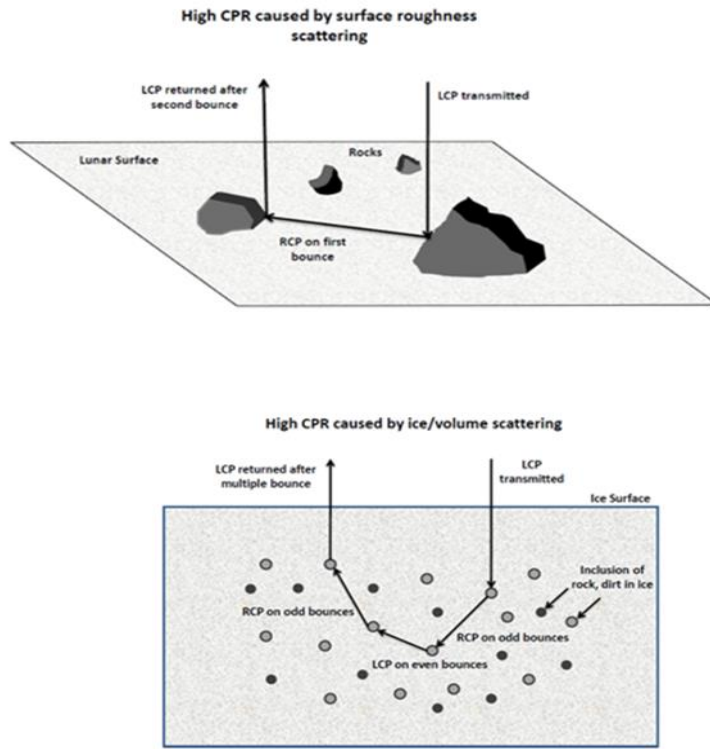
Figure 8 Higher CPR caused by planetary ice (volume) or roughness
due to surface scattering

2.11. Decompositions Used

The major decomposition techniques used in the study of the lunar surface are m-chi (m-χ), m-delta (m-δ), m-alpha(m-α) for hybrid polarimetry data are used.

To calculate the degree of polarization (m) from equation 21, the stokes child parameters δ and χ is calculated from the equation (22) and (23)

$$m = \frac{\sqrt{S_2^2 + S_3^2 + S_4^2}}{S_1} \qquad (21)$$

A completely polarized wave has a degree of polarization of 1, while a completely unpolarized wave has a degree of polarization of 0.
The relative phase (δ) denotes double bounce scattering and is calculated as per eq. 3

$$\delta = \tan^{-1}(s_4/s_3) \qquad (22)$$

The ellipticity parameter (χ) is sensitive to double bounce scattering compared to the surface scattering and is calculated as per eq 23.

$$\text{Sin}2\chi = -S_4/mS_1 \qquad (23)$$

2.11.1. m-δ decomposition

These decomposition allow land and oceanographic researchers to distinguish surface scattering and double bounce scattering. The parameters in this decomposition are m, relative phase, and orientation angle (δ) (Raney Keith et al., 2012). It is calculated by equations (24), (25) and (26).

$$s = [mS_1 \frac{(1+sin\delta)}{2}]^{\frac{1}{2}} \qquad (24)$$

$$v = [S_1 (1-m)]^{\frac{1}{2}} \qquad (25)$$

$$d = [mS_1 \frac{(1-sin\delta)}{2}]^{\frac{1}{2}} \qquad (26)$$

Where, s= odd-bounce scattering or surface scattering, v= volumetric scattering, and d= even-bounce scattering or double-bounce scattering

The parameters are dependent mainly on two components δ and degree of polarization (m). δ differentiates between surface and double bounce which makes it an important parameter. So, the positive value of δ shows signs of the dominance of surface scattering and the negative value for the double bounce scattering dominance.

2.11.2. m-χ decomposition

From the lunar surface, this decomposition is widely applied when separating even-bounce scattering from odd-bounce scattering and the parameters that are used are m, χ, and δ (P. N. Calla et al., 2014). This decomposition technique was first time used by Raney in hybrid polarimetric data (Raney Keith et al., 2012). For calculations of the parameters in this decomposition are shown in equations (27), (28) and (29).

$$s = [mS_1 \frac{(1-sin\delta)}{2}]^{\frac{1}{2}} \qquad (27)$$

$$v = [S_1 (1-m)]^{\frac{1}{2}} \qquad (28)$$

$$d = [mS_1 \frac{(1+sin\delta)}{2}]^{\frac{1}{2}} \qquad (29)$$

Where, s= odd-bounce scattering or surface scattering, v= volumetric scattering, and d= even-bounce scattering or double-bounce scattering

2.11.3. m-α decomposition

The parameter m and polarization angle(α) are determined by the H-α method of decomposition, which consists of eigenvalues.

α is calculated from equation (30)(Tomar, 2015)

$$\alpha = 2|\chi| \qquad (30)$$

m-α decomposition is calculated by equations (31), (32), and (33).

$$s = [mS_1 \frac{(1+cos2\alpha)}{2}]^{\frac{1}{2}} \qquad (31)$$

$$v = [S_1 (1 - m)]^{\frac{1}{2}} \qquad (32)$$

$$d = [mS_1 \frac{(1-cos2\alpha)}{2}]^{\frac{1}{2}} \qquad (33)$$

Where, s= odd-bounce scattering or surface scattering, v= volumetric scattering, and d= even-bounce scattering or double-bounce scattering

The value of alpha (α) is in the range of 0 and $\pi/2$. If the value of α is equal to 0 then it shows surface scattering, if it is in the range of $\pi/4$ then it shows volume scattering and if it shows double-bounce scattering then it is equal to $\pi/2$.

2.11.4. Decomposition models for fully polarimetric datasets

For characterization of L-band DFSAR of Chandrayaan-2 fully polarimetric dataset, two decompositions techniques have been used in this study namely Barnes Decomposition and H-A-α decomposition. Barnes decomposition is based on the 'wave dichotomy' and H-A-α decomposition is based on eigenvalue and eigenvector. The use of these two decompositions in this study was to minimize the overestimation of particular scattering in a target area which is easily seen in the model-based decomposition techniques.

Initially, for L-band data, the calibration was performed on the polarimetric channels of SLC data at the linear scale(Sriram S. Bhiravarasu et al., 2021).

$$\sigma^0(linear) = \frac{DN_{i,j}}{10^{\frac{k}{10}}} \qquad (34)$$

3. STUDY AREAS AND DATASETS

3.1. South Pole Geology

The geology of the moon is quite fascinating and makes us curious as human beings as most of it are still unexplored and unanswerable. The existence and findings of water ice deposits at both of its poles and especially in the South Polar Region makes the south pole an interesting exploratory area because most of the part is in the permanently shadowed region (PSR). The South Pole lies in one of the largest and oldest basins of our solar system recognized till now, that is the South Pole Aitken (SPA) basin (Lucey, 2004; Lucey et al., 1998; *NASA - South Pole -- Aitken Basin*, n.d.). A vast area of the Moon is occupied by SPA, which has a diameter of around 2500 km and depths of about 12 km, dating from pre-Nectarian times. (Kim et al., 2012). Moon's mineralogy consists of the mixtures of feldspar, pyroxene, olivine and, ilmenite. It was found that pyroxene and plagioclase are the major carriers of iron and aluminium respectively whereas, clinopyroxene is present in most of the mare deposits which are also present in the SPA basin. Orthopyroxene is majorly present near the rim of the SPA basin especially in between the Lyman and Antoniadi craters. The Apollo basin in the SPA which is rich in anorthite but is low in FeO also has a major presence of orthopyroxene. Olivine is significantly low in the SPA basin if compared to the other lunar surface (Lucey, 2004). (Lucey et al., 1998) also concluded that the SPA basin's floor is a mixture of lower crust which consists of low-K Fra Mauro (LKFM) mafic rock and the upper mantle contains 10-20 wt% of FeO and approximately 0.1 wt%TiO_2. It was revealed that the crust of the SPA basin is comparatively thinner (20 km) to the average thickness (68 km) of the far side. The center region of the SPA basin is rich in Ca, Fe pyroxene and Mg-rich pyroxenes are predominant in the rest of the central SPA. The outer region of the SPA, which is the SPA exterior, is highly feldspathic (Moriarty & Pieters, 2018).

The South Pole region which is just inside the main aim of the SPA basin is located in the heavily cratered region of the southern highlands(Paul D. Spudis et al., 2008). The geological interpretation of this region is very difficult because of the lunar spin axis as the sunlight is always at low angles in the polar region especially in the south pole making the most of it in PSR. Leibniz β is the large massif platform-like structure and is the most prominent feature in the inner ring of the basin(Paul D. Spudis et al., 2008). As earlier mentioned, this area belongs to the pre-Nectarian period and the terrain in this region is highly informal because of the SPA basin itself. The area is covered in various irregular craters and there is a collection of craters, too. As the average annual temperature of the lunar south pole is around 38K which is very low and the PSR is very cold enough to have water ice deposits. The Hydrogen concentrations in the PSR have been measured by Lunar Energetic Neutron Detector (LEND) which is around 0.3-0.5 wt% Water Equivalent Hydrogen (WEH)(Flahaut et al., 2020). The South Pole consists of the Schrodinger impact basin which consists of the Schrodinger crater, this basin is of much interest because of its structure as it is one of the last two impact basins to be formed on the lunar surface. The basin has several features as there is a deposit of dark material around a volcanic vent which is one of the largest individual volcanic features on the moon. Dark, spectrally similar substance was found at the Apollo-17 landing site, Taurus-Littrow valley, near the southeast edge of Mare Serenitatis. The substance is pyroclastic material and seems to be made of glass. (E.M. et al., 1994). In general, the SPA basin is one of the largest and oldest impact basins in the solar system, and thus it stands a very high chance of having more water ice deposits and other mineral-rich components, given its structure.(Yingst & Head, 1999).

3.1.1.   Lunar South Pole
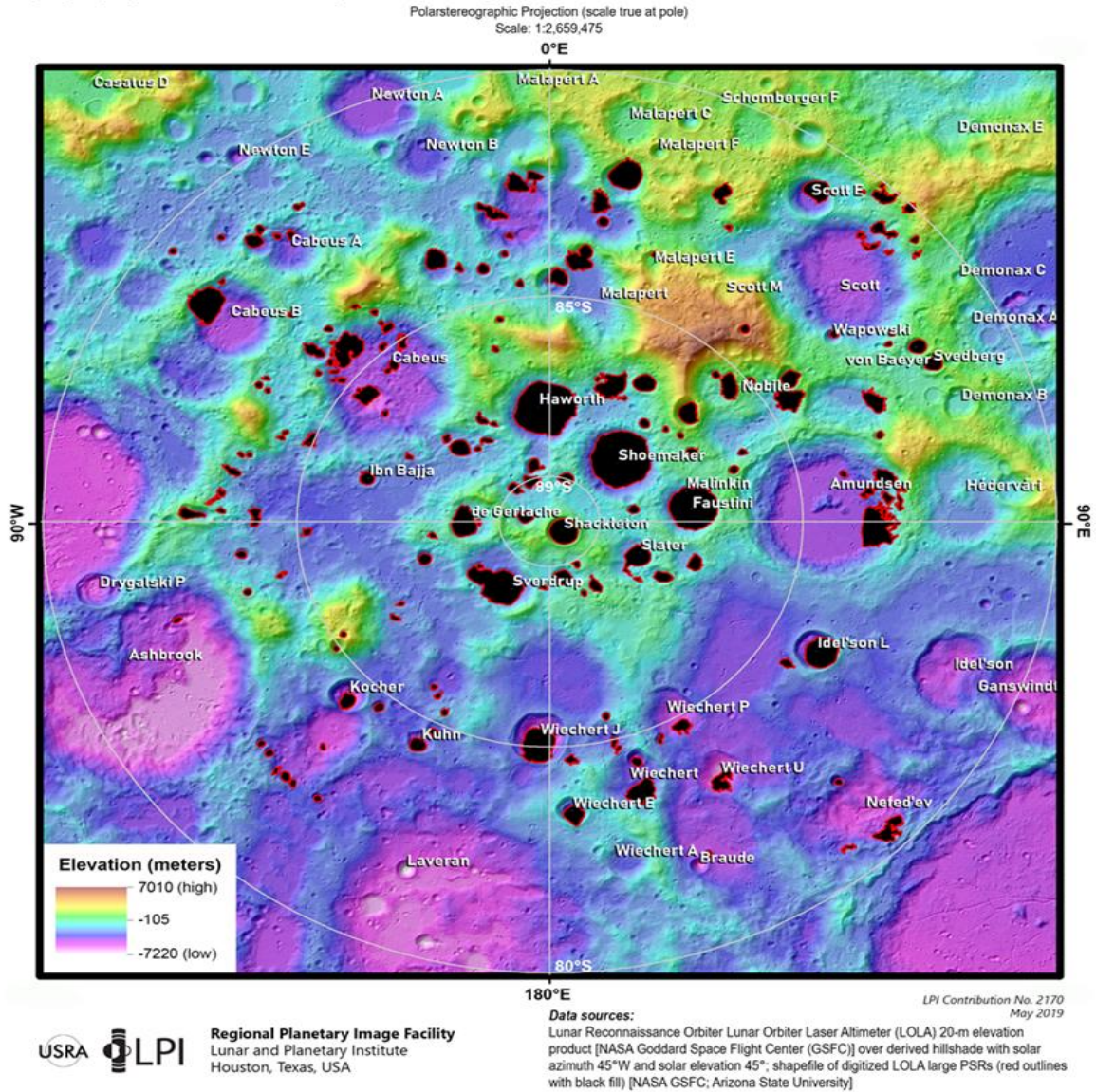
Figure 9 Topography and PSR of the lunar South Pole (Credits-Lunar and Planetary Institute)

Figure 10 Mosaic of the South Pole from Chandrayaan-2 DFSAR scene

The above fig 10, shows the mosaic of 16 scenes covered by Chandrayaan-2 DFSAR for the south pole of the lunar surface. The detailed description of the datasets used in creating the mosaic is shown in Appendix 1. The red areas show the PSR region on the lunar surface. Many craters of this region are unnamed, so they will be addressed based on their coordinates. The PSR region of the lunar surface was taken from the Lunar Orbiter Laser Altimeter (LOLA). The Sinclair-based decomposition has been done on each scene for

characterizing the scattering pattern on the lunar subsurface. This decomposition shows mainly volume scattering and double bounce scattering for the major area, some area shows surface scattering, too.

3.1.2. Cabeus crater

Cabeus crater is about 100 km from the south pole of the moon, close to the south pole of the moon. The average depth of the crater is 4 km, and it looks like a truncated cone. Its flat bottom diameter is 60 km, and the angle of the walls' slope is equal to 10-15°. The location of Cabeus crater is 84° 54' 0" S, 35° 30' 0" W. The main part of the crater is illuminated around 25% of the moon's day and the inner part of the crater is illuminated more than 30% of the moon's day. In the west part of the crater, there is the permanently shadowed region of the crater and concur with a small impact crater on the bottom of Cabeus, which is illuminated no more than 15% of direct sunlight of the moon's day. The average temperature is about 110 K in the north part of the crater, which is the upper limit of the existence of volatile compounds such as water. The maximum temperature also increases from 110 K to 150 K at the same time, which is an interesting point to note that with these variations in the conditions there is a possibility of the presence of volatiles in the regolith of the crater (Kozlova & Lazarev, 2010). A temperature of about 55 K is recorded in the permanently shadowed (PSR) region of the crater (HEIKEN et al., 1991), due to the nature of PSR, and the fact that brightness temperature plays a critical role in this, when brightness temperature changes from 69.93 + 0.5 K to 69.93 - 0.05 K, water ice volume increases from 0 to 7.2% (Meng et al., 2010; Patel et al., 2014). The LCROSS mission detected ~6 wt.% of water ice from the ejecta of the impact plume and it also confirmed that it is not only in just water adsorbed in the grains but, some of the water was ejected in the form of ice from the crater (Colaprete et al., 2010).
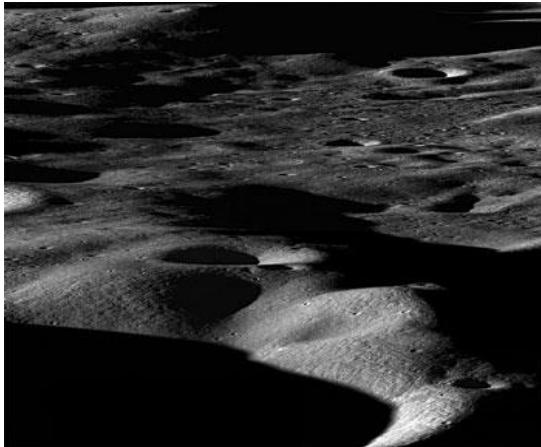
Figure 12 Cabeus Crater Credits-
NASA/GSFC/Arizona State University

Figure 11 Pauli colour composite image of the PSR region for Cabeus crater from CH2 DFSAR Selenographic Referenced Image(SRI)

3.1.3. Shackleton crater

Shackleton crater is situated on the interior basin massif of the South Pole Aitken (SPA) basin. The south pole is situated inside the topographic rim of the SPA basin and it is one of the oldest largest and oldest impact craters on the moon(Petro & Pieters, 2004). It is the largest impact crater in the moon's south pole that is located within one degree of its south pole and measures 20 km in diameter and 4.2 km deep. Initially, the age of this crater was found to be of Eratosthenian age (1-3.2 Gyr before present), but after the studies,

it was concluded that it is of Imbrian age (3.2-3.8 Gyr before present). The age of the Shackleton crater is 3.6 Gyr which is older than the mare surface of the Apollo 15 (3.3 Gyr) landing site, but relatively younger than the Apollo 14 landing site (3.85 Gyr)(Paul D. Spudis et al., 2008; Thomson et al., 2011). The location of the Shackleton crater is 89° 54' 0" S, 0° 0' 0" E and it is nearly coincident with the lunar south pole and whose interior is almost completely in permanent sun shadow. The walls of the crater are smooth because the surface roughness is found in the range of 20-50 meters, while the crater floor is divided into two parts, namely the flat portion and the elevated terrain (Zuber et al., 2012). Due to the permanent shadow, it may have served as a cold trap for volatiles congregating on the poles as both poles of the moon have inflated hydrogen content and if water ice is present, these types of volatiles could be trapped.(Paul D. Spudis et al., 2008).
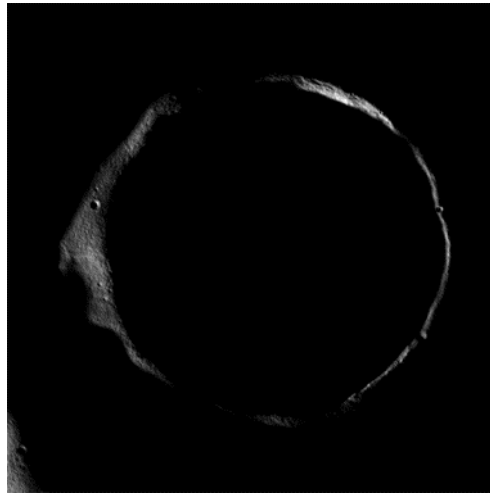
Figure 13 Shackleton Crater (Credits-NASA/GSFC/Arizona State University)

3.1.4. Slater Crater

Slater crater is also one of those craters which are situated at the lunar South Pole and most of its area is covered in PSR. Its coordinates are 88.08°S 111.29°E and its PSR_ID is SP_874430_1188390. A summit between the Shackleton crater and Slater crater has been identified as a possible landing site of the upcoming NASA'S Artemis mission. The site is identified as site 007.
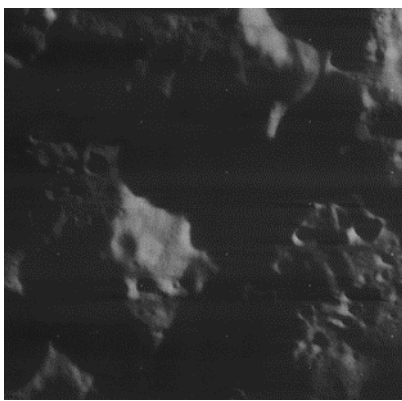
Figure 15 Slater Crater (Credits-LPI, Lunar Orbiter Photo Gallery, Lunar Orbiter 4)
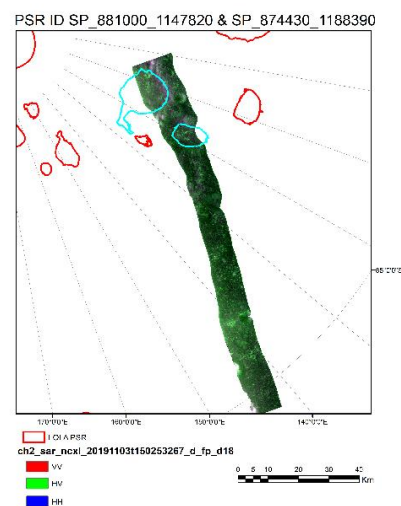
Figure 14 Pauli colour composite image of the PSR region for Slater crater from CH2 DFSAR Selenographic Referenced Image(SRI)
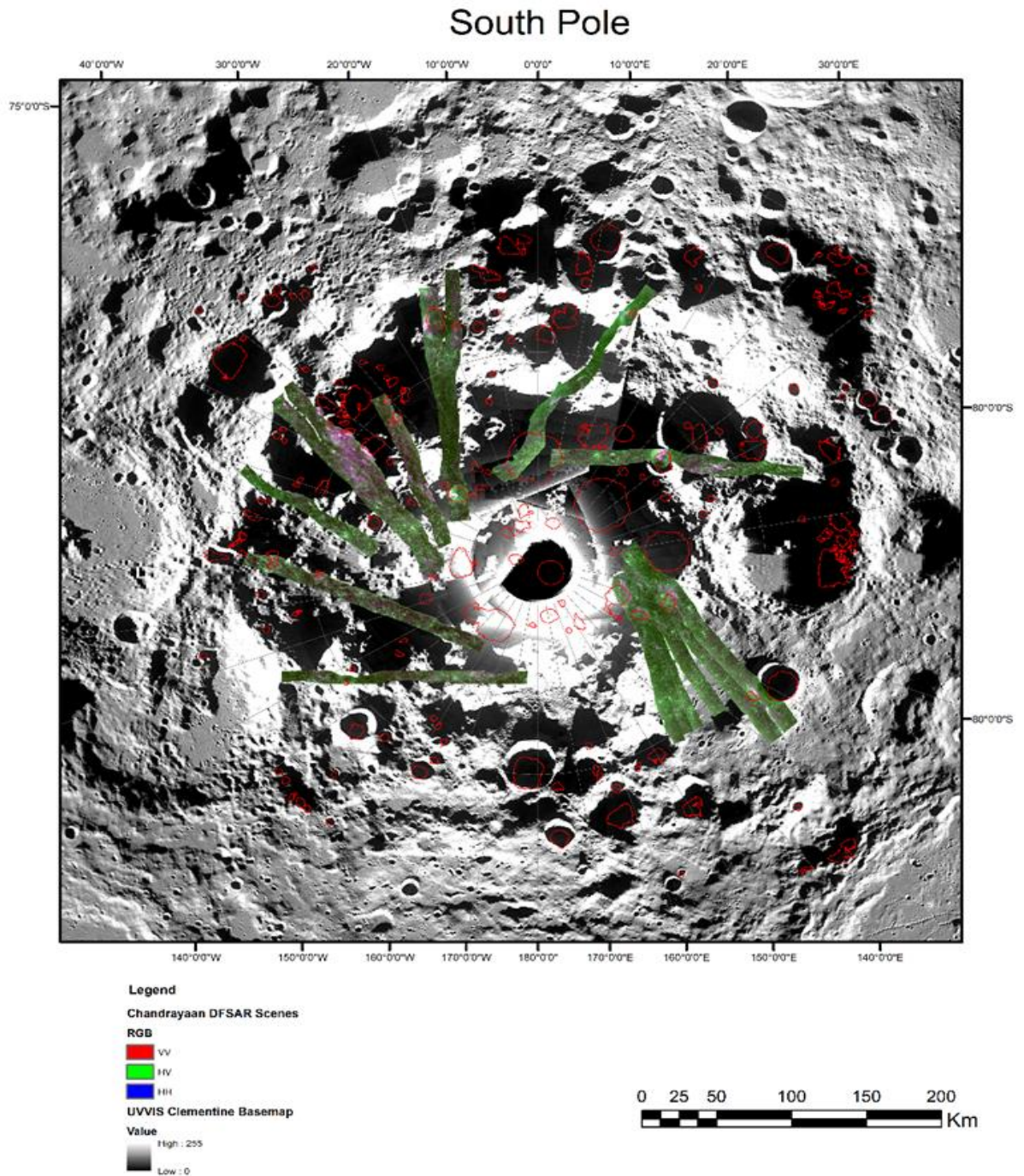
3.2.   Lunar North Pole
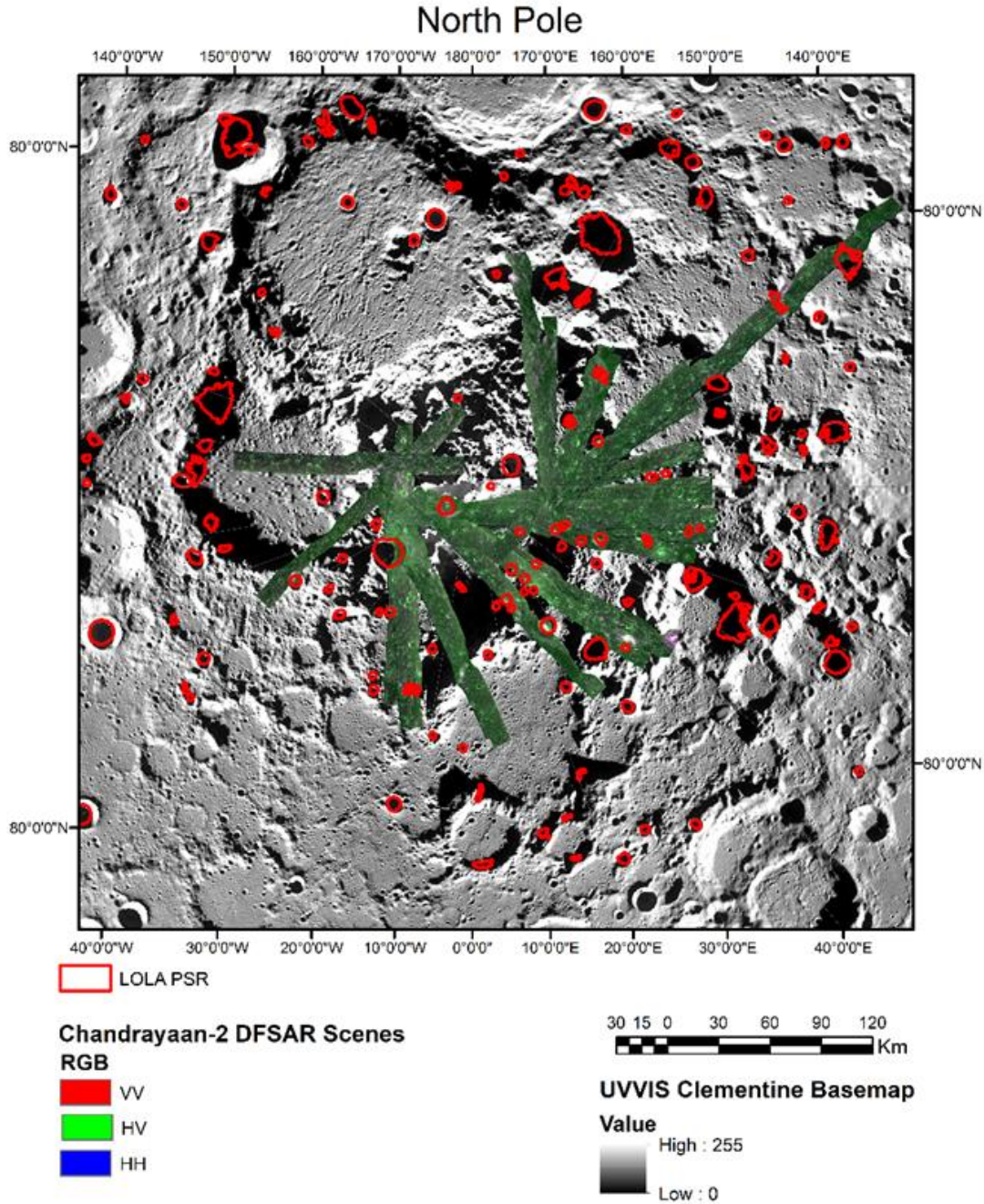
Figure 16 Mosaic of the South Pole from Chandrayaan-2 DFSAR scene

The above fig 16, shows the mosaic of 25 scenes covered by Chandrayaan-2 DFSAR for the north pole of the lunar surface. The detailed description of the datasets used in creating the mosaic is shown in Appendix 1. The red areas show the PSR region on the lunar surface. Four scenes are covering four craters that have

been identified for the study for the North Pole namely Hermite-A and Erlanger. The PSR region of the lunar surface was taken from the Lunar Orbiter Laser Altimeter (LOLA). The Sinclair-based decomposition has been done on each scene for characterizing the scattering pattern on the lunar subsurface. This decomposition shows mainly volume scattering and double bounce scattering for the major area, some area shows surface scattering, too.

3.2.1. Hermite-A crater

Hermite-A crater is located in proximity of a large crater called Hermite. The diameter of this crater is approximately around 20 km, and its coordinates are 87.8° N and 47.1° W. Most of the part of this crater is in PSR and it is also called a twin of Shackleton because of its bowl-shaped structure(O. P. N. Calla et al., 2016).
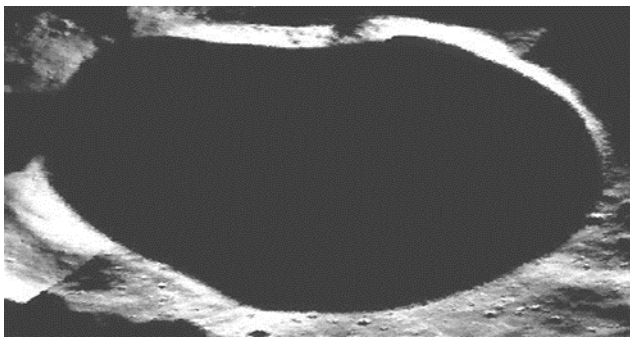
Figure 18 Hermite-A Crater
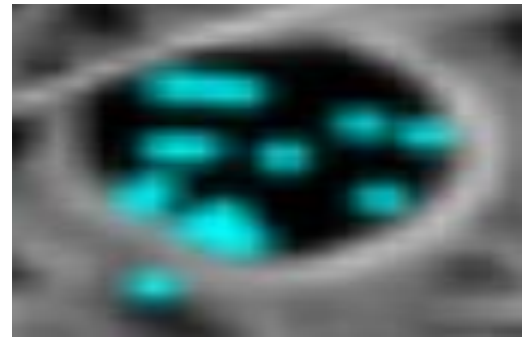
Figure 17 Clusters of surface ice at the Hermite-A crater, detected by NASA's Moon Mineralogy Mapper instrument of ISRO's Chandrayaan-1 mission (Credit: NASA).

3.2.2. Erlanger crater

The diameter of the Erlanger crater is around 10 km and its coordinates are 86.94 N and 28.62 E. It is situated between two large craters Peary and Byrd. This crater is too in PSR as most of the craters do not get sunlight(Bhavya, 2013).

Figure 19 Erlanger crater Credits-NASA/GSFC/Arizona State University

Erlanger Crater(PSR ID NP_869610_0287570), NP_877350_0169810, NP_875450_0179490

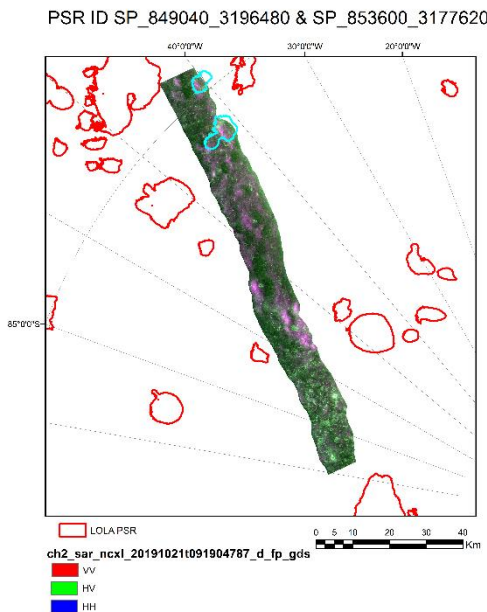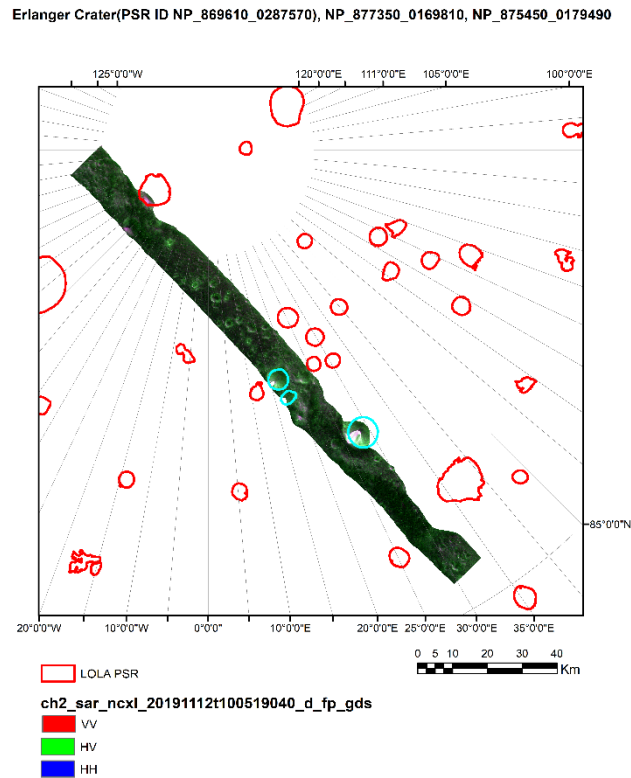

Figure 20 Pauli colour composite image of the PSR region for Erlanger crater from CH2 DFSAR Selenographic Referenced Image(SRI)

3.3. Location of the lunar rille

This study also requires the study of a location of a lunar rille for the study of surface characterization of it for achieving the fourth sub-objective. The region which has been identified is Rimae Sulpicius Gallus.

3.3.1. Rimae Sulpicius Gallus

The rimae Sulpicius Gallus is situated in the Mare Serenitatis region and the region is well known to be of a lunar mare which means it has large dark basaltic plains. The pyroclastic deposits near the Sulpicius Gallus are estimated to be 50m thick and contains both mare and highlands terrain.
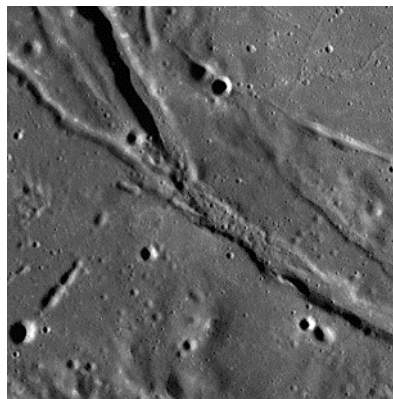
Figure 21 Rimae Sulpicius Gallus Credits- NASA/GSFC/Arizona State University

3.4. Datasets Used

This work will utilize three datasets of different missions namely Chandrayaan-1 Mini-SAR dataset, Lunar Reconnaissance Orbiter (LRO) Miniature Radar Frequency (Mini-RF) dataset, Chandrayaan-2 Dual-Frequency Synthetic Aperture Radar (DFSAR) dataset.

Table 4 Datasets used in the study

Sr No.	Sensor Name	Product ID	Study Area	Band	Resolution(in meters), Azimuth & Range Resolution (CH-2)
1	LRO Mini-RF	LSZ_02261_2CD_OKU_89S140_V1	Shackleton	S	7.5
2	Chandrayaan-1 Mini-SAR	FSB_01299_2CD_OIU_86N326_V1	Erlanger	S	75
3	Chandrayaan-2 DFSAR	ch2_sar_ncxl_20191112t100519040_d_fp_gds	Erlanger	L	0.59 & 9.59
4	Chandrayaan-2 DFSAR	ch2_sar_ncxl_20191103t150253267_d_fp_d18	Slater	L	0.59 & 9.59
5	Chandrayaan-1 Mini-SAR	fsb_01744_1cd_xiu_85n339_v1	Hermite-A	S	75
6	LRO Mini-RF	lsz_06871_1cd_xku_88n304_v1	Hermite-A	S	7.5
7	Chandrayaan-2 DFSAR	ch2_sar_ncxl_20191019t011733461_d_fp_d18	Hermite-A	L	0.55 & 9.59
8	Chandrayaan-2 DFSAR	ch2_sar_ncxl_20191021t091904787_d_fp_gds	Cabeus	L	0.49 & 9.59
9	LRO Mini-RF	LSZ_02615_1CD_XKU_22N010_V1	Rimae Sulpicius Gallus	S	7.5

The datasets used in this work are freely available. The datasets of Mini-SAR of Chandrayaan-1 for Erlanger and Hermite-A is downloaded from PDS Geosciences Node. The datasets of Mini-RF of LRO for Hermite-A and Rimae Sulpicius Gallus is also downloaded from PDS Geosciences Node. The datasets of DFSAR of Chandrayaan-2 for Erlanger, Slater, Hermite-A and Cabeus is downloaded from Indian Space Science Data Centre (ISSDC).

3.5.   Software Used

For achieving the objectives, the following pieces of software have been used

1.   ENVI Classic
2.   Python
3.   Arc GIS
4.   SNAP
5.   PolSAR Pro

4. METHODOLOGY

This chapter talks about the entire approach and steps involved in completing the objectives for this study. It explains the steps involved in pre-processing of the datasets and the steps involved in the estimation of the dielectric constant. It also explains the steps involved in the decomposition techniques and the polarimetric parameters used for the sensors involved in this study. The overall workflow is given in figure 22.
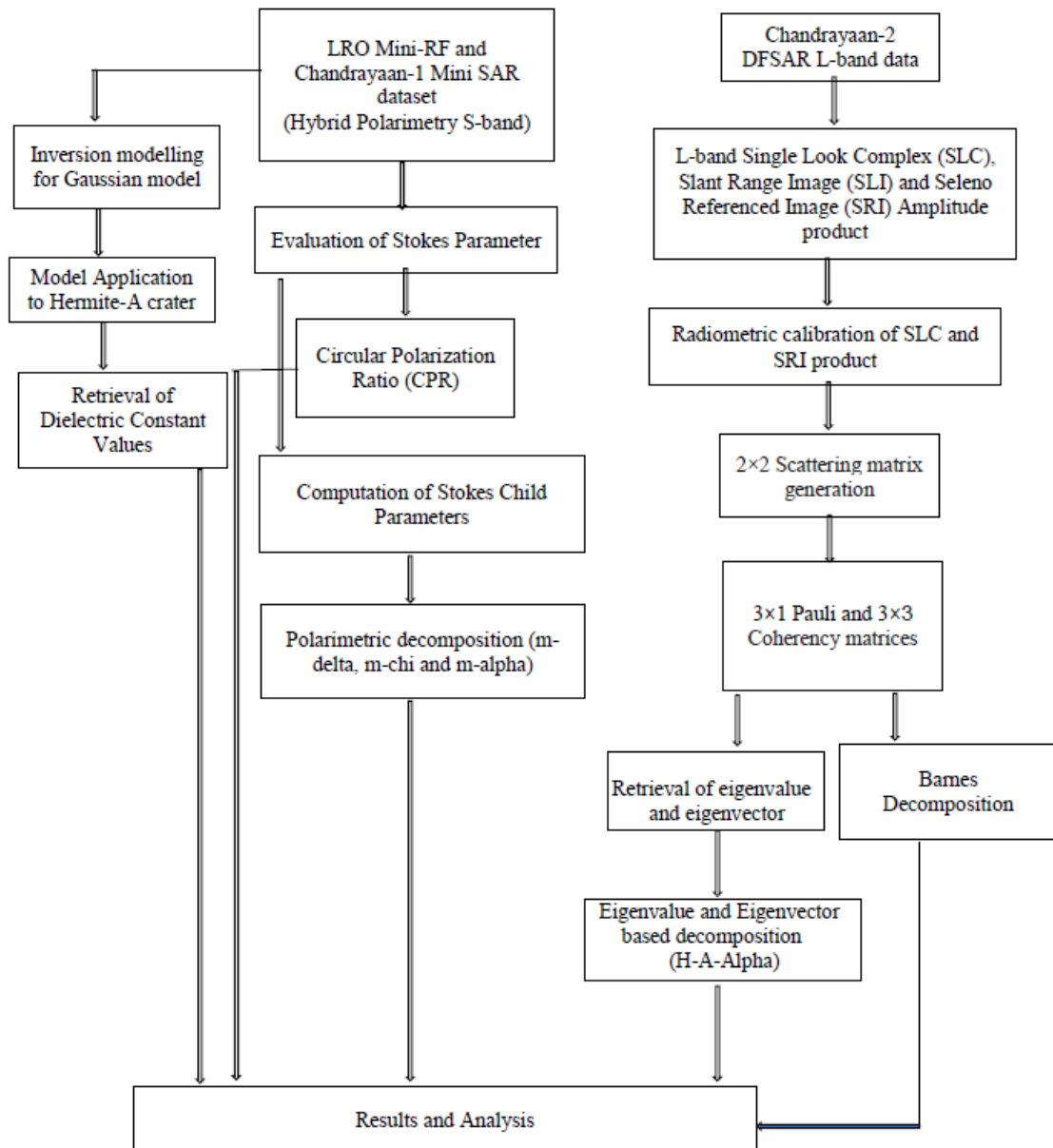
Figure 22 Overall Workflow

4.1. Calculation of Local Incidence Angle

Only half of the moon receives plasma from the solar wind because of its revolution around the earth and rotation on its axis. Only 1.5 degrees of inclination is found on the Moon's axis which as a result, sunlight illuminates various parts throughout the day. Other areas, on the other hand, are perpetually dark and utterly devoid of sunshine. The local incidence angle of the solar wind must be quantified to account for topographical changes on each study region on the lunar surface.

Based on derivations, the solar wind's angle of incidence θ_0 is calculated to be 45°, with the assumption that the solar wind impinges parallel to the Moon's spin plane.

Based on the lunar DTM (GLD100) and lunar north polar DEM, the slopes are calculated for the x and y directions as $\alpha = \tan \omega$ and $\beta = \tan \gamma$, respectively.

Equations and must be used to compute slope angles and from lunar DTM.

$$\gamma = \tan^{-1}\left(\frac{DTM(i,j+1)-DTM(i,j)}{R}\right) \qquad (35)$$

$$\omega = \tan^{-1}\left(-\frac{DTM(i+1,j)-DTM(i,j)}{R}\right) \qquad (36)$$

Where,

Lunar Digital Terrain Model (GLD100) scale is equal to 100m and 10m respectively, in relation to the lunar polar DEM.

Due to changes in local topographic conditions, the angle of incidence of the plasma flow varies locally with the slope of the surface according to the equation 37(Liu et al., 2018).

$$\theta_{ol} = \cos^{-1}\left(\frac{\cos\omega \cos(\gamma-\theta_0)}{\sqrt{(\cos\gamma)^2(\sin\omega)^2+(\cos\omega)^2}}\right) \quad (37)$$

In this study, the local incidence angle for the Hermite-A crater is 62.69 degrees.

4.2. Data Preprocessing

Resampling of incidence angle image (derived from lunar DEM) and normalizing of stokes vector images are part of the data processing for the LRO Mini-RF dataset and Chandrayaan-1 Mini-SAR dataset for Hermite-A crater. The Moon has a radius of 1737.4, a coordinate system of GCS Moon 2000, and a datum of D Moon 2000, with multiple map projections established under the selenographic and planetocentric projection systems. Equirectangular map projection, in which all lines of latitude and longitude are parallel to each other, is assigned to regions in the center area of the Moon. The lunar DEMs at the north and south poles have Moon_2000_npole and Moon_2000_spole coordinate systems, which are equivalent to polar stereoscopic map projections. Specifically, the vertical component image, the horizontal component image, and the incidence angle image were used as input images for Gaussian model testing. MAPCDR is a map-projected calibrated data record of Mini-RF containing four Stokes vectors, each with an equirectangular map projection and datum of D Moon 2000. The MAPCDR pictures have a resolution of 14.806 meters, and the GLD 100 lunar DTM has a resolution of 100 meters. To normalize Stokes vector images for the Hermite-A crater, the average value of the incidence angle was computed. Further horizontal and vertical component pictures can be calculated after normalizing Stokes vector images.
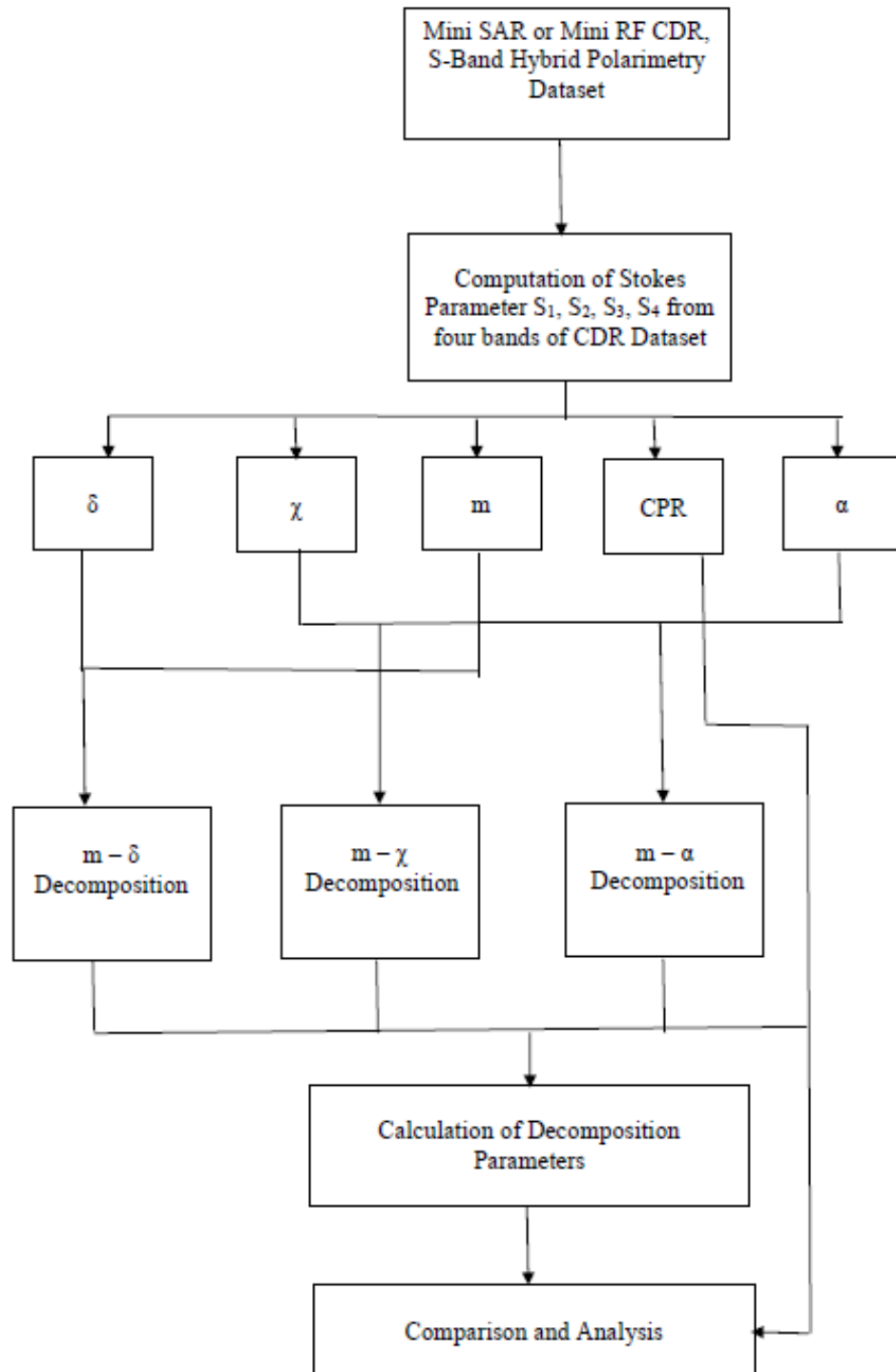
Figure 23 Workflow of Decomposition Techniques for Hybrid polarimetry data

The workflow of the methodology adopted to evaluate the scattering mechanism in four decomposition techniques used by all the datasets is shown in figure 23. The calculation of stokes child parameters is

evaluated after the Stokes parameters. The interpretation is based on the scattering mechanisms of the ejecta and values of CPR for the estimation of lunar volatiles.

The fully polarimetric dataset of L band DFSAR of Chandrayaan-2 is a Single Look Complex (SLC) dataset consisting of four polarization channels HH, HV, VH, and VV and each polarization channel has two bands real and imaginary. The bands are segregated individually for each polarization channel by ENVI and then calibrated individually. The real and imaginary bands are merged and processed to get the scattering and the generation of coherency matrix takes place for further processing and the estimation of the decomposition technique used in the study.

4.2.1. Derivation of Stokes Parameters

Stokes parameters can be calculated from Equation 13 for horizontal, vertical, and their real and imaginary components from the LRO Mini-RF and Chandrayaan-1 Mini-SAR datasets. The Stokes Parameters images which are derived are shown in Fig 24, 25, 26, 27 and 28.
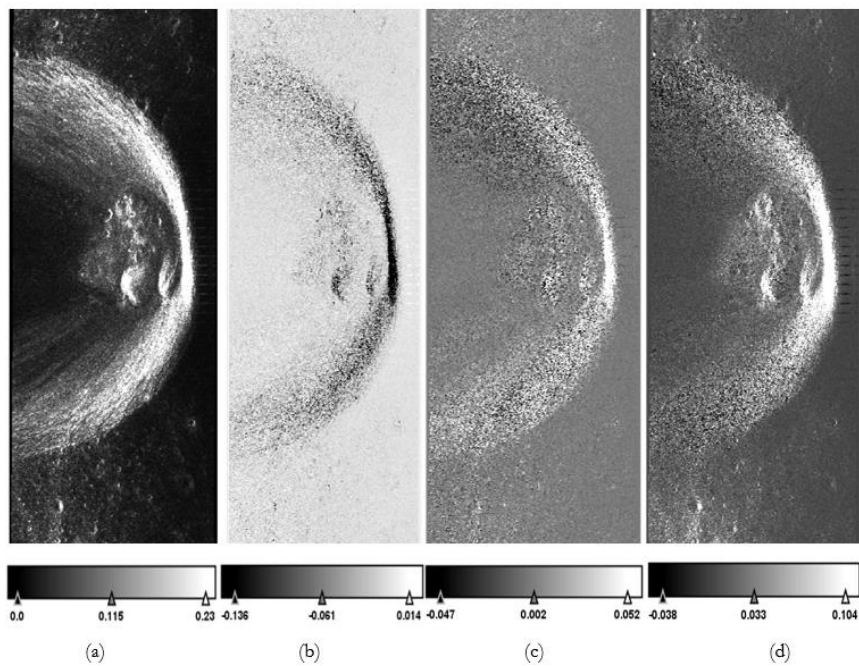
Figure 24 Stokes Parameter Images of Shackleton crater from LRO Mini-RF (a) S1 (b) S2 (c) S3 (d) S4

0.007   0.065   0.122   -0.005   0.016   0.037   -0.023   -0.005   0.013   -0.007   0.016   0.038

(a)   (b)   (c)   (d)
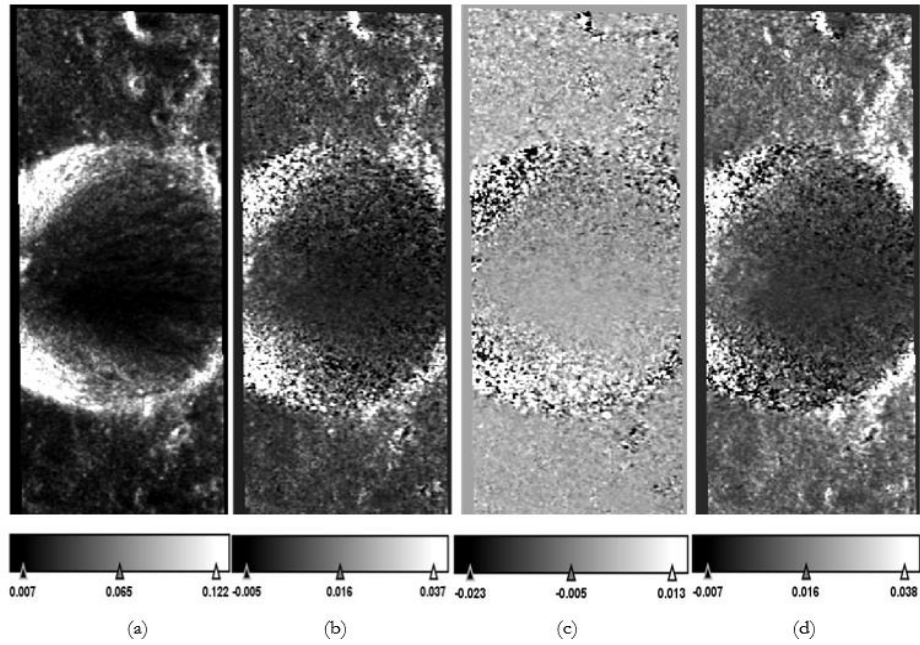
Figure 25 Stokes Parameter Images of Erlanger crater from CH1 Mini-SAR (a) S1 (b) S2 (c) S3 (d) S4

Hermite-A (CH1)

0.0   0.099   0.198   -0.01   0.024   0.058   -0.047   -0.014   0.019   -0.019   0.02   0.058

(a)   (b)   (c)   (d)
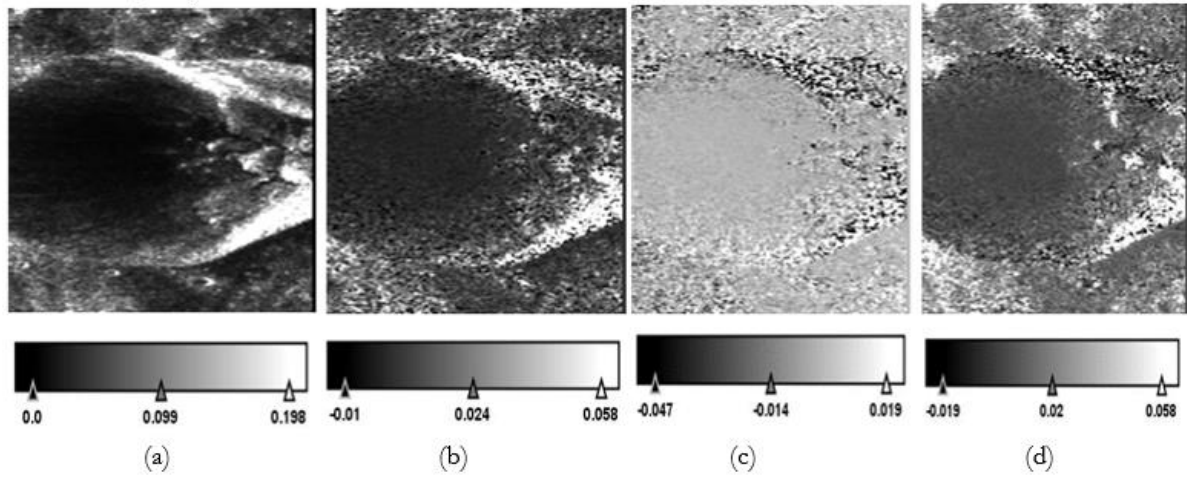
Figure 26 Stokes Parameter Images of Hermite-A crater from CH1 Mini-SAR (a) S1 (b) S2 (c) S3 (d) S4

Hermite-A (LRO)

(a) (b) (c) (d)
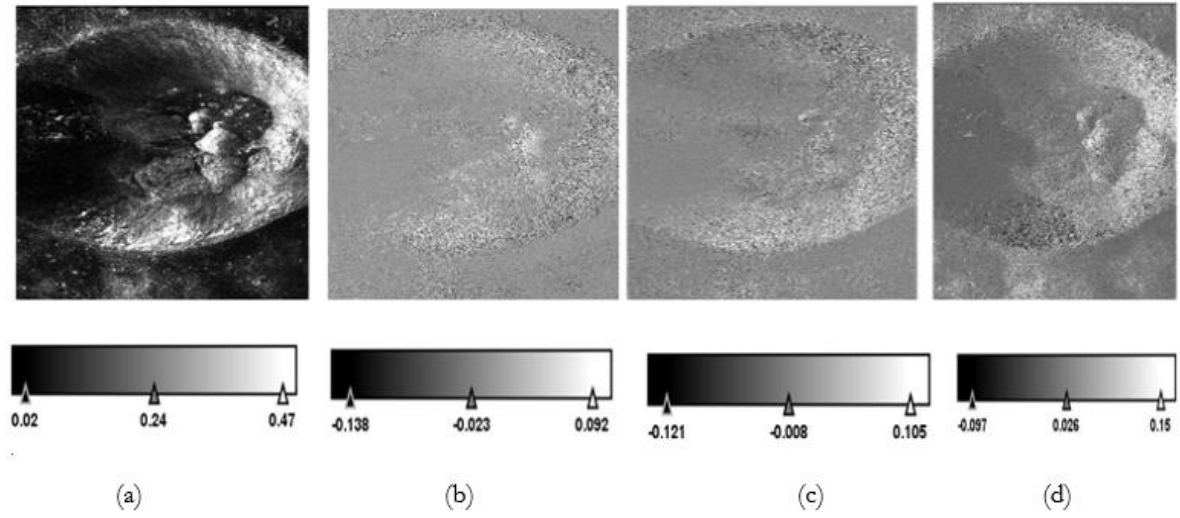
Figure 27 Stokes Parameter Images of Hermite-A crater from LRO Mini-RF (a) S1 (b) S2 (c) S3 (d) S4

(a) (b) (c) (d)
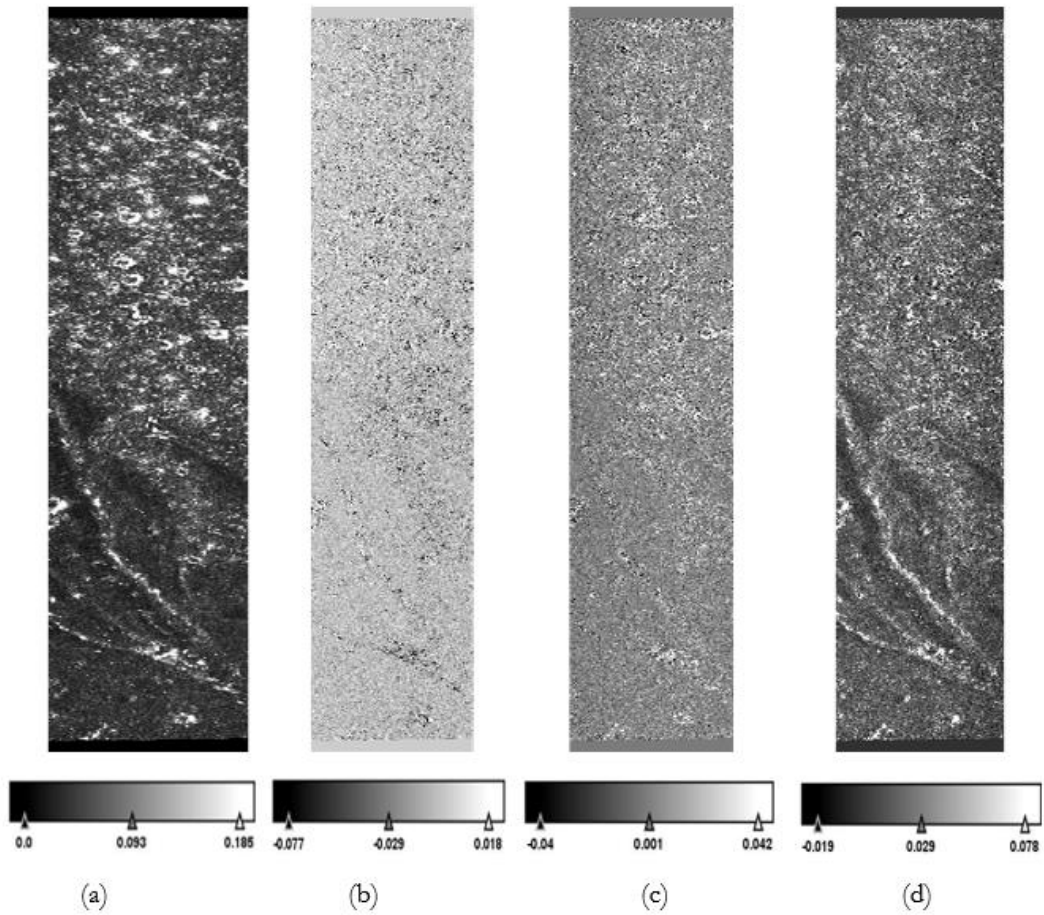
Figure 28 Stokes Parameter Images of Rimae Sulpicius Gallus from LRO Mini-RF (a) S1 (b) S2 (c) S3 (d) S4

4.2.2. Calculation of Stokes Child parameters

The Hybrid polarimetric data techniques used in this study require three decomposition techniques namely m-α, m-δ, and m-χ for LRO-Mini-RF CDR and Chandrayaan-1 Mini-SAR CDR datasets. The four stokes child parameters namely degree of polarization (m), delta (δ), chi (χ), and alpha (α) have been calculated by applying equations (21), (22), (23), and (30) respectively. The Stokes child parameters generated for the craters are given in figure 29, 30, 31, 32 and 33.
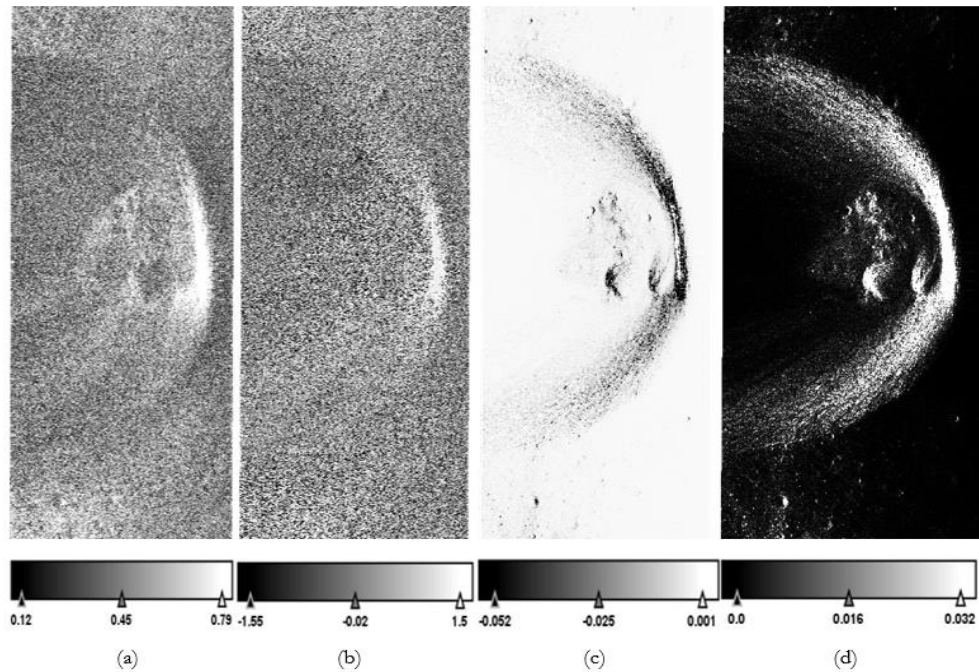
Figure 29 Stokes child parameters of Shackleton crater from LRO Mini-RF (a) m (b) delta (c) chi (d) alpha
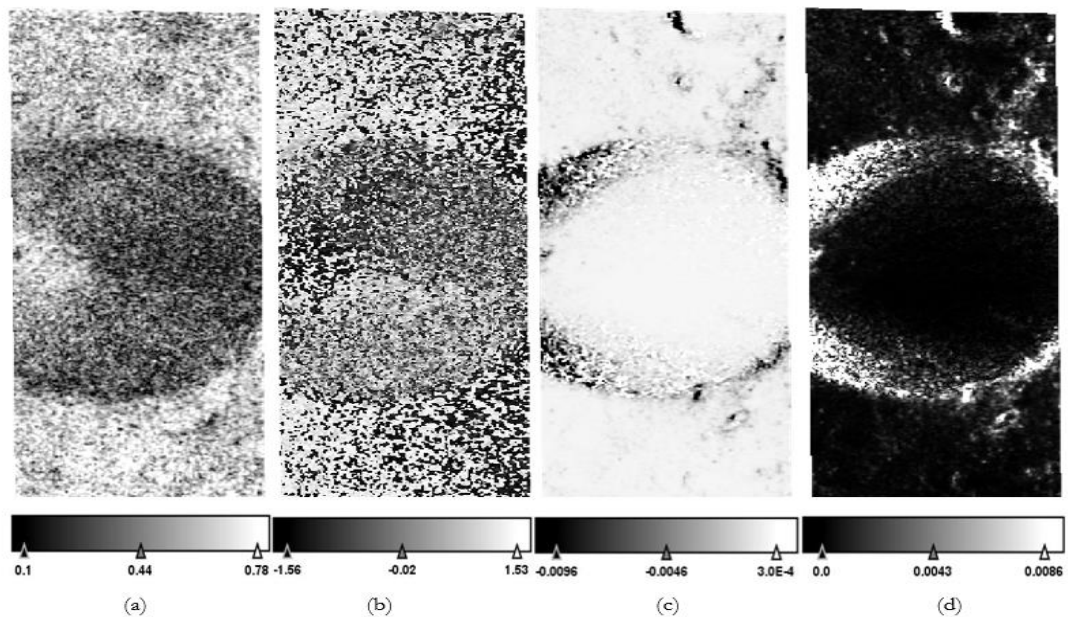
Figure 30 Stokes child parameters of Erlanger crater from CH1 Mini-SAR (a) m (b) delta (c) chi (d) alpha
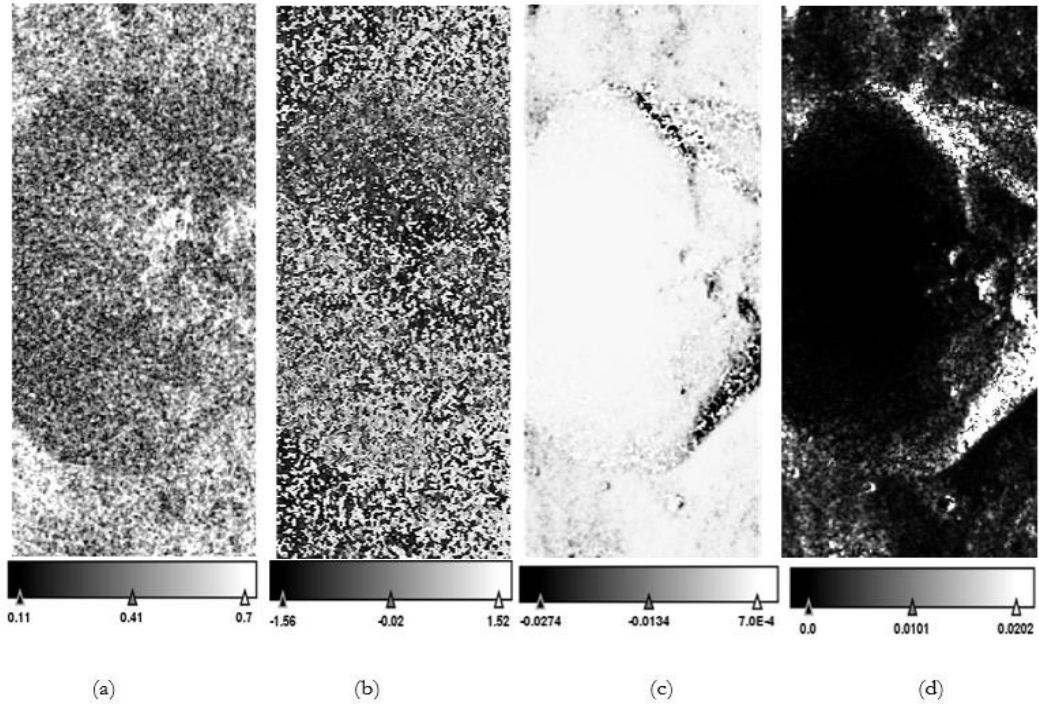
Hermite-A (CH1)

Figure 31 Stokes child parameters of Hermite-A crater from CH1 Mini-SAR (a) m (b) delta (c) chi (d) alpha
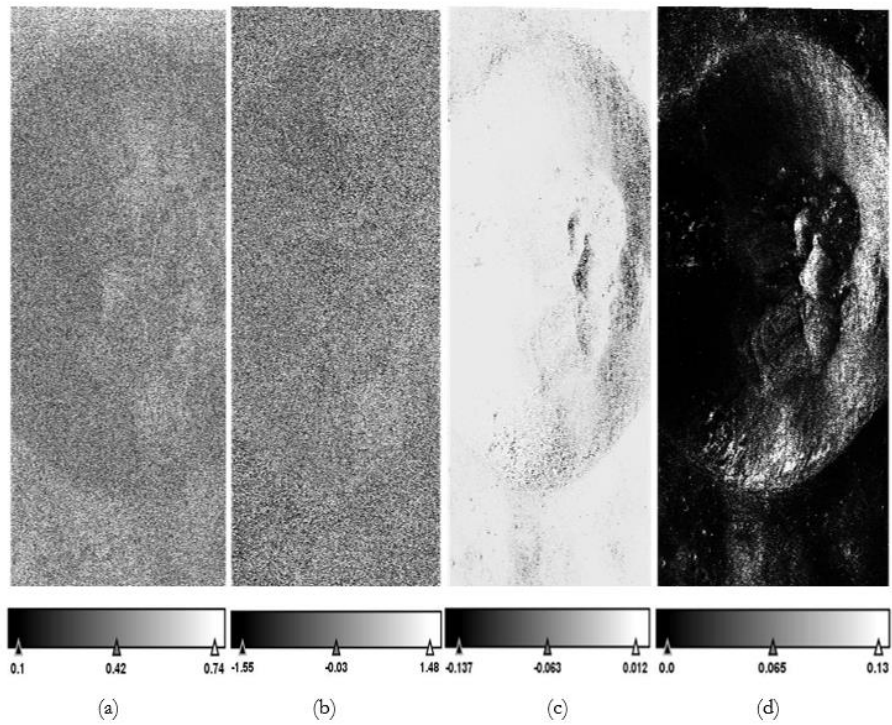
Hermite-A (LRO)

Figure 32 Stokes child parameters of Hermite-A crater from LRO Mini-RF (a) m (b) delta (c) chi (d) alpha
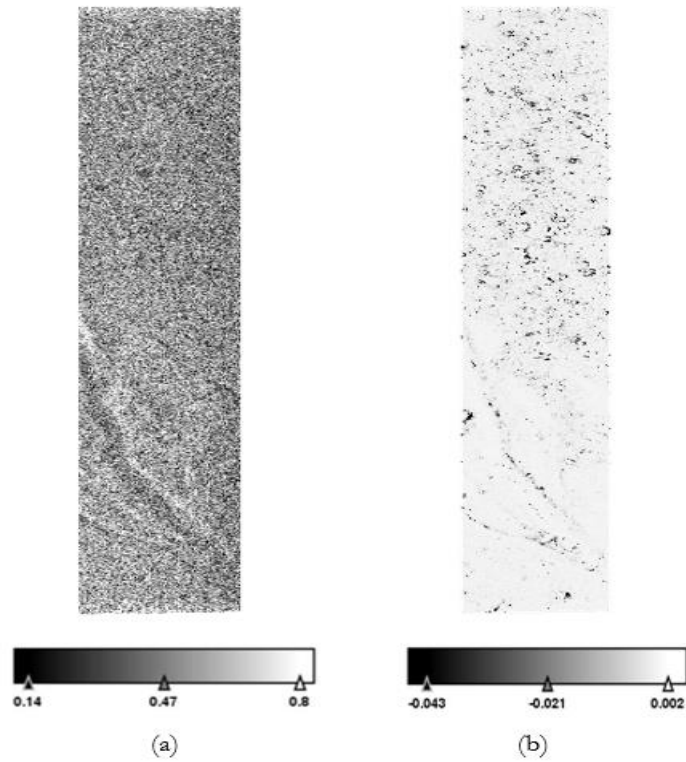
Figure 33 Stokes child parameters of Rimae Sulpicius Gallus from
LRO Mini-RF (a) m (b) chi

The extension of the calculation of Stokes child parameters results in the estimation of CPR and the scattering patterns and the calculation of polarimetric parameters under the decomposition techniques for Hybrid polarimetric datasets and fully polarimetric datasets by equations (), (), (), (), (), (), (), (), (), (). This results in the further analysis and comparison of results by the decomposition techniques and an analogy shall be drawn to study the scattering patterns and lunar volatiles for the craters.

4.2.3. Coherency Matrix generation for fully polarimetric data

The analysis of the fully polarimetric data of L band DFSAR Chandrayaan-2 datasets requires the generation of T3 coherency matrix which is obtained from the scattering matrix and the generation of these matrices are explained in the equation (), (), and (). The Pauli RGB image of the T3 Coherency Matrix for the Erlanger, Slater, Cabeus and Hermite-A craters is given in figure 34 (a),(b), (c) and (d) respectively.

(a) (b) (c) (d)
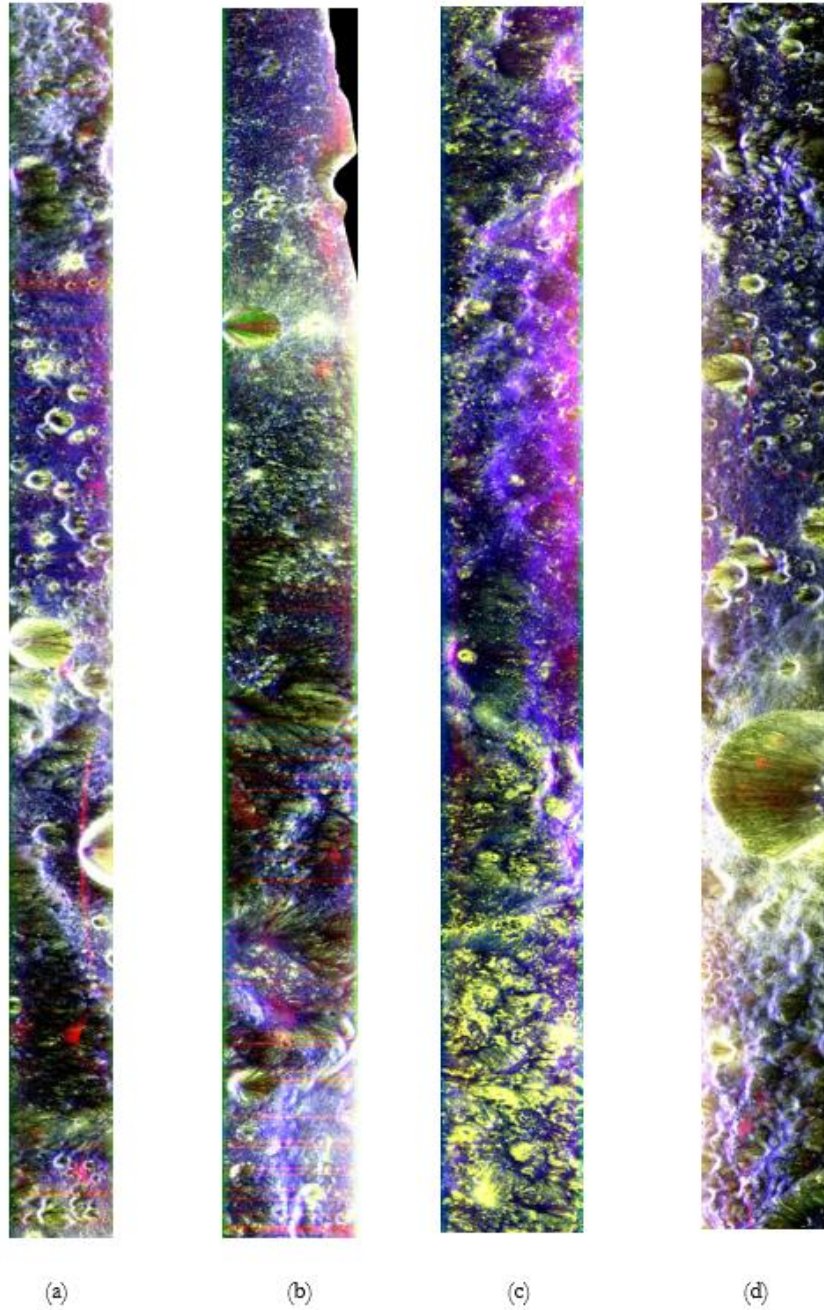
Figure 34 Pauli RGB image of Single Look Complex (SLC) Slant Range Image(SLI) data of CH2 DFSAR (a)Erlanger (b) Slater (c)Cabeus (d) Hermite-A

5.   RESULTS AND DISCUSSIONS

This work involves the characterization of four craters which are situated at the North Pole and the South Pole of the lunar surface which is Hermite-A and Erlanger at the North Pole and the South Pole region has craters which are included are Cabeus and Shackleton and Slater crater. These all craters lie in the permanently shadowed region (PSR) of the lunar surface.

5.1.   Characterization of Shackleton Crater

Shackleton crater is situated in the South Pole region, and it is in PSR. The characterization of this crater is on three decomposition techniques and CPR for Hybrid Pol data of LRO which is of S-band.

5.1.1.   m-δ (m-delta) Decomposition

(a) Double Bounce   (b) Volume   (c) Surface   (d) RGB Composite

Figure 35 m-delta decomposition of LRO (Mini-RF) (a) Double-bounce scattering, (b) Volume scattering ,(c) Surface scattering and (d) RGB colour composite

Figure 35 shows the RGB composite of the m-δ decomposition of Shackleton crater along with the components of scattering mechanisms namely double-bounce, volume, and surface scattering. As it is seen in the Figure that volume scattering is dominant in this decomposition technique. The surface scattering is visible on the right side of the crater wall. However, the presence of the rough surface makes the crater dominant in the volume scattering which is a diffuse scattering pattern due to absorption in the crater walls.

Double bounce scattering is also visible on the crater but is relatively low than the volume and the surface scattering. The surface scattering is dominant outside of the crater which can be seen. The mean values of surface scattering are 0.16, 0.136 for volume scattering and 0.124 for double-bounce scattering.

5.1.2.   m- χ (m-chi) Decomposition

Figure 36 m-chi decomposition of LRO (Mini-RF) (a) Double-bounce scattering, (b) Volume scattering ,(c) Surface scattering and (d) RGB colour composite

The m-chi decomposition separates the odd and even bounce scattering and enhances it. It also differentiates the ejecta and their relative thickness. As shown in figure 36 the RGB composite of the m-χ decomposition, the surface scattering, and double bounce scattering are dominant in the right side of the crater wall and some part of the crater base. The outer rim of the crater also shows the double bounce scattering. The volume scattering is seen in the crater walls and some parts of the crater base which can be because of the presence of rough material in the crater walls and double bounce scattering can be because of natural dihedrals in the surroundings. The mean values of surface scattering are 0.143 which is highest in comparison to the double bounce scattering which is 0.14 and 0.136 for the least volume scattering.

5.1.3. m- α (m-alpha) Decomposition

This decomposition technique is based on Eigenvector analysis of hybrid pol data, and it is close to H/α decomposition of fully polarimetric data. In this angle, α is derived from the stokes parameter. The polarization angle of 0° is sensitive to double bounce scattering, surface scattering is sensitive to 90° and volume scattering is sensitive to predominant depolarized backscatter.

Figure 37 m-alpha decomposition of LRO (Mini-RF) (a) Double-bounce scattering, (b) Volume scattering ,(c) Surface scattering and (d) RGB colour composite

Fig 37 shows the RGB composite of the m-α decomposition, surface scattering is quite dominant in this decomposition technique and is visible in the crater walls, base, and outside the rim. The double bounce scattering is quite low in this decomposition and the presence of volume scattering is greater than the surface scattering due to the presence of the rough surface. High-volume scattering is quite visible in the crater walls. The mean values of the double bounce scattering are very low i.e., 0.0055 which is visible only in the small area of the right side of the crater. Whereas the mean value of volume scattering is 0.136 and for surface scattering, it is 0.2.

5.1.4. Analysis of Circular Polarization Ratio (CPR)
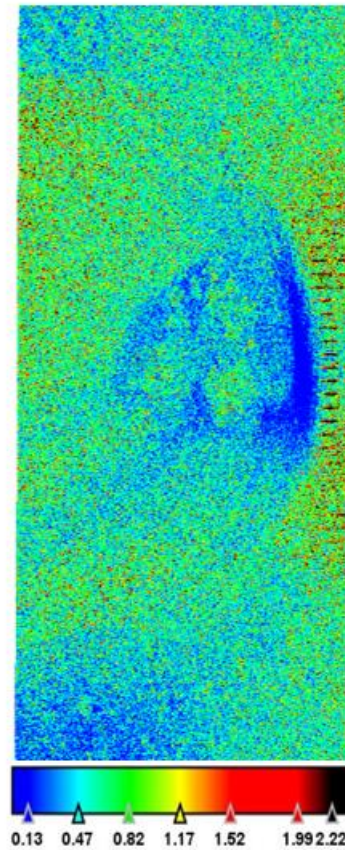
Figure 38 Value of CPR for
Shackleton crater for LRO (Mini-RF)

Figure 38 shows the values of CPR in the crater. The high values of CPR, which is more than 1 in the Shackleton crater depict that the crater has some areas which can be a probable location of water ice deposits. The values which are below 1 relate to the lunar regolith and other materials. The high values of CPR can be also due to the scattering by the rough surface, which can be because of double bounce scattering or volume scattering. The locations of the right side of the crater walls show low CPR, was observed that it showed surface scattering in these regions. The CPR value which is close to 1.99 in some areas is there in crater walls and some areas outside the crater rim.

5.2. Characterization of Erlanger crater

Erlanger crater is one of the small craters situated at the North Pole on the lunar surface. It also lies in the PSR region. The characterization of this crater is also based on three decomposition techniques and CPR for Hybrid Pol data of Chandrayaan-1 and LRO which is of S-band. For Fully polarimetric data of DFSAR of Chandrayaan-2, the Barnes decomposition technique and the H-A-α decomposition technique has been used to analyze the different polarimetric parameters.

5.2.1. m-δ (m-delta) Decomposition

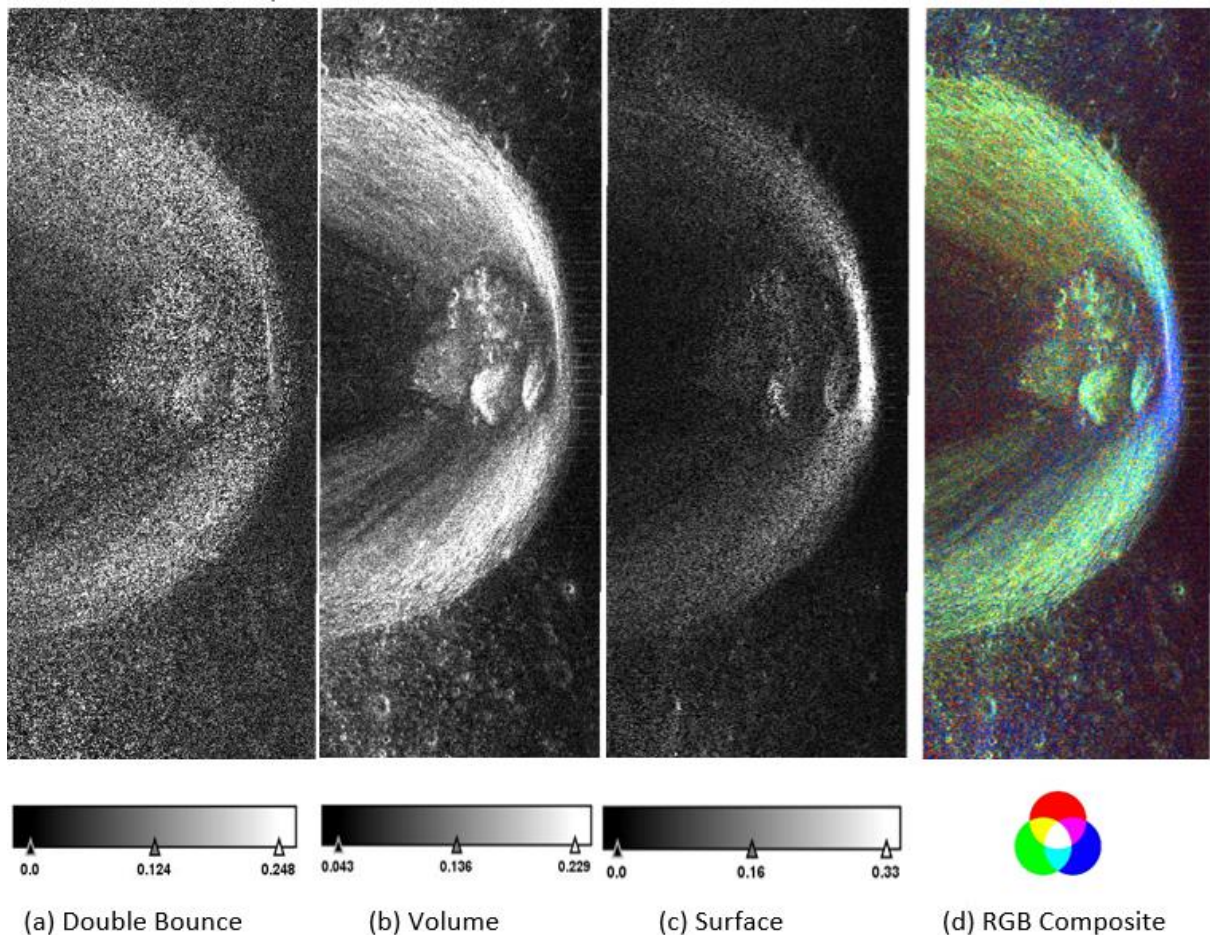(a) Double-bounce   (b) Volume   (c) Surface   (d) RGB Composite
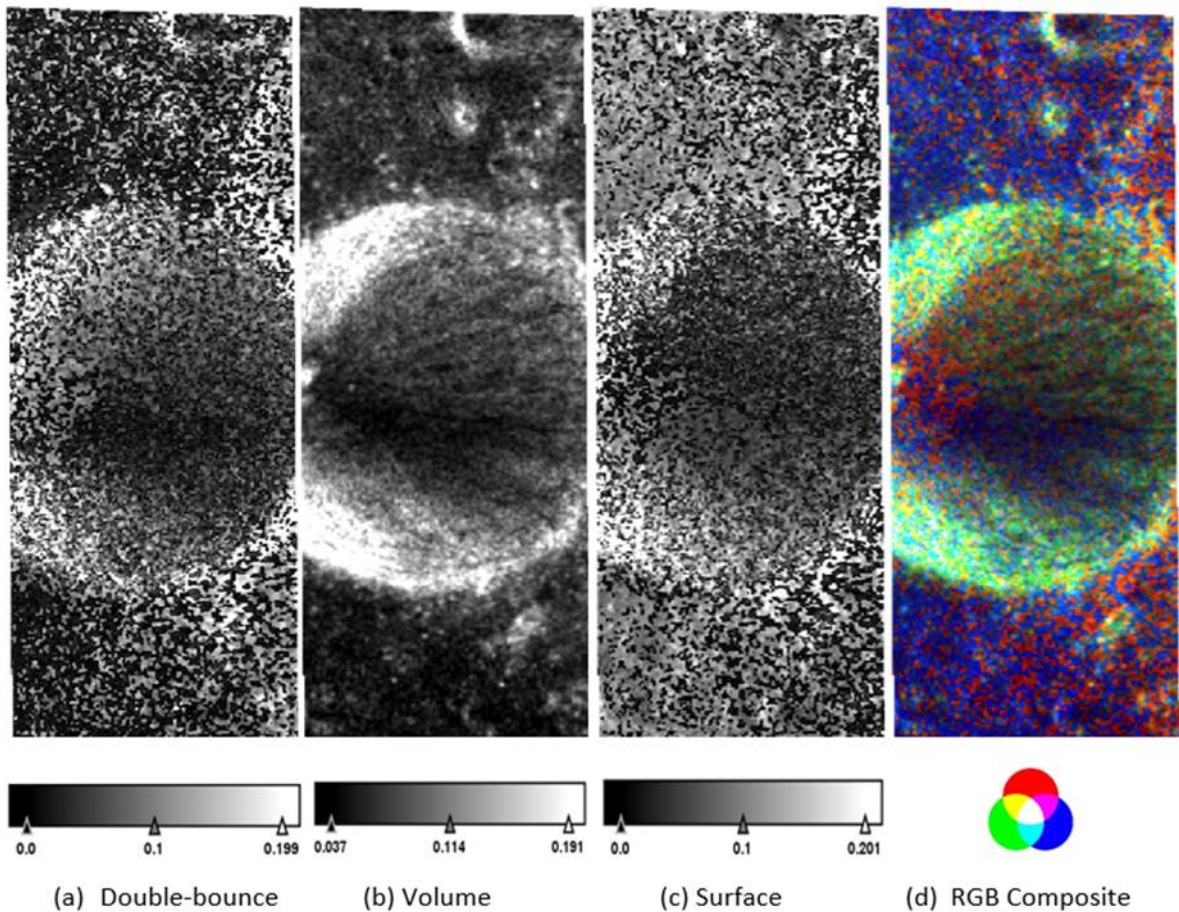
Figure 39 m-delta decomposition of Chandrayaan-1 (Mini-SAR) (a) Double-bounce scattering, (b) Volume scattering ,(c) Surface scattering and (d) RGB colour composite

Figure 39 shows the RGB composite of the m-δ decomposition of the Erlanger crater which shows the dominance of volume scattering in the crater walls, whereas the crater base and the surrounding area around the rim show the dominance of surface scattering and double bounce scattering. The crater base and the surrounding areas are smooth, so the surface scattering is more prominent in these regions. Double-bounce scattering is visible in the crater base and outside the crater rim which can be because of the natural dihedral structure in the surroundings. The mean values of volume scattering are 0.114, for surface and double-bounce it is the same which is 0.1.

5.2.2. m- χ (m-chi) Decomposition
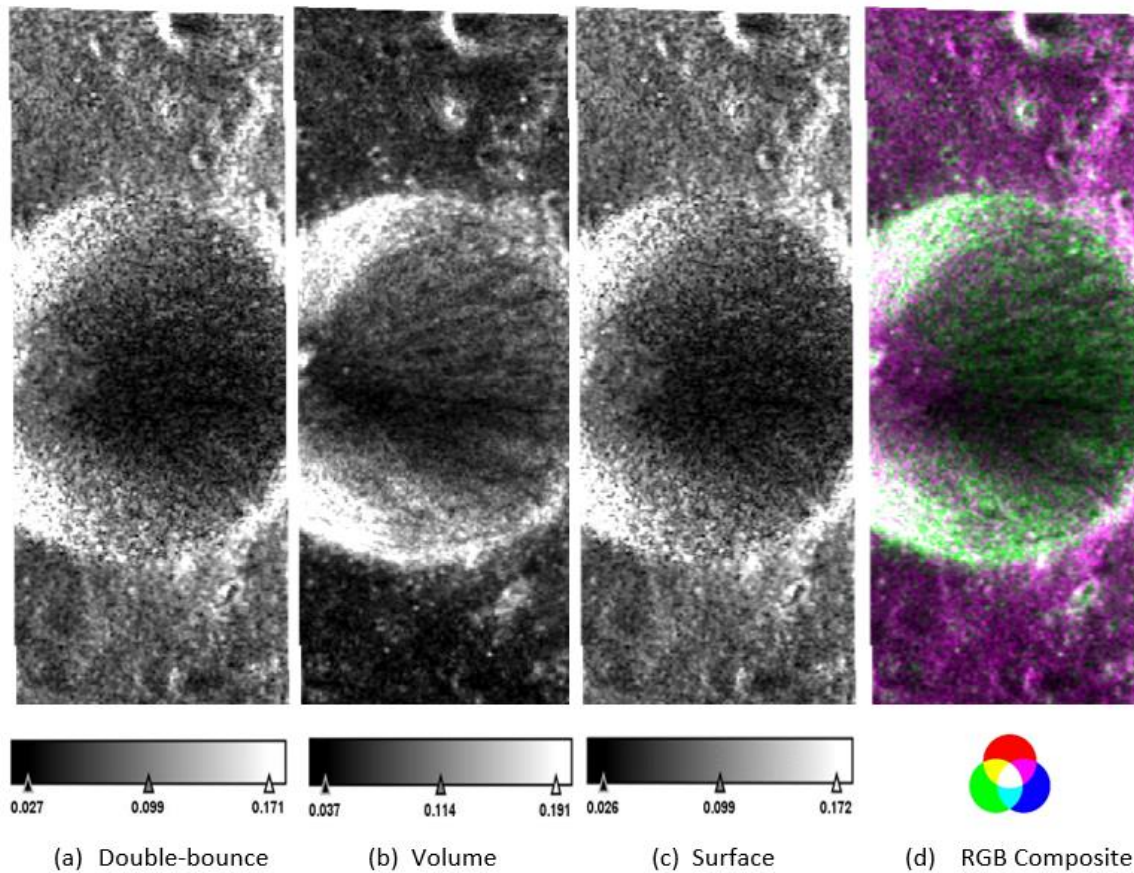
Figure 40 m-chi decomposition of Chandrayaan-1 (Mini-SAR) (a) Double-bounce scattering, (b) Volume scattering ,(c) Surface scattering and (d) RGB colour composite

Figure 40 shows the RGB composite of the m-χ decomposition of the Erlanger crater which shows that the dominance of volume scattering is found in the crater walls suggesting that the walls of the crater are of the rough surface as it was seen in m-δ decomposition. The crater base has double-bounce and surface scattering as in dominance. The Magenta colour in the crater base and the surrounding around the rim show the combination of double-bounce and surface scattering. The mean values of the volume scattering are 0.114 and for double bounce and surface scattering id 0.099 which is the same and was also seen in the m-δ decomposition.
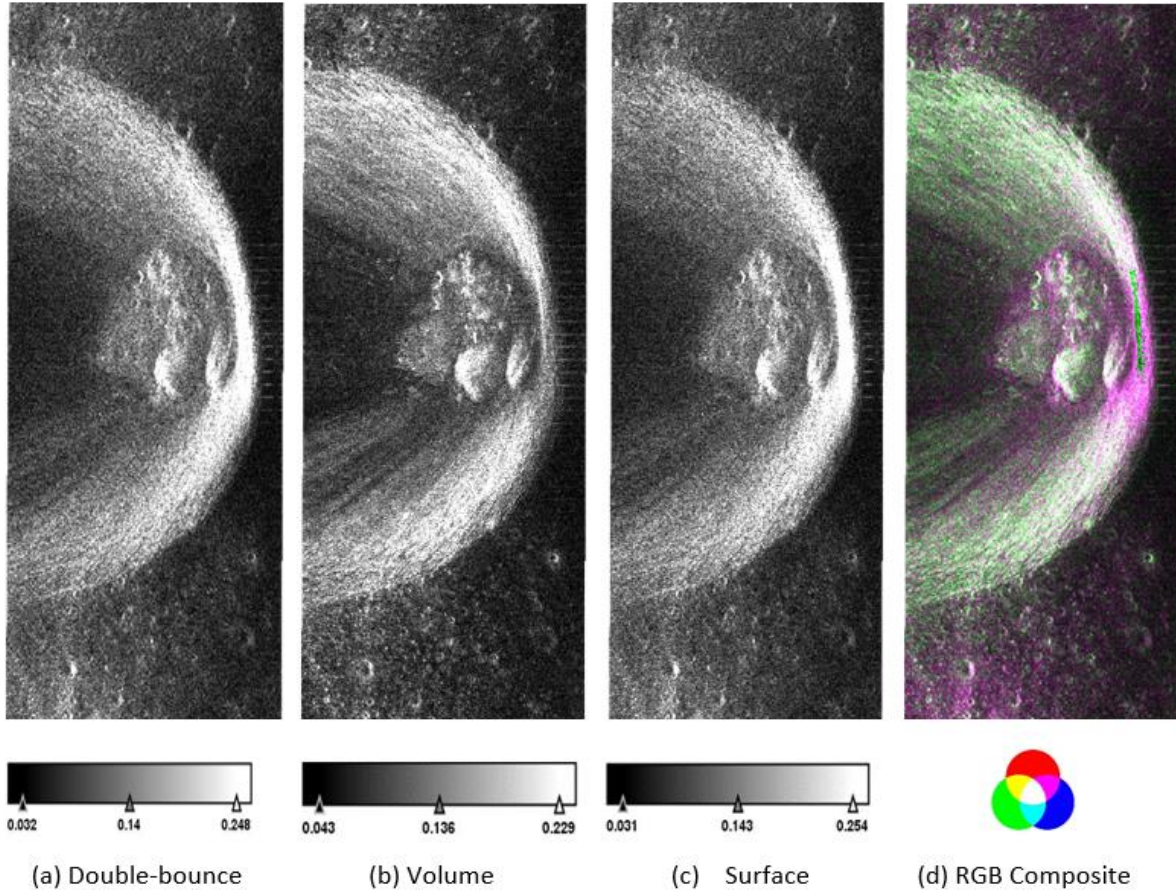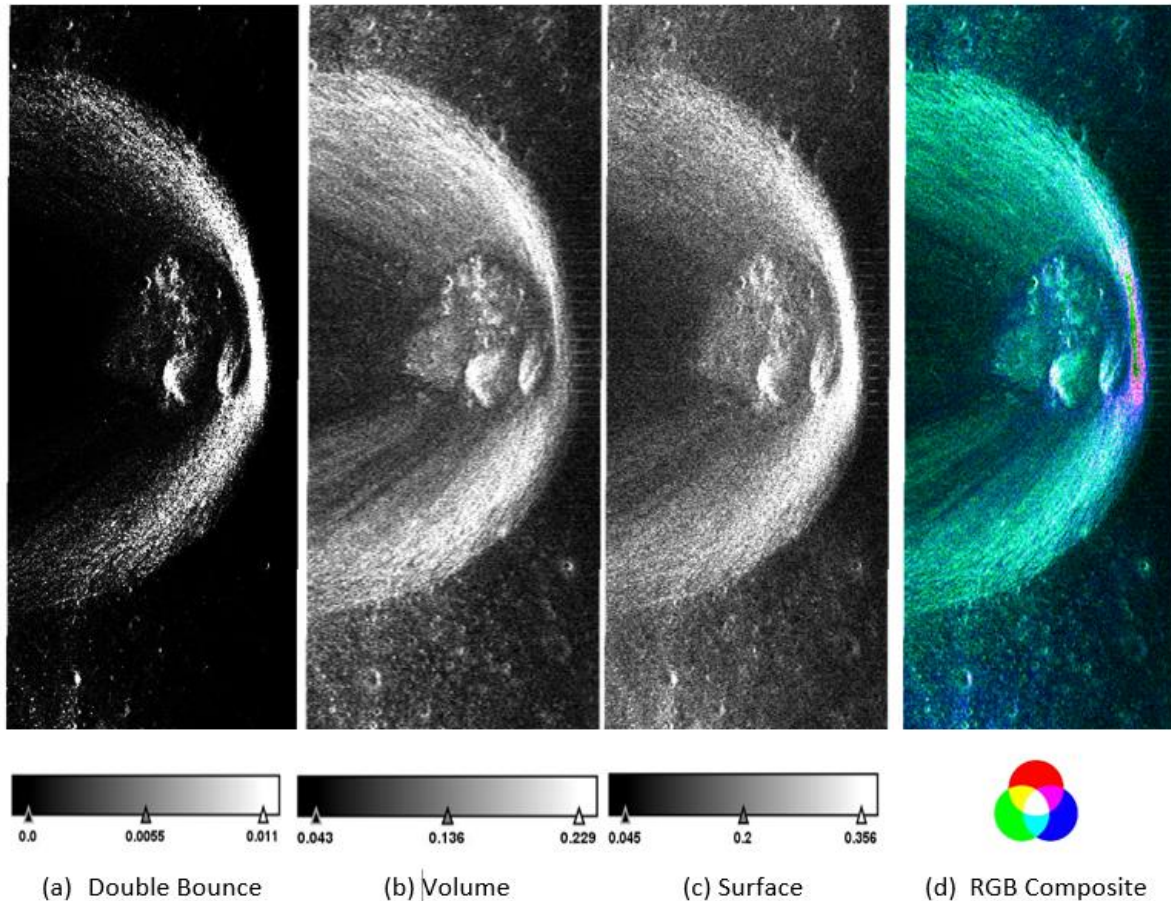
5.2.3. m- α (m-alpha) Decomposition
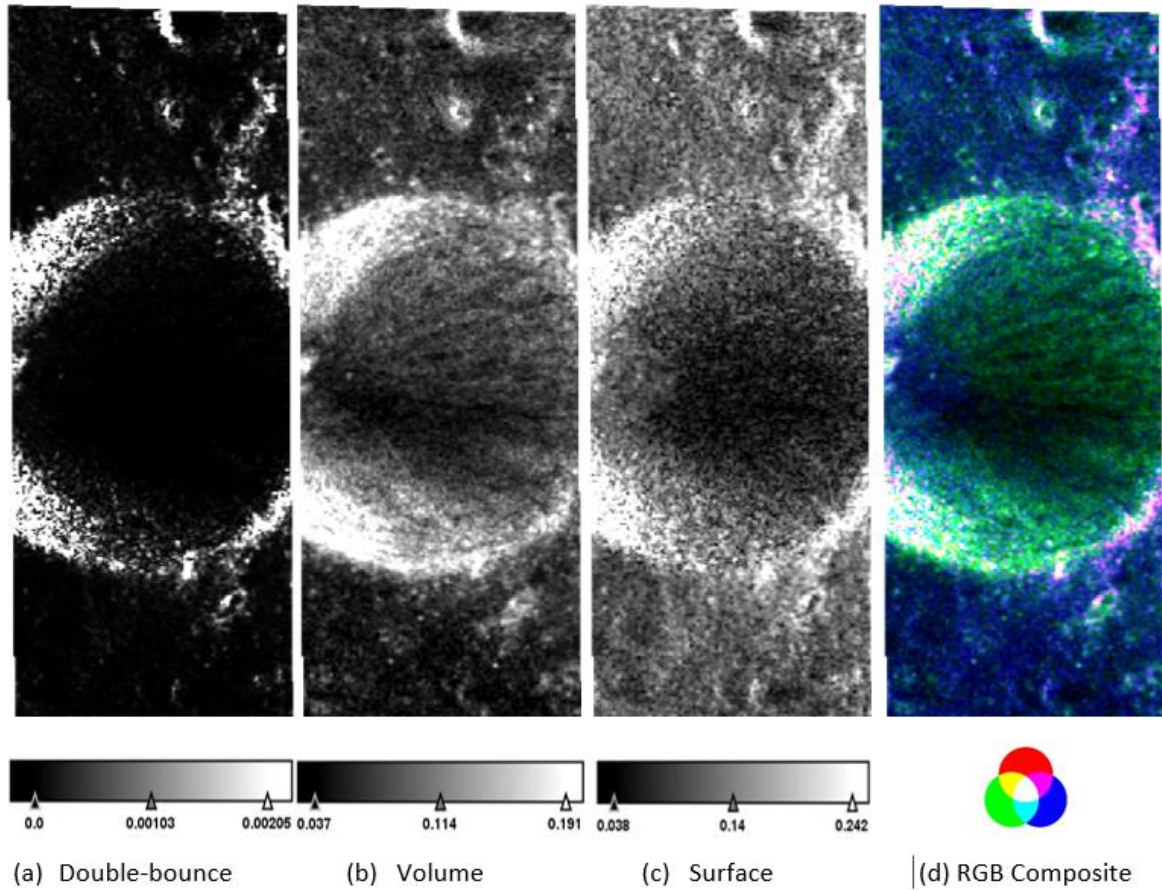
Figure 41 m-alpha decomposition of Chandrayaan-1 (Mini-SAR) (a) Double-bounce scattering, (b) Volume scattering ,(c) Surface scattering and (d) RGB colour composite

Figure 41 shows the RGB composite of m-α decomposition of the Erlanger crater. High volume scattering is seen in the crater walls as it was seen in the other two decompositions i.e., m-δ and m-χ. But in this, the crater base shows the dominance of surface scattering, and it is also seen on the outside of the crater rim. A very small scattering of double bounce is seen in the rim connected to the crater which can be because of the presence of natural dihedral in the region. The small craters in the region outside the crater also show volume scattering whereas, the surface scattering outside the crater shows the area to be smooth which was not in the case of the other two decompositions. The mean values of volume scattering are 0.114 which is similar in all the decompositions and the surface scattering is 0.14 whereas the mean values of double scattering are very low which is 0.00103.

5.2.4. Barnes Decomposition

Figure 42 Barnes decomposition for Chandrayaan-2(DFSAR) (a) Full scene of the data covering Erlanger crater (b) Zoomed view of the two PSR region (c) Zoomed view of Erlanger crater

Figure 42 shows the RGB composite image of Barnes Decomposition of the scene covering Erlanger crater of DFSAR of Chandrayaan-2 data. Figure 42(a) shows the scene which covers three PSR regions including the PSR region of the Erlanger crater. Figure 42(b) shows the zoomed version of the scene of the two PSR whose in which the crater which is encircled in black whose PSR_ID is NP_877350_0169810 and the crater which is encircled in blue in the scene whose PSR_ID is NP_875450_0179490 which is shown to clearly distinguish the crater and its scattering mechanism. Figure 42(c) shows the zoomed image of the Erlanger crater whose PSR_ID is NP_869610_0287570. The wall of the crater shows volume scattering in dominance depicting the crater walls to be of a rough surface. The floor of the crater shows the surface scattering which is seen in blue colour, which also depicts that the floor is smooth which was also seen from the other

decomposition techniques used on the S-band of Mini-SAR and Mini-RF. The walls also show some regions to be in blue colour which gives an interpretation that some regions in the crater walls are smooth. The area outside the crater rim shows the ejecta of the crater which is seen in green colour depicting volume scattering in these regions. The scene also shows different craters which can be easily identified as in green colour and some regions show blue colour which are smooth in nature.

5.2.5. H- A- α Decomposition

Figure 43 Parameters of eigenvalue and eigenvector based decomposition and polarimetric decomposition (a) Entropy, (b) Alpha angle, (c) Anisotropy (d) H-A-Alpha decomposition

The above figure 43 shows the Entropy, Alpha and Anisotropy derived from the H-A-alpha decomposition. To characterize the Erlanger crater and the other two PSR regions which are in the scene, these are the polarimetric parameters that are used. The RGB composite image of the H-A-Alpha decomposition has also been used to differentiate the scattering present in the scene and the crater. As it was seen in the Barnes decomposition of this scene the crater gives the dominance of the volume scattering present in the walls and the floor of the crater which is in green colour. This gives an interpretation of the rough surface present in the crater. A very small portion in the crater floor gives surface scattering and a mix of double bounce scattering in crater floor. This gives an idea about the crater floor which is smooth on the surface in comparison to the crater walls. The other small craters in the scene which covers the PSR are also identified which gives volume scattering and the area which is in blue gives the interpretation about the surface to be smooth, which is surface scattering. The eigenvector-eigenvalue parameters Entropy and Alpha angle also go well with the results obtained from Barnes decomposition and H-A-Alpha decomposition models. The entropy values in the crater are higher and are around 1 in the crater region, which corresponds that it is because of the volume scattering present in the crater, but the crater floor gives low entropy. The value of the alpha angle is around 45° in the crater walls which again corresponds to volume scattering present in the crater. This supports the results of the decomposition technique obtained in the form of the dominance of volumetric scattering. The value of Anisotropy in the major portion of the crater is zero which represents that the scattering is obtained from three pure targets. With these results, it can be withdrawn that the crater shows volume scattering in all the datasets and the decomposition models that were applied.

5.2.6. Analysis of Circular Polarization Ratio (CPR)
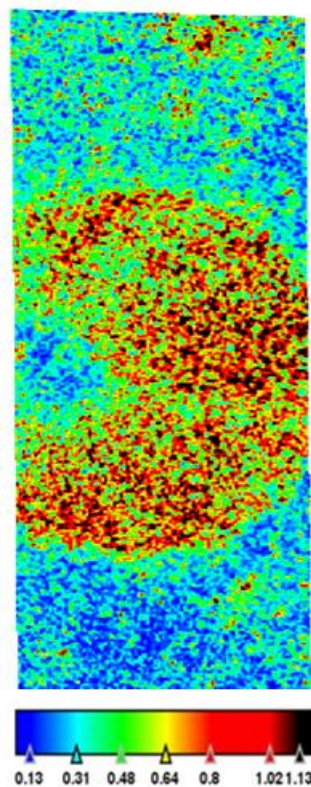
Figure 44 Value of CPR for
Erlanger crater for LRO (Mini-RF)

Figure 44 shows the values of CPR in the crater. The high values of CPR, which is more than 1 in the Erlanger crater depict that the crater has some areas which can be a probable location of water ice deposits. The values which are below 1 relate to the lunar regolith and other materials. The high values of CPR can be also due to the scattering by the rough surface, which can be because of double bounce scattering or volume scattering. The locations of the crater walls show high CPR which is close to 1.02 to 1.13 particularly in the crater walls but not on the floor of the crater. The areas outside of the crater show a low CPR value which can be caused due to the surface scattering.

5.3. Characterization of Slater Crater

The scene which covers the Slater crater is of L-band DFSAR of Chandrayaan-2 and as is earlier stated that this region lies in PSR of the lunar South Pole.
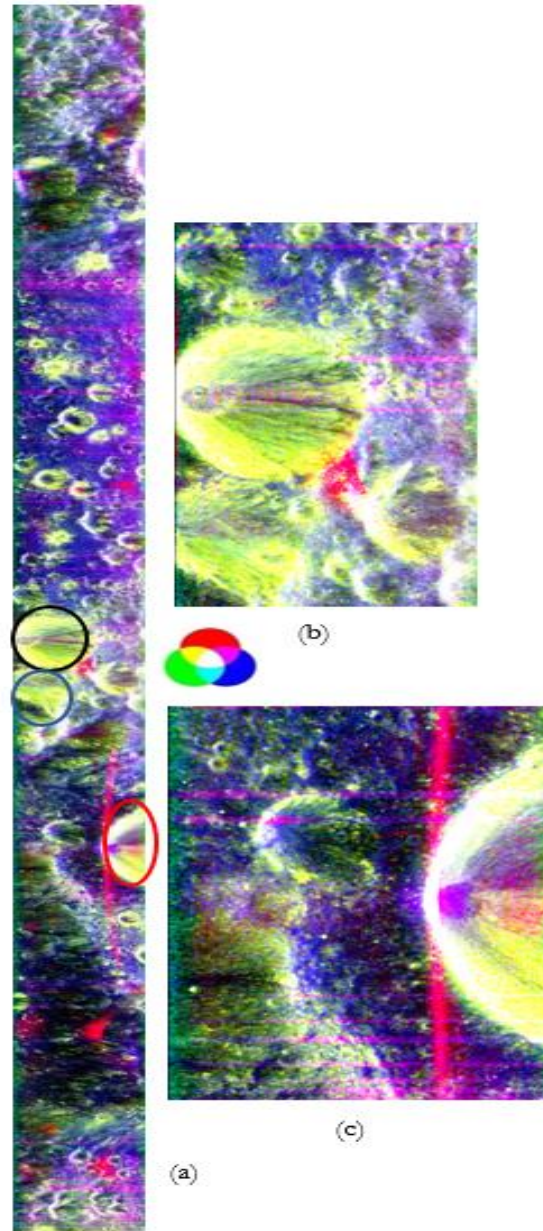
5.3.1. Barnes Decomposition
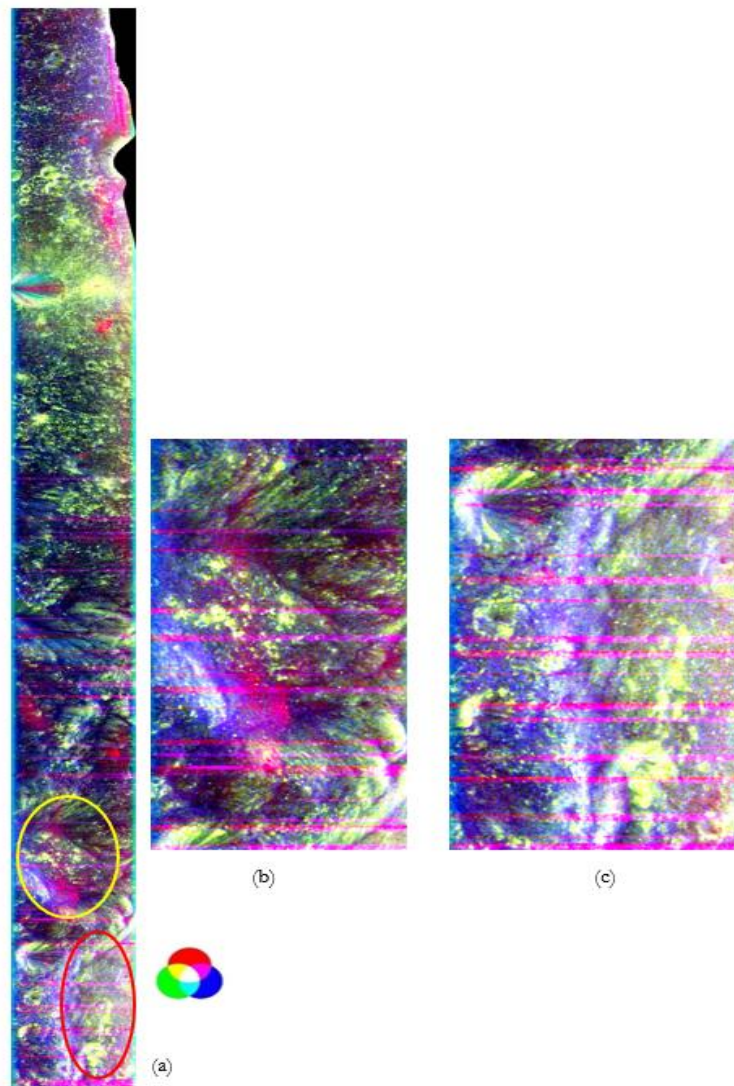
Figure 45 Barnes decomposition for Chandrayaan-2(DFSAR) (a) Full scene of the data covering Slater crater (b) Zoomed view of the PSR region (c) Zoomed view of Slater crater

Figure 45 shows the RGB composite image of Barnes Decomposition of the scene covering the Slater crater of DFSAR of Chandrayaan-2 data. Figure 45(a) shows the scene which covers two PSR regions including the PSR region of the Slater crater. Figure 45(b) shows the zoomed version of the scene of the PSR which is encircled in yellow whose PSR_ID is SP_88100_1147820 which is shown to clearly distinguish the crater and its scattering mechanism. Figure 45(c) shows the zoomed image of the Slater crater whose PSR_ID is SP_874430_1188390. The wall of the crater shows volume scattering depicting the crater walls to be of a rough surface and some areas of the walls depict surface scattering. The floor of the crater shows volume scattering which is seen in green colour, which also depicts that the floor is rough. The PSR_ID SP_88100_1147820 shows volume scattering in the crater floor and also in the crater walls which depicts that these regions are rough.
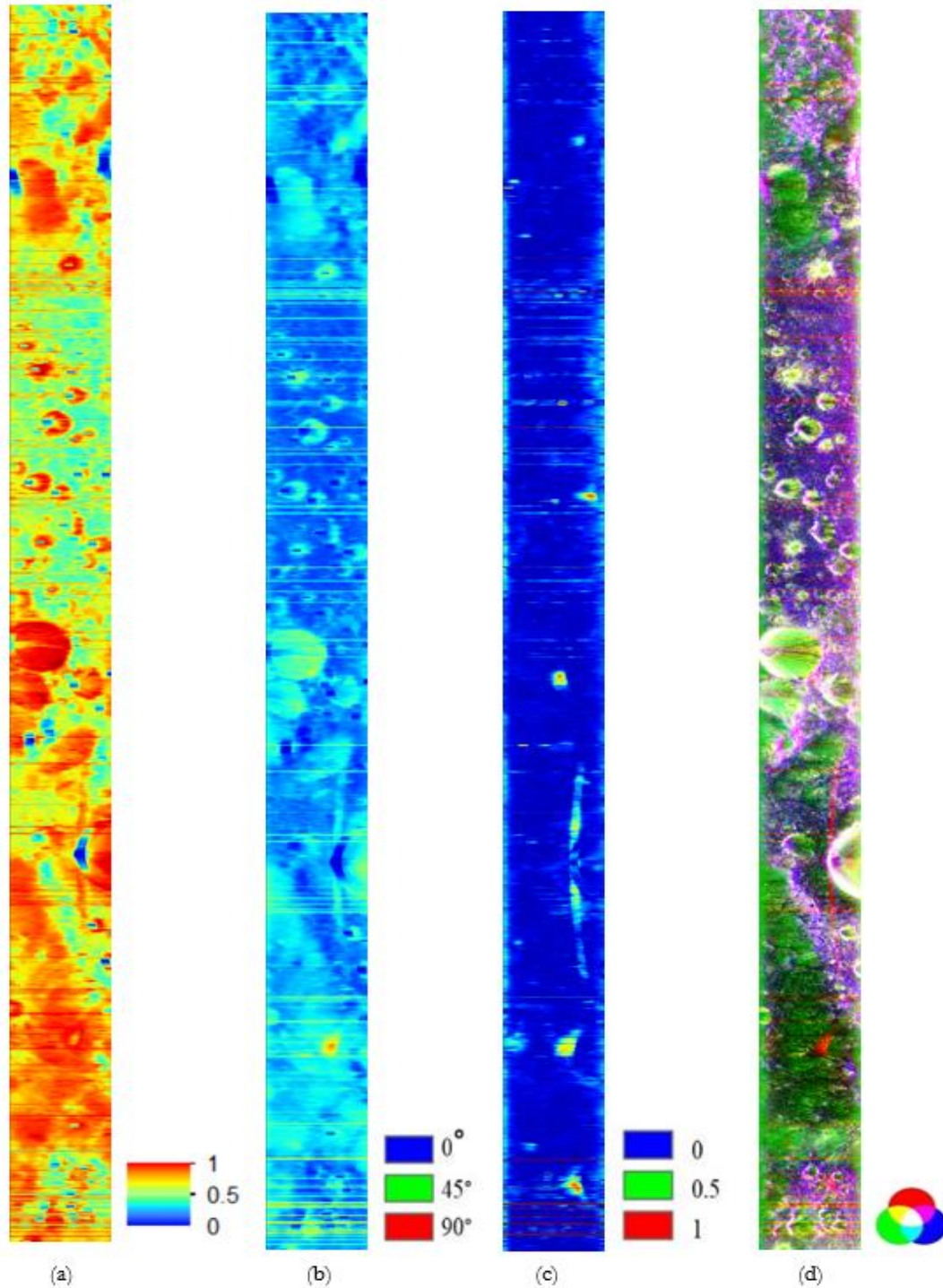
5.3.2. H-A-Alpha Decomposition

Figure 46 Parameters of eigenvalue and eigenvector based decomposition and polarimetric decomposition (a) Entropy, (b) Alpha angle, (c) Anisotropy (d) H-A-Alpha decomposition

The above figure 46 shows the Entropy, Alpha and Anisotropy derived from the H-A-alpha decomposition. To characterize the Slater crater and the other PSR region which is in the scene, these are the polarimetric parameters that are used. The RGB composite image of the H-A-Alpha decomposition has also been used to differentiate the scattering present in the scene and the crater. As it was seen in the Barnes decomposition of this scene the crater gives the dominance of the volume scattering present in the walls and the floor of the crater which is in green colour. This gives an interpretation of the rough surface present in the crater. A very small portion in the crater walls gives surface scattering. This gives an idea about the crater floor which is smooth on the surface in comparison to the other region of the crater walls. The other small craters in the scene are also identified which gives volume scattering and the area which is in blue gives the interpretation about the surface to be smooth, which is surface scattering. The eigenvector-eigenvalue parameters Entropy and Alpha angle also go well with the results obtained from Barnes decomposition and H-A-Alpha decomposition models. The entropy values in the crater are higher and are around 1 in the crater region, which corresponds that it is because of the volume scattering present in the crater, but the walls gives low entropy. The value of the alpha angle is around 45° in some regions of the crater floor which again corresponds to volume scattering present in the crater and the crater walls give 0°. This supports the results of the decomposition technique obtained in the form of the dominance of volumetric scattering. The value of Anisotropy in the major portion of the crater is zero which represents that the scattering is obtained from three pure targets. With these results, it can be withdrawn that the crater shows volume scattering in all the decomposition models that were applied.

5.4. Characterization of Cabeus Crater

The Cabesus crater is situated at the South Pole on the lunar surface. Some part of this crater lies in the PSR region. For Fully polarimetric data of DFSAR of Chandrayaan-2, the Barnes decomposition technique and the H-A-α decomposition technique has been used to analyze the different polarimetric parameters.

5.4.1. Barnes Decomposition
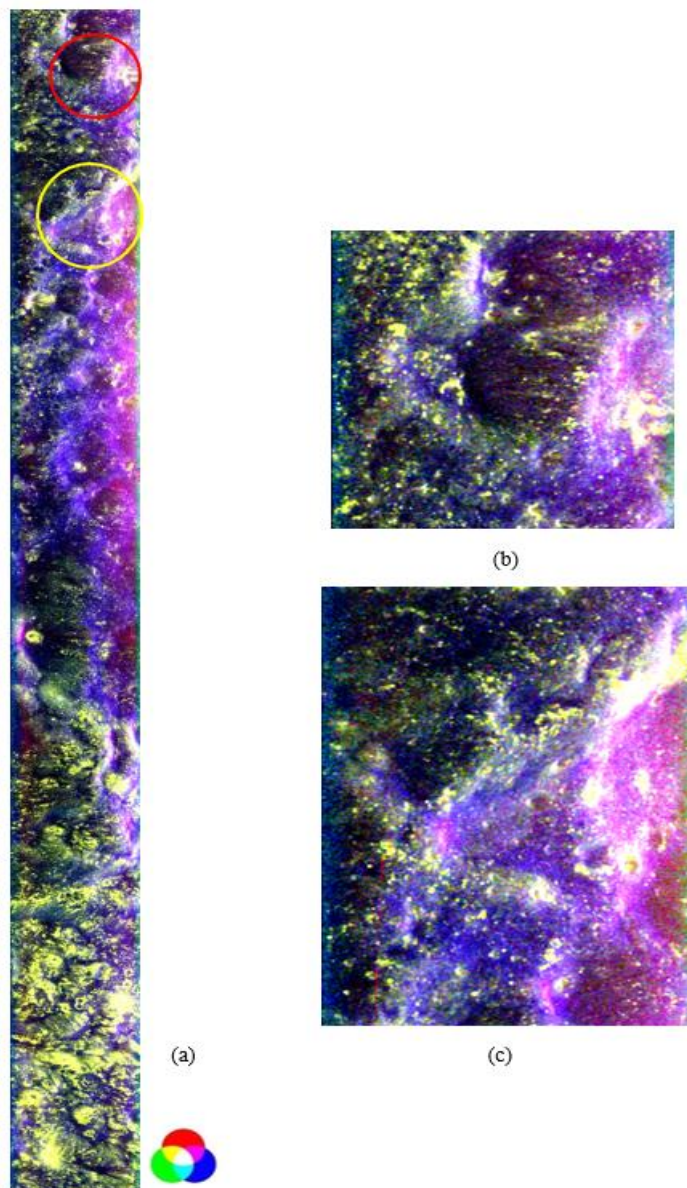
Figure 47 Barnes decomposition for Chandrayaan-2(DFSAR) (a) Full scene of the data covering Cabeus crater (b) Zoomed view of first PSR of Cabeus (c) Zoomed view of second PSR of Cabeus crater

Fig. shows 47 the RGB composite image of the scene covering the two PSR regions of the Cabeus crater of Barnes decomposition for the DFSAR of Chandrayaan-2 data in L-band. This decomposition shows the scatterin characteristics of the PSR region of the crater. The region encircled in yellow is the first PSR region with the PSR ID SP_849040_3196480 and its zoomed image is shown in Figure 47(b). The second PSR region is encircled in yellow in Figure 47 (a) and whose PSR ID is SP_853600_3177620 and its zoomed

image is shown in Figure 47(c). In the first PSR region, a mix of double-bounce and surface scattering is seen and a very small portion in the crater floor is seen with volume scattering. The second PSR region shows that the surface scattering and double-bounce scattering in the region. The magenta colour in this region shows the double-bounce and surface scattering which can be caused due to the presence of natural dihedral reflectors present in the region of this crater. A very small portion in the wall of this crater shows the presence of volume scattering which shows that a very small area of the crater wall is rough. The lack of volume scattering in the PSR region gives the crater for further analysis in the decomposition with polarimetric parameters to be studied.
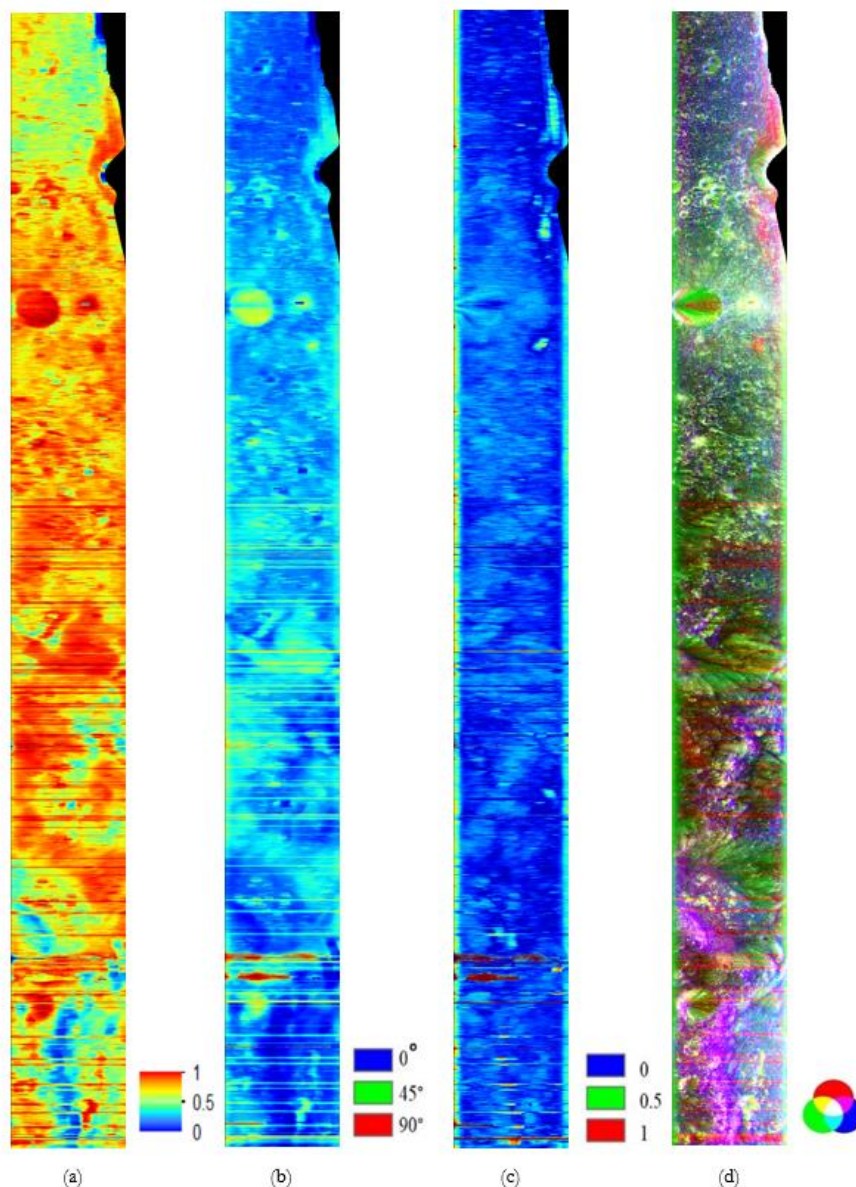
5.4.2. H- A-α Decomposition
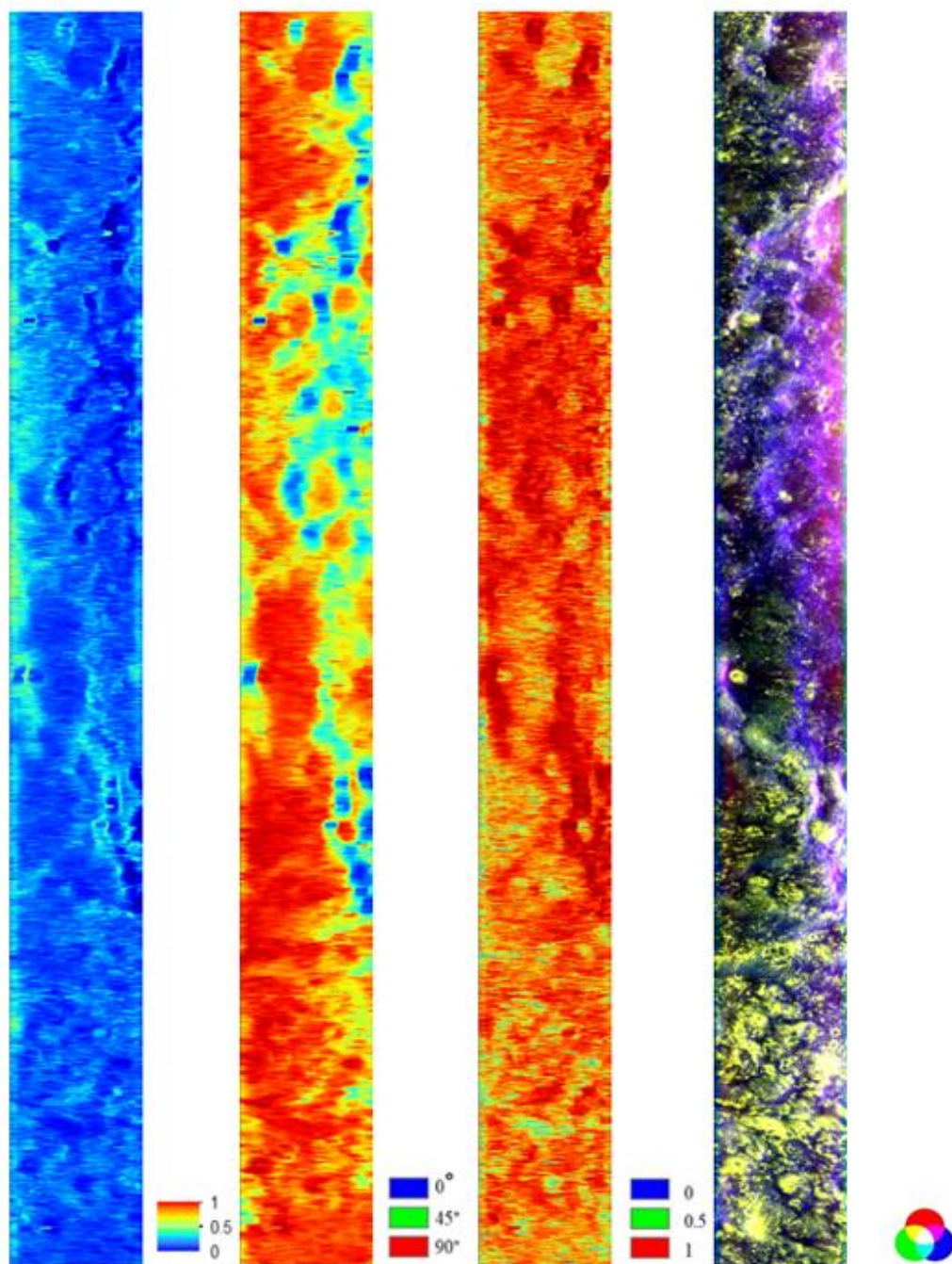
Figure 48 Parameters of eigenvalue and eigenvector based decomposition and polarimetric decomposition (a) Entropy, (b) Alpha angle, (c) Anisotropy (d) H-A-Alpha decomposition

The above figure 48 shows the Entropy, Alpha and Anisotropy derived from the H-A-alpha decomposition. To characterize the Cabeus crater, these are the polarimetric parameters that are used. The RGB composite image of the H-A-Alpha decomposition has also been used to differentiate the scattering present in the scene and the PSR region of the crater. As it was seen in the Barnes decomposition of this scene the crater gives the dominance of the mix of double-bounce and surface scattering. A very small portion in the crater floor gives volume scattering in the first PSR region in the crater floor and the second PSR region of the crater walls give volume scattering. Overall, it can be said that the crater does not show volume scattering in dominance. The other regions in the scene are also identified which gives volume scattering and the area which is in blue gives the interpretation about the surface to be smooth, which is surface scattering. The eigenvector-eigenvalue parameters Entropy and Alpha angle also go well with the results obtained from Barnes decomposition and H-A-Alpha decomposition models. The entropy values in the crater are very low and are around 0 or less than 0.5 in the crater region, which corresponds that it is because of the surface scattering present in the crater. The value of the alpha angle is around 0° in the major portion of the crater region which again corresponds to surface scattering present in the crater. This supports the results of the decomposition technique obtained in the form of the dominance of surface scattering. The value of Anisotropy in the major portion of the crater is 1 represents that the scattering is obtained from only a single target. With these results, it can be withdrawn that the crater shows surface scattering in the major areas of the crater and in the decomposition models that were applied.

5.5. Characterization of Hermite-A Crater

Hermite-A crater is a small crater which is situated near the Hermite crater in the North Pole. Hermite-A does lie in the PSR region. The characterization of this crater is on three decomposition techniques and CPR for Hybrid Pol data of Chandrayaan-1 and LRO which is of S-band. For Fully polarimetric data of DFSAR of Chandrayaan-2, Barnes decomposition and the H-A-α decomposition technique has been used to analyze the different polarimetric parameters.

5.5.1. m-δ (m-delta) Decomposition

In this decomposition, the analysis is being made based on three scattering mechanisms which are surface, double-bounce, and volume scattering. The RGB composite image from all these scattering mechanisms has been made for the crater to analyze the scattering pattern and the extent of ejecta around the rim of the crater. The colours like cyan, magenta, and yellow have been included to indicate the mixing of the scattering patterns.

Figure 49 m-delta decomposition of Chandrayaan-1 (Mini-SAR) (a) Double-bounce scattering, (b) Volume scattering ,(c) Surface scattering and (d) RGB colour composite

Figure 49 shows the RGB composite of the m-δ decomposition done for the Mini-SAR of Chandrayaan-1 data for the Hermite-A crater which shows the dominance of volume scattering in the crater walls, whereas a small region in the crater base shows the domination of surface scattering and double bounce scattering and is also seen around the areas which surround the crater rim. The crater base and the surrounding areas

are smooth, so the surface scattering is more prominent in these regions. It is evident that volume scattering is visible as a small peak in the crater floor, while double-bounce scattering is evident in the crater base and outside the crater rim which can be because of the natural dihedral structure in the surroundings. The mean values of volume scattering are 0.136, for the surface, it is 0.125 and for double-bounce, it is 0.117.

LRO (Mini-RF)

Figure 50 m-delta decomposition of LRO (Mini-RF) (a) Double-bounce scattering, (b) Volume scattering,(c) Surface scattering and (d) RGB colour composite

Figure 50 shows the RGB composite of the m- δ decomposition of the Hermite-A crater seen from Mini-RF from LRO, which shows that the dominance of volume scattering is found in the crater walls suggesting that the walls of the crater are of the rough surface as it was seen in the m-δ decomposition of the Mini-SAR data. The crater base also has double-bounce and surface scattering in some of the regions, but the small peak present in the crater base is showing volume scattering and some of the regions of the crater walls are showing both double-bounce and surface scattering. The crater walls are clearly showing all the scattering and the crater walls, but volume scattering is seen as a dominant scattering. The Magenta colour in the crater base and the area surrounding the rim shows the mix of double-bounce and surface scattering. The volume scattering gives the mean values around 0.219 and whereas, for double-bounce it is 0.19 which is the lowest and for surface scattering is 0.2.

5.5.2. m-chi decomposition

Chandrayaan-1 (Mini-SAR)

Figure 51 m-chi decomposition of Chandrayaan-1 (Mini-SAR) (a) Double-bounce scattering, (b) Volume scattering, (c) Surface scattering and (d) RGB colour composite

Figure 51 shows the three scattering mechanisms along with the RGB composite done for the Mini-SAR of Chandrayaan-1 data by m-χ decomposition for the Hermite-A crater which shows the dominance of volume scattering in the crater walls suggesting that the walls of the crater are of the rough surface as it was seen in the m-δ decomposition of Mini-SAR and Mini-RF data. The crater base has double-bounce and surface scattering as in dominance, but the small peak present in the crater base is showing volume scattering. The crater walls are clearly showing all the scattering and the crater walls are much visible in this decomposition technique in comparison to the m-delta decomposition. The Magenta colour in the crater base and the surrounding around the rim show the mix of surface scattering and double-bounce scattering. The volume scattering gives the mean values around 0.136 and 0.117 for double-bounce scattering and surface scattering is 0.118 which is the nearly same.

LRO (Mini-RF)
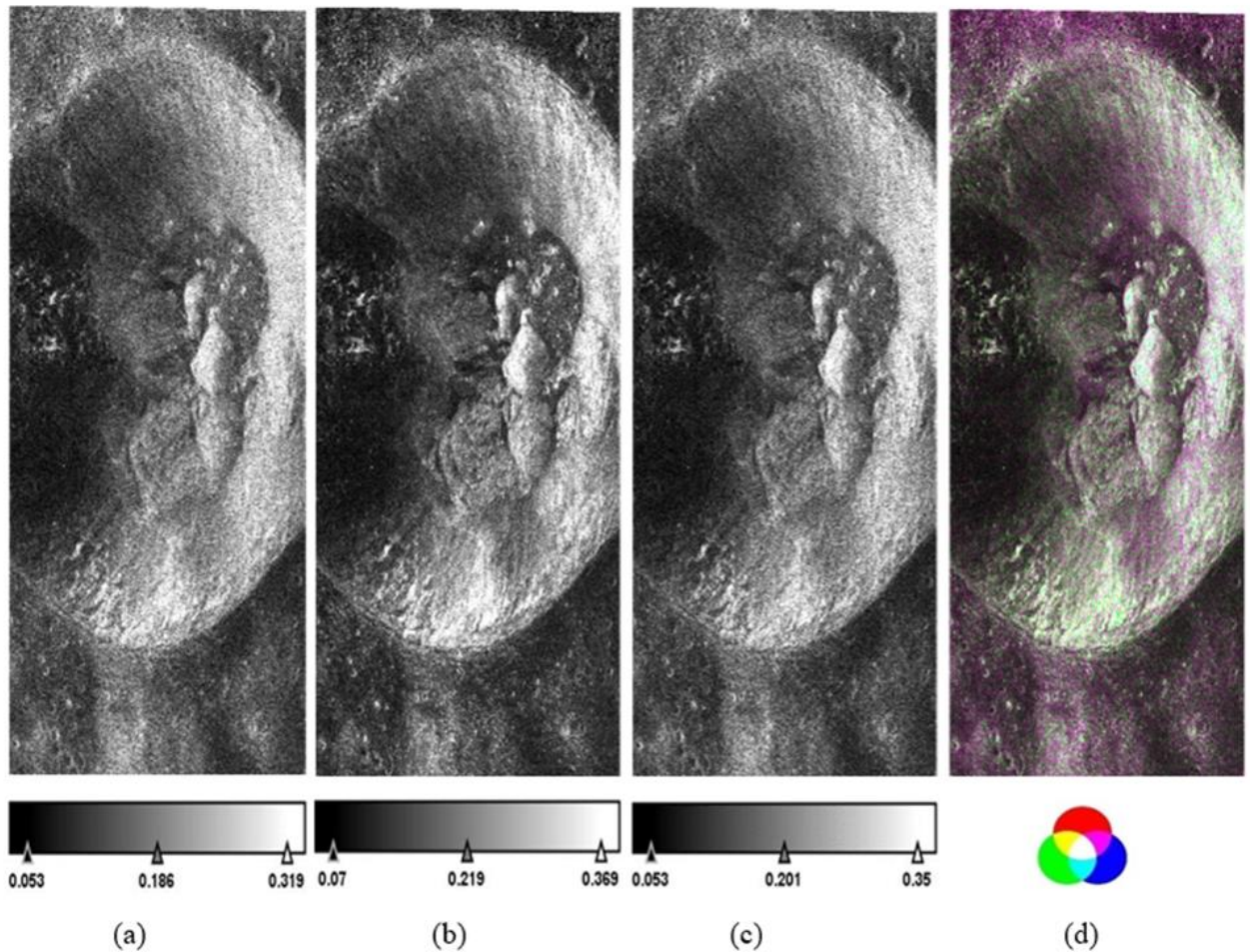
Figure 52 m-chi decomposition of LRO (Mini-RF) (a) Double-bounce scattering, (b) Volume scattering,(c) Surface scattering and (d) RGB colour composite

Figure 52 shows the three scattering mechanisms along with the RGB composite done for the Mini-RF data of LRO by m-χ decomposition for the Hermite-A crater which shows the dominance of volume scattering in the crater walls suggesting that the walls of the crater are of the rough surface as it was seen in the m-δ decomposition of Mini-SAR and Mini-RF data, along with the m-χ decomposition for the same. The double-bounce and surface scattering is seen in the crater base in some of the regions, but the volume scattering is seen in the peak situated at the crater base and some of the regions of the crater walls are showing both double bounce and surface scattering. The crater walls are clearly showing all the scattering and the crater walls, but volume scattering is seen as a dominant scattering. The Magenta colour in the crater base and the surrounding around the rim show the combination of double-bounce and surface scattering. The volume scattering gives the mean values around 0.219 and 0.186 for double-bounce scattering which is the lowest and for surface scattering is 0.201.

5.5.3. m- α (m-alpha) Decomposition
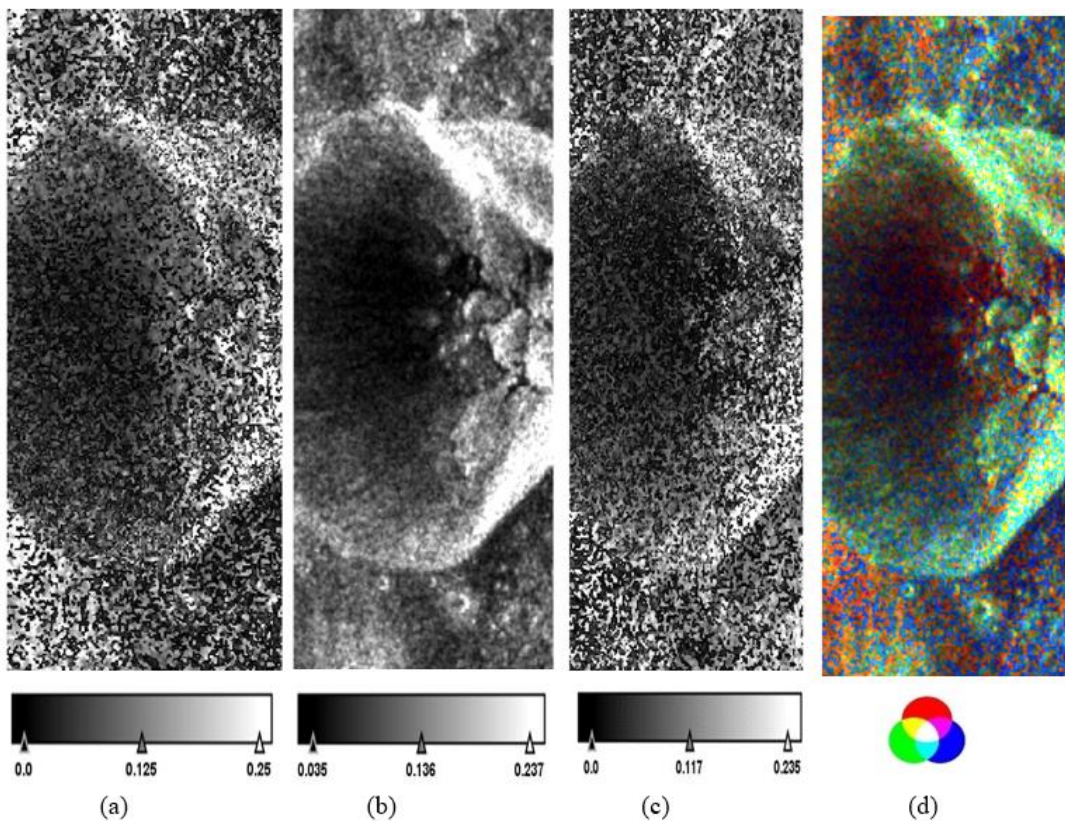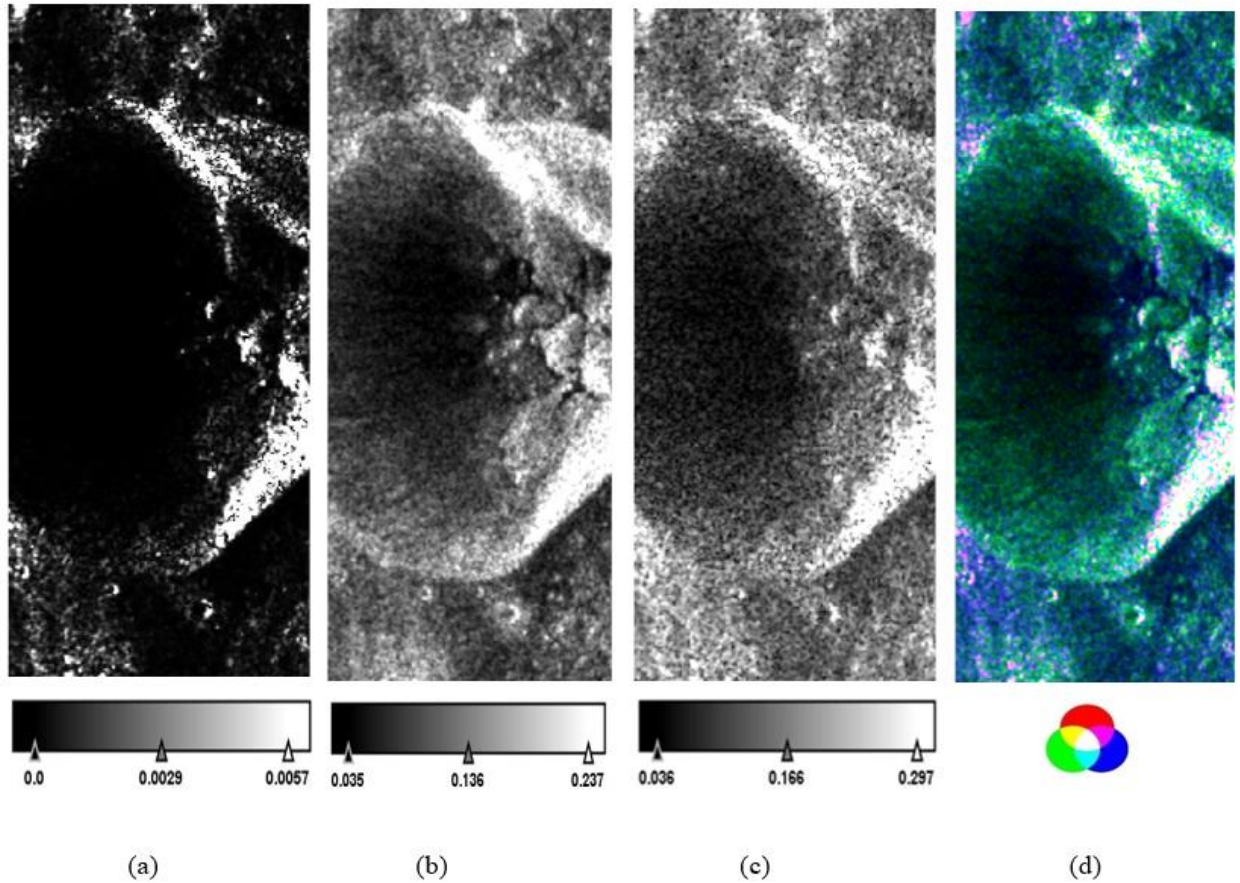

Figure 53 m-alpha decomposition of Chandrayaan-1 (Mini-SAR) (a) Double-bounce scattering, (b) Volume scattering,(c) Surface scattering and (d) RGB colour composite

Figure 53 shows the three scattering mechanisms along with the RGB composite done for the Mini-SAR of Chandrayaan-1 data by m-α decomposition for the Hermite-A crater which shows the dominance of volume scattering in the crater walls suggesting that the walls of the crater are of the rough surface as it was seen in m-δ and m-χ decomposition of Mini-SAR and Mini-RF data. But in this, the crater base shows the dominance of surface scattering, and it is also seen on the outside of the crater rim. A very small scattering of double bounce is seen in the rim connected to the crater which can be because of the presence of natural dihedral in the region. The peak in the crater base also shows the volume scattering. The small craters in the region outside the crater also show volume scattering whereas, the surface scattering outside the crater shows the area to be smooth which was not in the case of the other two decompositions. The mean values of volume scattering are 0.136 which is similar in all the decompositions and the surface scattering is 0.166 which is high from the volume scattering whereas the mean values of double scattering are very low which is 0.0029.

LRO (Mini-RF)

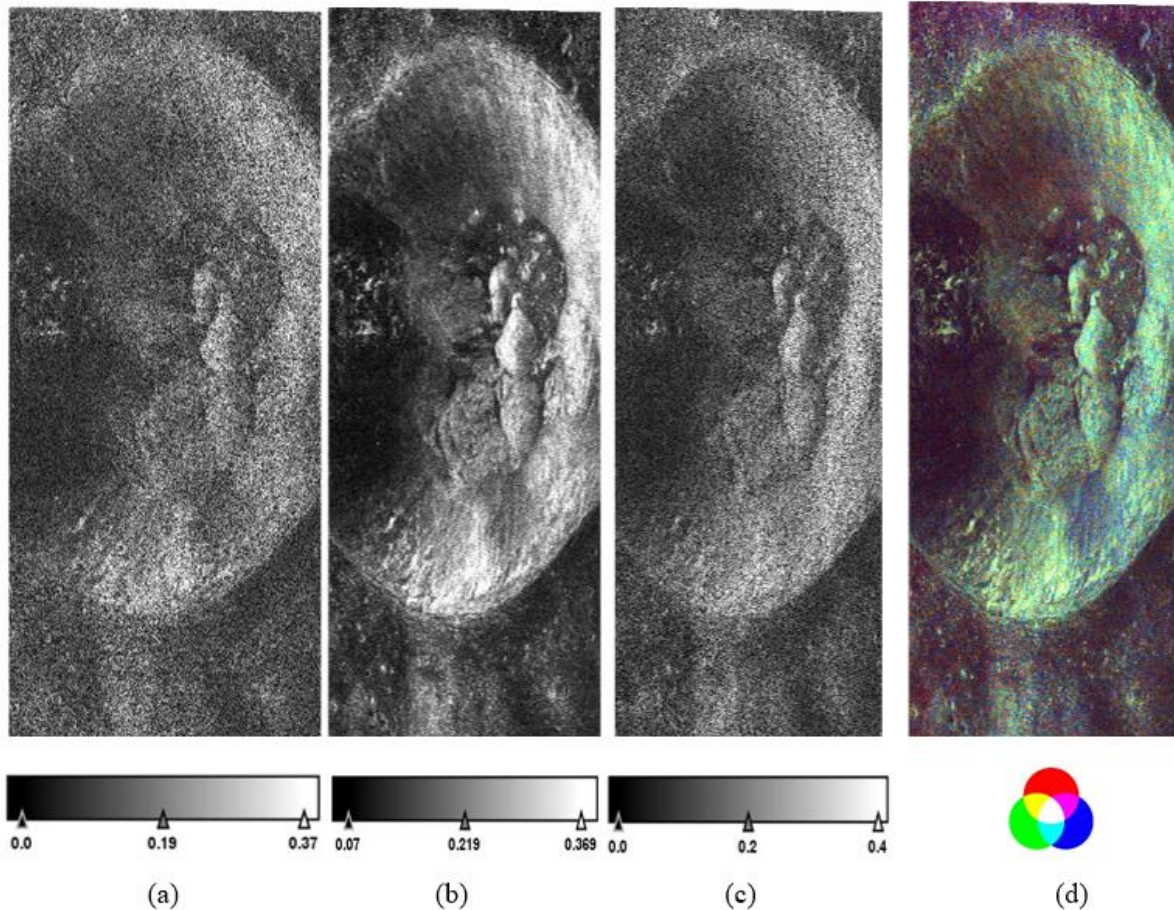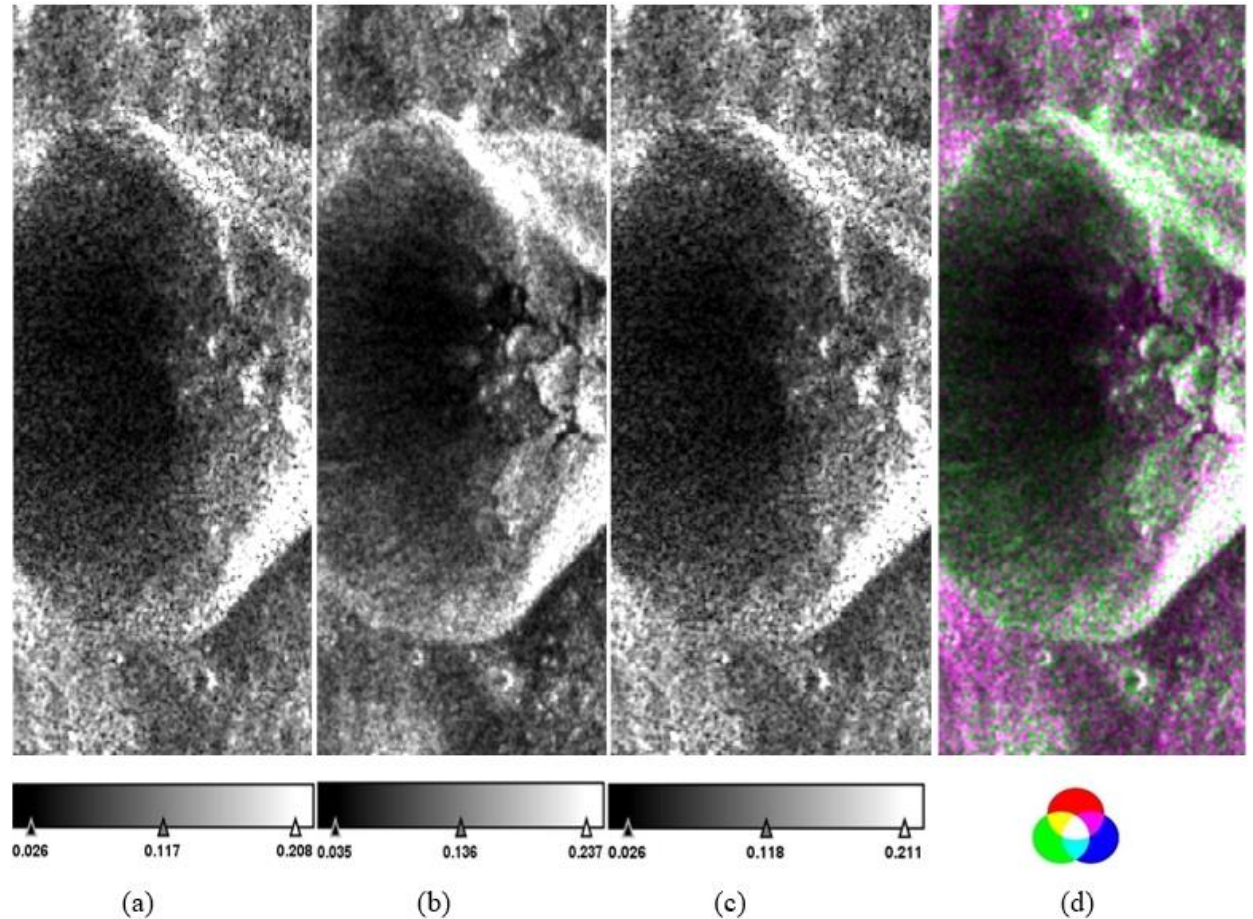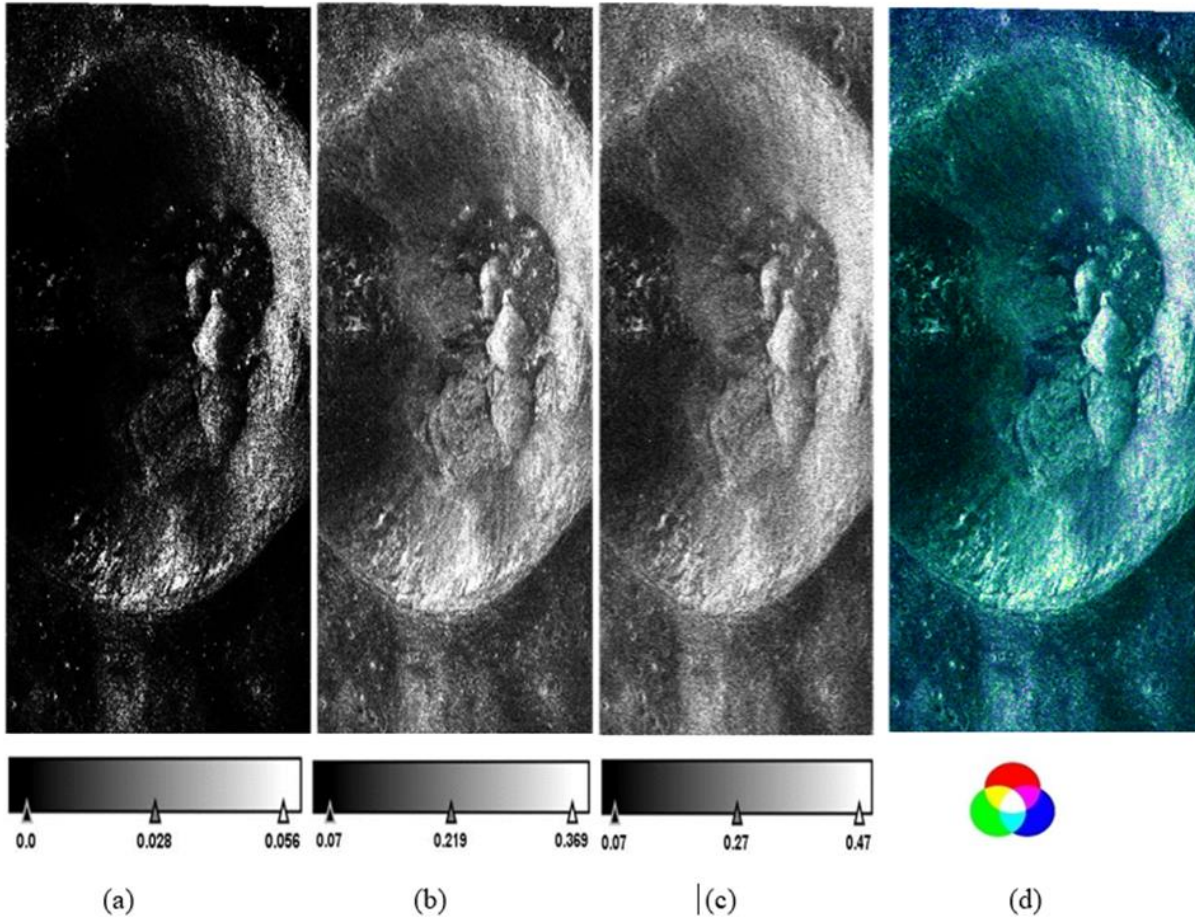

Figure 54 m-alpha decomposition of LRO (Mini-RF) (a) Double-bounce scattering, (b) Volume scattering,(c) Surface scattering and (d) RGB colour composite

Figure 54 shows the three scattering mechanisms along with the RGB composite done for the Mini-RF data of LRO by m-α decomposition for the Hermite-A crater which shows the dominance of volume scattering in the crater walls suggesting that the walls of the crater are of the rough surface as it was also seen in the other decomposition techniques namely m-δ decomposition and the m-χ decomposition of the Mini-SAR data and Mini-RF data as well. The crater base shows surface scattering in some of the regions and volume scattering is seen in the small peak in the crater and some of the regions of the crater walls are showing surface scattering, making double-bounce scattering visibility low in the region. The region outside the crater shows the dominance of surface scattering and the smooth surface in the crater walls also depicts surface scattering. The mean values of the volume scattering are 0.219 and for surface, scattering is 0.27 and for the double bounce is 0.028 which is very low in comparison to the volume and double-bounce.

5.5.4. Barnes Decomposition
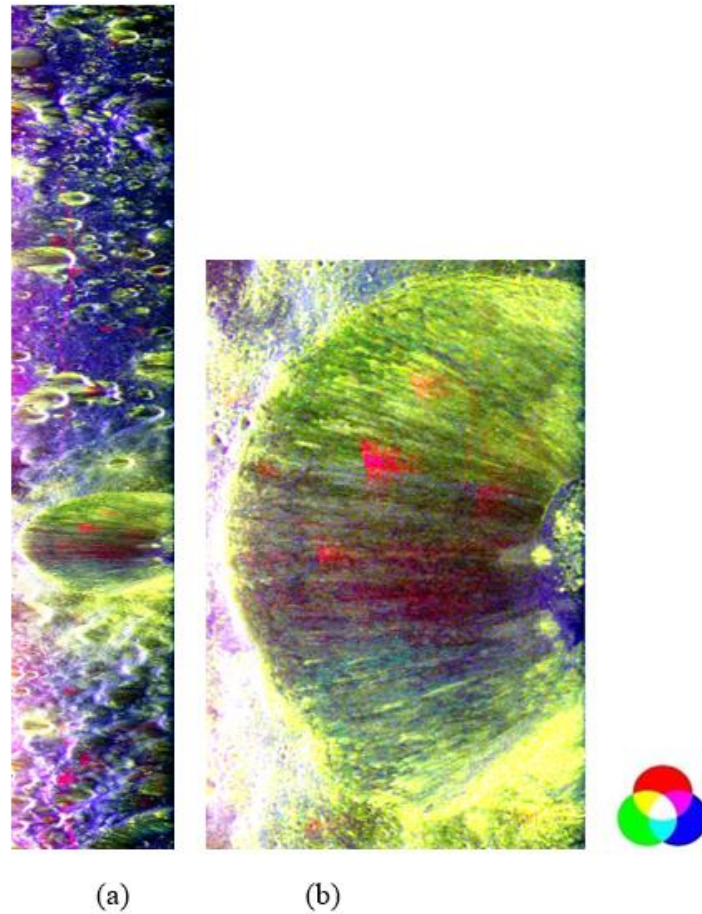
Figure 55 Barnes decomposition for Chandrayaan-2(DFSAR) (a) Full scene of the data covering Hermite-A crater (b) Zoomed view of Hermite-A crater

Figure 55 shows the Barnes decomposition applied on the scene covering Hermite-A crater for the DFSAR of Chandrayaan-2 data in L-band and on the right side is zoomed image of the crater. This decomposition shows the crater in a very good perspective in comparison to the S-band of Mini-SAR and Mini-RF of Chandryaan-1 and LRO respectively. The volume scattering is seen in dominance in the crater walls and the ejecta outside the crater rim. The double-bounce and surface scattering are seen in the middle of the left side of the crater wall. Some parts of the crater floor is showing surface scattering which was also seen in the S-band earlier depicting the crater floor is smooth. But the peaks situated inside the crater show volume scattering. The ejecta outside the crater rim can be easily identified in this scene as it is showing the extent of the ejecta to a good level. The craters which are seen in this scene can also be identified as it is showing volume scattering. The regolith or the lunar floor is showing surface scattering which is in blue depicting the surface to be smooth in the regions where the area of the crater is not present. Double bounce scattering is not seen but it is seen as a mixed scattering with the other scattering in some regions.

5.5.5.   H-A-Alpha Decomposition
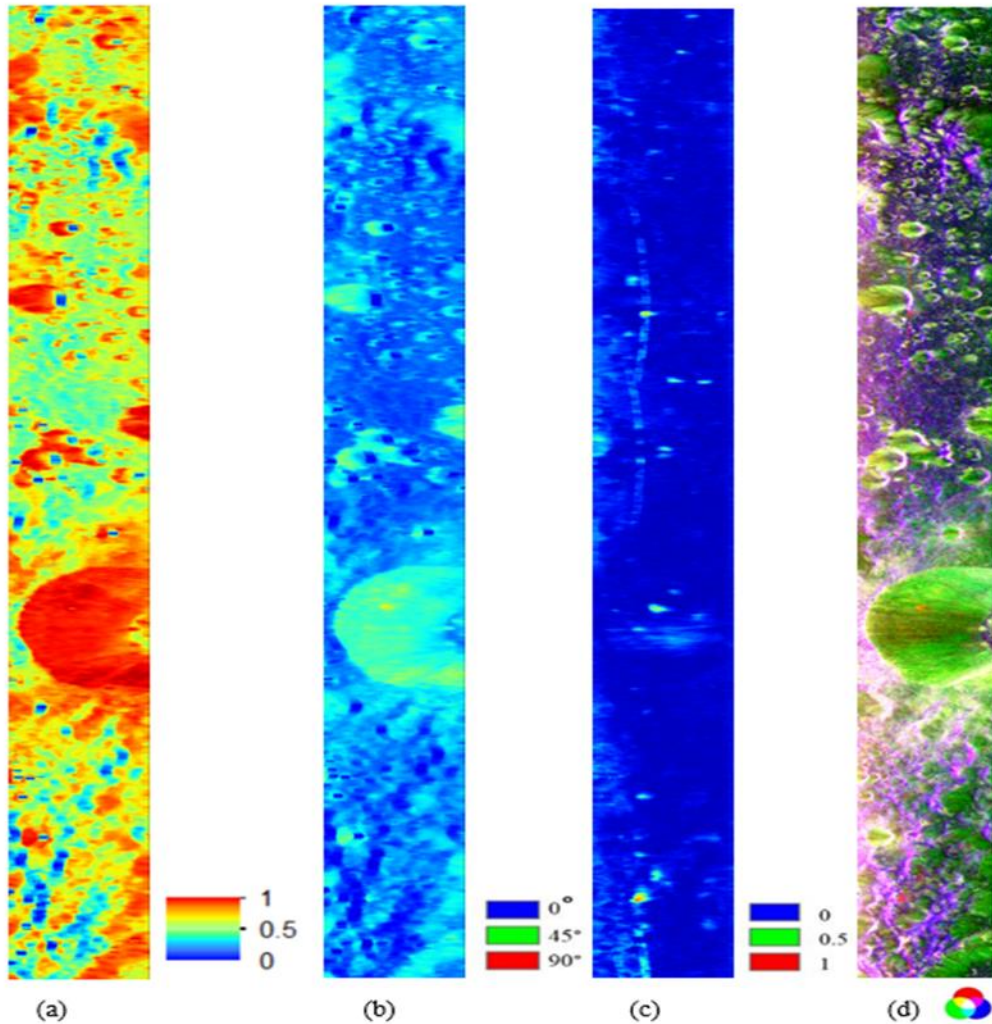
Figure 56 Parameters of eigenvalue and eigenvector based decomposition and polarimetric decomposition (a) Entropy, (b) Alpha angle, (c) Anisotropy (d) H-A-Alpha decomposition

The above figure 56 shows the Entropy, Alpha and Anisotropy derived from the H-A-alpha decomposition. To characterize the Hermite-A crater, these are the polarimetric parameters that are used. The RGB composite image of the H-A-Alpha decomposition has also been used to differentiate the scattering present in the scene and the crater. As it was seen in the Barnes decomposition of this scene the crater gives the dominance of the volume scattering present in the walls and the floor of the crater which is in green colour. This gives an interpretation of the rough surface present in the crater. A very small portion in the crater floor gives surface scattering and a mix of double bounce scattering in crater floor. This gives an idea about the crater floor which is smooth on the surface in comparison to the crater walls. The other small craters in the scene are also identified which gives volume scattering and the area which is in blue gives the interpretation about the surface to be smooth, which is surface scattering. The eigenvector-eigenvalue parameters Entropy and Alpha angle also go well with the results obtained from Barnes decomposition and H-A-Alpha decomposition models. The entropy values in the crater are higher and are around 1 in the crater region, which corresponds that it is because of the volume scattering present in the crater. The value of the alpha angle is around 45° in the crater region which again corresponds to volume scattering present in the

crater. This supports the results of the decomposition technique obtained in the form of the dominance of volumetric scattering. The value of Anisotropy in the major portion of the crater is zero which represents that the scattering is obtained from three pure targets. With these results, it can be withdrawn that the crater shows volume scattering in all the datasets and the decomposition models that were applied.

5.5.6. Analysis of Circular Polarization Ratio (CPR)
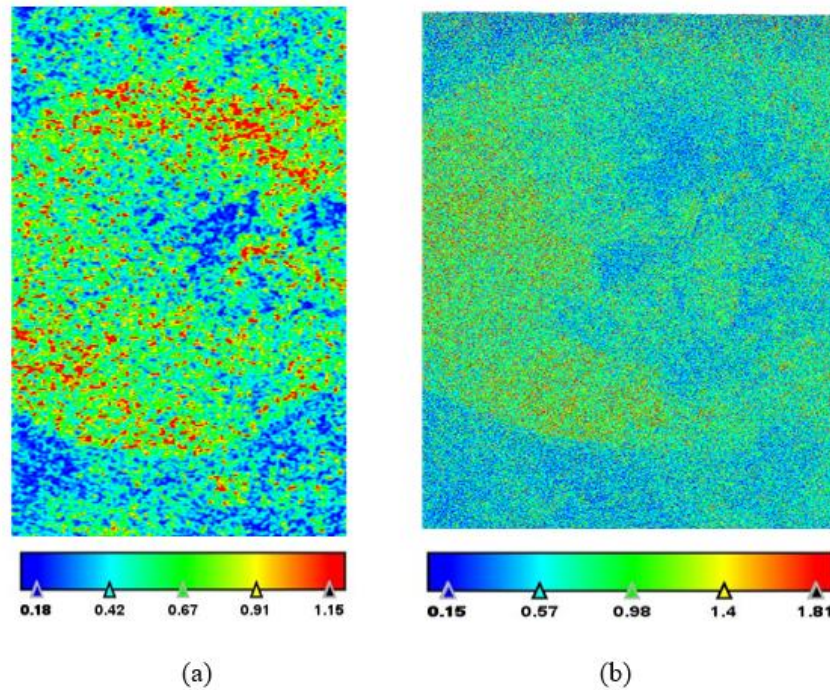
Figure 57 Value of CPR for Hermite-A crater (a) Chandrayaan-1(Mini-SAR) (b) LRO
(Mini-RF)

Figure 57(a), represents Chandrayaan-1's CPR values in the crater as determined by the Mini-SAR data. The high values of CPR, which is more than unity in the Hermite-A crater depict that the crater has some areas where possible water ice deposit locations can be found around. The values which are below 1 relate to the lunar regolith and the other materials. As a result of scattering by rough surfaces, high values of CPR can also occur. This may occur due to the double bounce scattering or the volume scattering. High CPR which is close to 1.15 particularly in the crater walls can also be seen on the left side and some areas on the floor of the crater. The areas outside of the crater show a low CPR value which can be caused due to the surface scattering. Figure 57(b), shows the value of CPR which is seen from the Mini-RF of LRO data of Hermite-A crater. Here, the value of CPR is much higher in comparison to the Mini-SAR. The values are near 1.81 on the left of the crater walls and some areas on the floor of the crater. The value around 1.4 is also seen in those areas which are also quite higher in these regions in comparison to the Mini-SAR data. Here, the lowest value is less than the Mini-SAR which is around 0.15 which depicts the region of surface scattering which is present on the crater floor and the areas outside the crater. It can be seen that the region where the value of the CPR is more than 1 those regions showed volume scattering in the decomposition.

5.5.7. Dielectric Characterization of Hermite-A crater

The further analysis of Hermite-A crater, Gaussian model has been used to retrieve the dielectric constant values of Hermite-A crater.
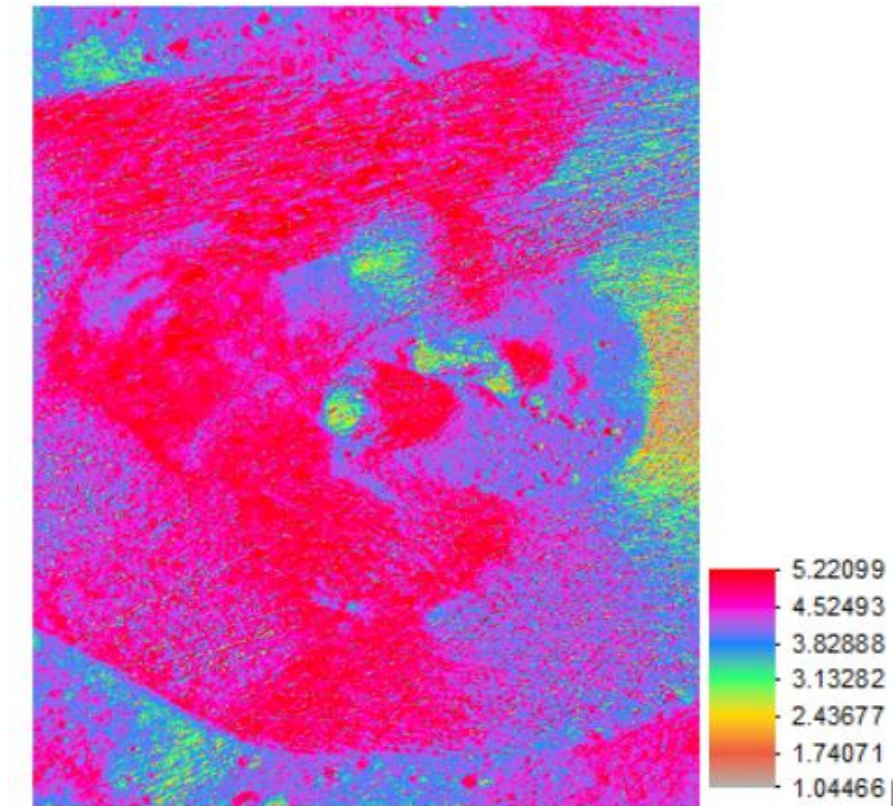
Figure 58 Dielectric Constant Values of Hermite-A crater from Chandrayaan-1 Mini-SAR data

Figure 58 shows the dielectric constant values from the Chandrayaan-1 Mini-SAR of the Hermite-A crater. The regions where the dielectric constant values are high are mainly on the crater walls. These regions, when compared with values of CPR and the decomposition techniques for volume scattering, showed that the crater walls have a high CPR value which is more than 1 and volume scattering was there in these regions. Some regions in the crater base showed high dielectric constant values too but, when compared with the decomposition techniques of the same region and the values of CPR which was low and they do not show volume scattering in these regions. So, it can be noted that these locations are not the possible locations of water ice deposits.
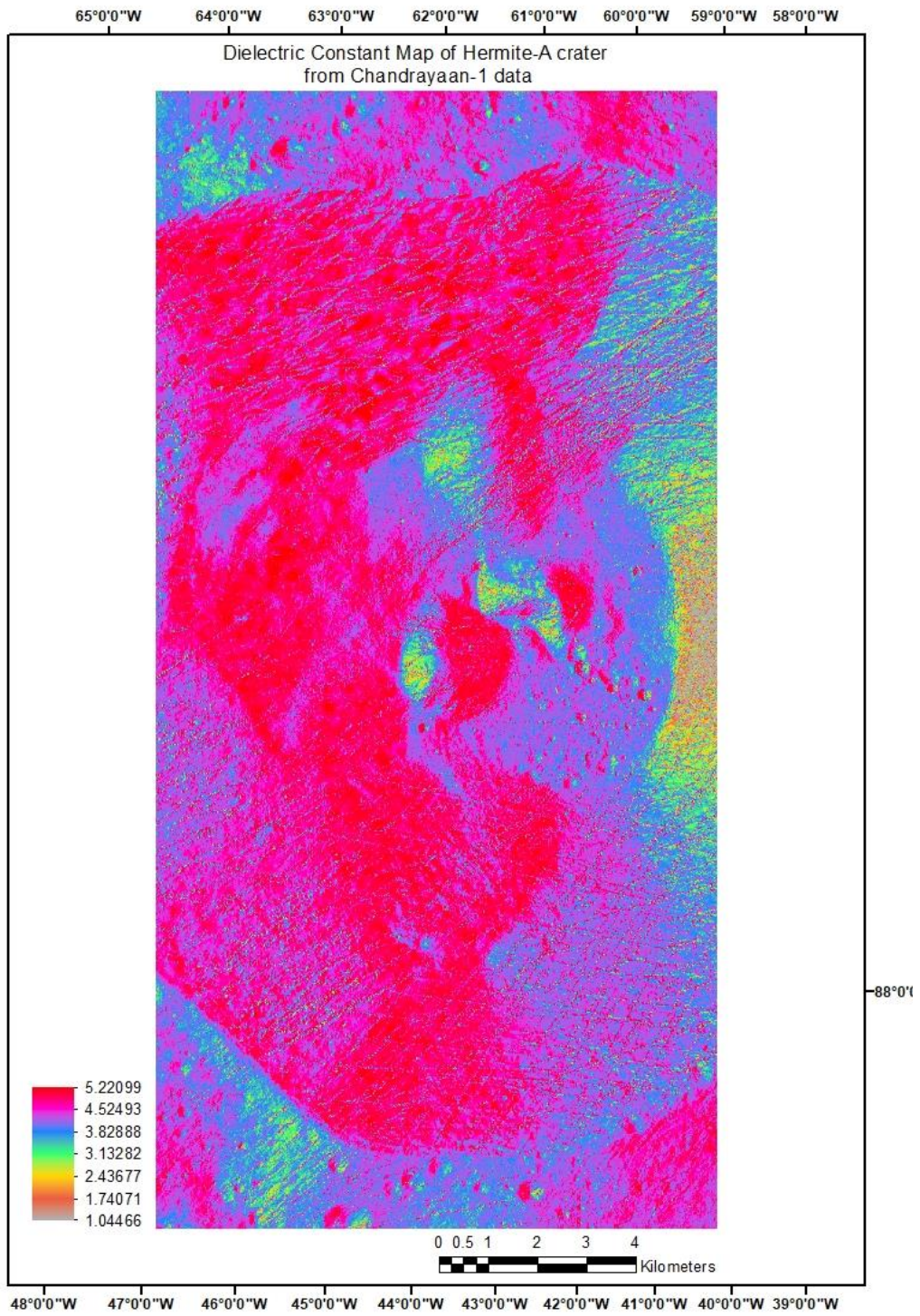
Figure 59 Dielectric Constant Map of Hermite-A crater from Chandrayaan-1 Mini-SAR data
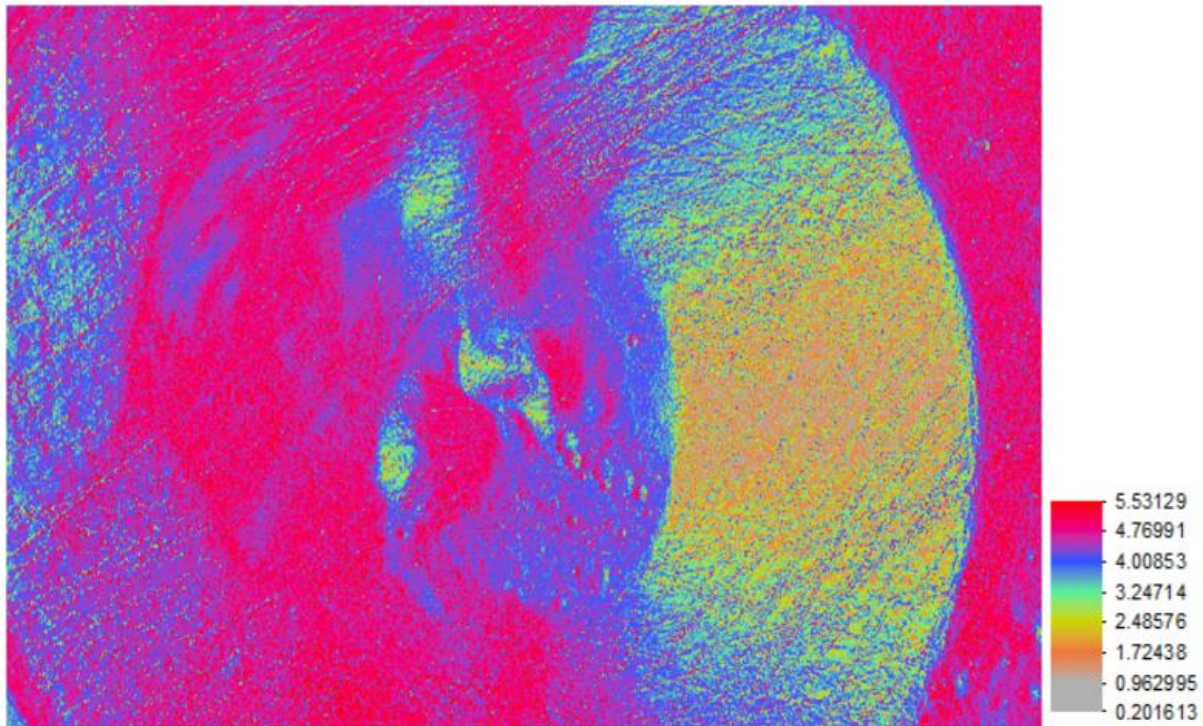
Figure 60 Dielectric Constant values of Hermite-A crater from LRO Mini-RF data

Figure 60, shows the dielectric constant values from the LRO Mini-RF data of the Hermite-A crater. The regions where the dielectric constant values are high are mainly on the crater walls which is similar to the values retrieved from the Chandrayaan-1 Mini-SAR data. These regions, when compared with values of CPR and the decomposition techniques for volume scattering, showed that the crater walls have a high CPR value which is more than 1 and volume scattering was there in these regions which are also in the case of Mini-SAR data. From this, it can be said that the crater walls can be possible locations of water ice. The range of dielectric constant derived from the Mini-SAR of Chandrayaan-1 and Mini-RF of LRO is similar which is 1.04466 to 5.22099 and 0.2016 to 5.53129.
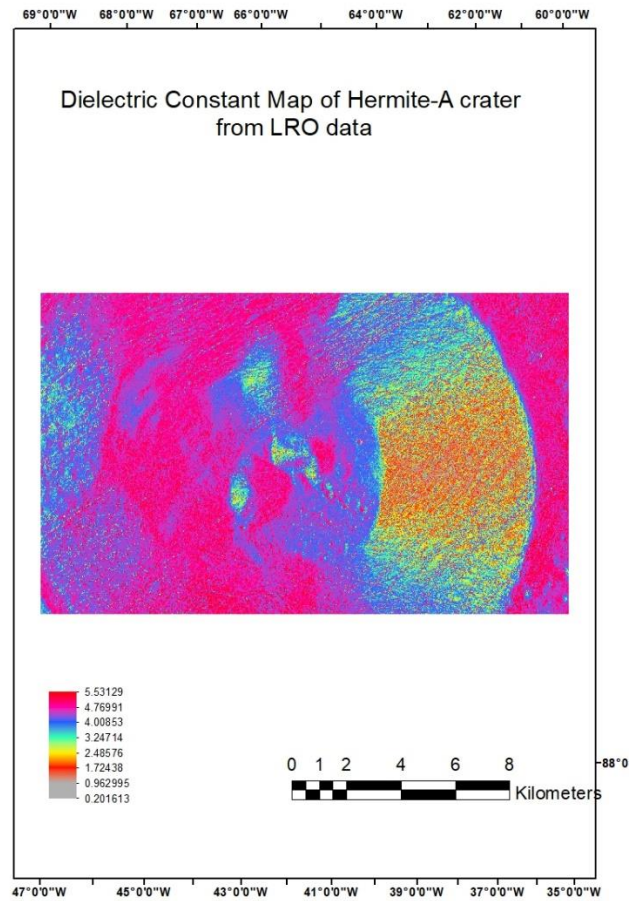
Figure 61 Dielectric Constant Map of Hermite-A crater from LRO Mini-RF data
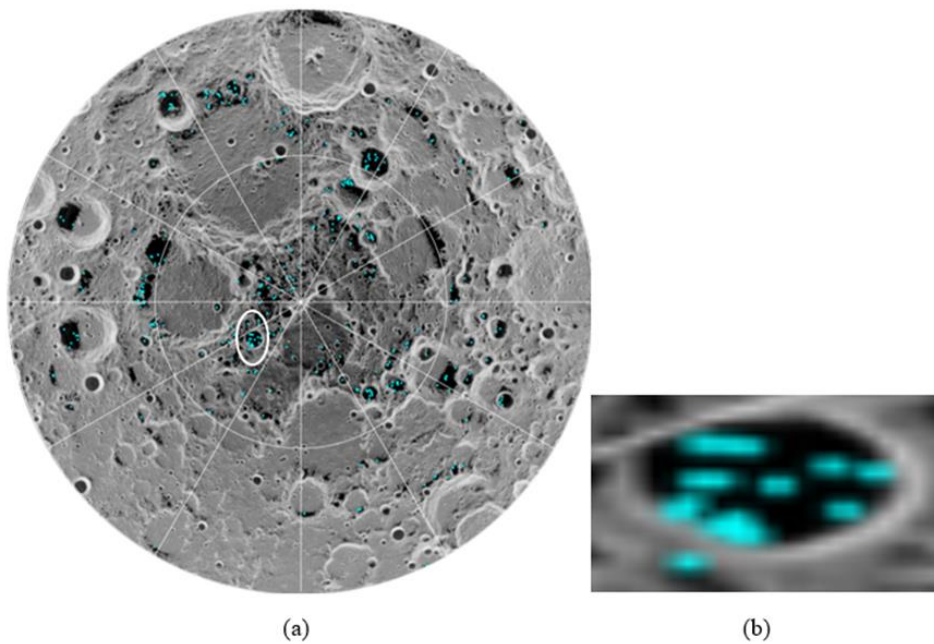
Figure 62 Clusters of surface ice at the Lunar North Pole, detected by NASA's Moon Mineralogy Mapper instrument of ISRO's Chandrayaan-1 mission (Credit: NASA). (a) The white circle is the Hermite-A crater (b) Zoomed view of Hermite-A crater

A recent study shows the distribution of ice clusters present in the lunar North pole (Li et al., 2018). Various studies in past that have been carried out state the importance of CPR for water ice detection on lunar poles (Nozette et al., 2001; P. D. Spudis et al., 2013; Thomson et al., 2012). It may be possible for regions where CPR values are greater than unity to be caused by EMR interacting with the boundary of water ice and hence may be possible locations of water ice deposits(Eke et al., 2014). It can also be concluded that values of high CPR are may be possible because of the lunar boulders or the rough surface present in the lunar regolith (Fa & Cai, 2013). It is a bit difficult to conclude that the detection of the water-ice present in the regolith is because of the high values of CPR. As high volume scattering is also present in the crater walls and it is clear in all the decomposition techniques. As above mentioned about the recent study which was carried by Li et al., 2018 showed the distribution of ice clusters in the region from Moon Mineralogy Mapper (M3) aboard Chandrayaan-1 (Fig.62 a) which shows the Hermite-A crater in the white encircled region and it can be seen that the ice clusters are present in crater walls. So, it can be concluded from the results that the high volume scattering and high CPR and high values of dielectric constant are not because of boulders or rocks but it is because of the presence of water-ice present in the regolith of the crater.

5.6.   Characterization of the Rimae Sulpicius Gallus

The Rimae Sulpicius Gallus is the lunar rille that contains pyroclastic deposits in its surrounding area. The characterization of this area is done by the m-χ decomposition technique for the hybrid-pol data of LRO Mini-RF and values of CPR.
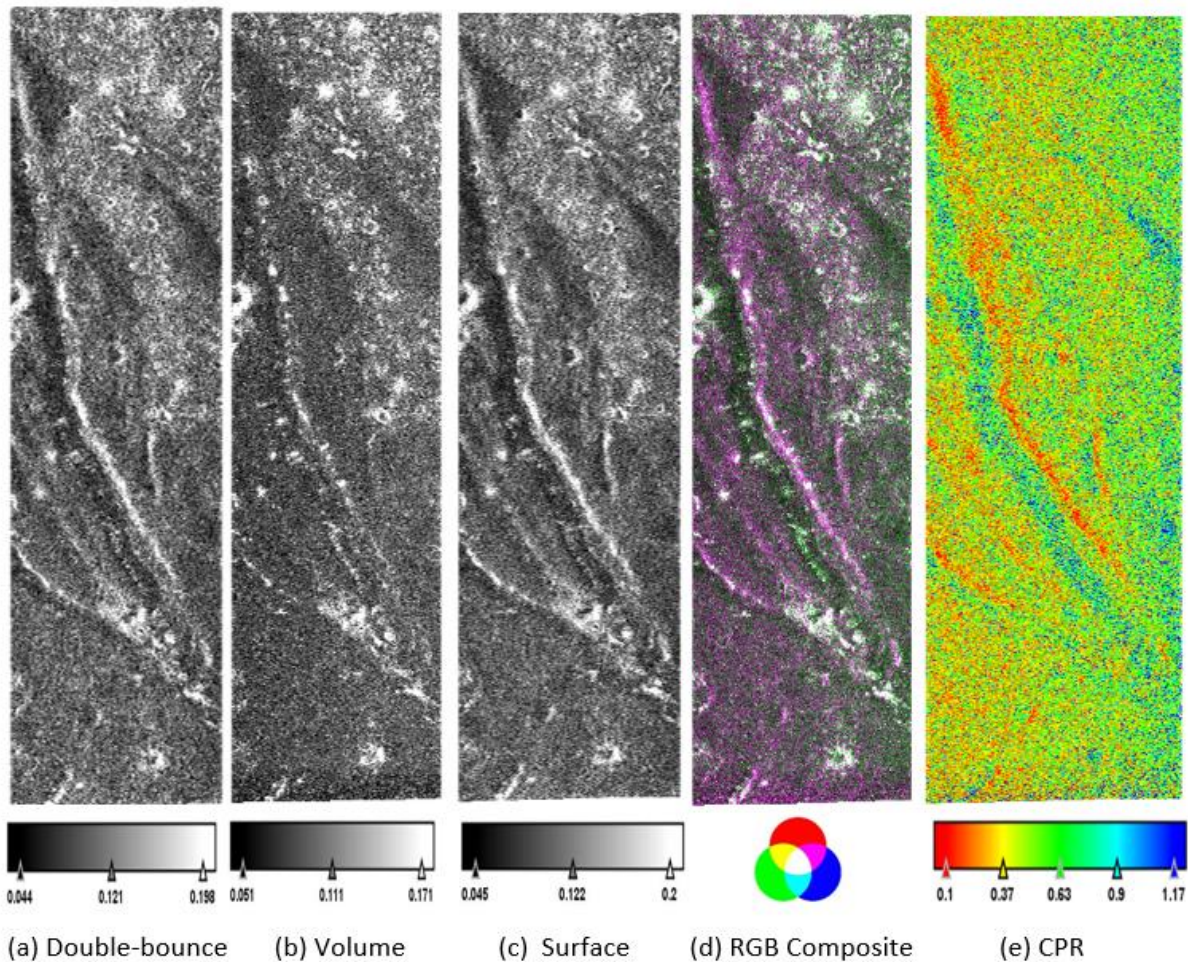
Figure 63 m- χ decomposition of LRO (Mini-RF) (a) Double-bounce scattering, (b) Volume scattering,(c) Surface scattering and (d) RGB colour composite (e) CPR values

Fig 63 shows the RGB composite of the m-chi decomposition in which the area where the rille i.e., the Rimae Sulpicius Gallus is seen, shows the dominance of double bounce scattering in the surrounding region including some part which shows the volume scattering. In this, it can be seen that the mean values of all the scattering mechanisms are quite similar which is 0.12 for double-bounce scattering, 0.12 for surface scattering, and 0.11 for volume scattering.

For any surface, if the CPR value is greater than one indicates that due to the presence of diffuse scatterers or volume scattering shows the same sense polarization. The area which showed the volume scattering in the decomposition has a higher value of CPR which is around 1.17 in these regions (figure 63 e). The pyroclastic deposits in the region show the presence of high volume scattering along with the double-bounce scattering.

6. CONCLUSIONS AND RECOMMENDATIONS

This study shows an attempt to identify and characterize the region of the lunar poles and the PSR region of the lunar surface which also includes the lunar rille present in the Mare Serenitatis region. The main objective of this work was to find the possible locations of water ice present by polarimetric decompositions techniques of compact polarimetry and fully polarimetric data in combination with the polarimetric parameters and the dielectric constant values. To achieve this objective the m-δ, m-χ and m-α decomposition have been used for the Hybrid polarimetric data and Barnes decomposition and eigenvector and eigenvalues based H-A-α decomposition model have been used for fully polarimetric data. The scattering patterns that were obtained from these decompositions were supported by Entropy, Alpha angle and Anisotropy parameters. The dielectric constant values also supported these patterns in Hermite-A crater. This study gives an idea about the craters in the lunar poles which gives an interpretation of the scattering in these regions. The use of CPR value gives the idea about the regions in the crater where there is a rough surface or smooth and an initial interpretation of the region about the possible locations of water ice deposits. As it was seen in the craters namely Shackleton, Erlanger and Hermite-A crater that the values of CPR were more than unity in the craters which can be a reason for the water-ice deposits as the values were high. The m-chi decomposition technique for the Hybrid polarimetric data was better in comparison to m-alpha and m-delta as in the m-chi decomposition technique the interpretation of the scattering mechanisms was good. The value of CPR in the Shackleton crater was high which was around 1.99 in some regions and these regions also showed high volume scattering in all the decomposition techniques that were applied. Erlanger crater also showed a high CPR value which was around 1.13 and the crater walls and the crater floor showed high volume scattering in these regions in all the decomposition techniques that were applied on the Hybrid polarimetry data. Hermite-A crater also showed very high volume scattering in the walls of the crater and which was obtained in all the decompositions applied to the scenes. For both the Mini-SAR and Mini-RF datasets, the CPR value was also greater than unity in regions with considerable volume scattering. According to Mini-SAR and Mini-RF data, the CPR value for Hermite-A was approximately 1.15.In the areas where volume scattering was high and CPR values were high, the dielectric constant of the crater was also high.The region was also compared with the surface ice distribution map done in 2018 by Li et al., it is found out that the reason for getting high volume scattering and high CPR and high values of dielectric constant is because of the water-ice present in the PSR of the lunar north polar crater. The bands of different SAR missions which were included in the study were S-band for Mini-SAR and Mini-RF and L-band for DFSAR. The L-band gave a good visual interpretation of the scenes for the Erlanger, Hermite-A, Slater and Cabeus. The PSR regions were also identified in the scenes from the Lunar Reconnaissance Orbiter Camera (LROC) which is available from NASA/GSFC. The Barnes decomposition technique which is based on wave dichotomy and H-A-alpha decomposition technique for the fully polarimetric data of L-band DFSAR characterizes the crater in a much detailed manner in comparison to the S-band. These decomposition techniques also characterize the scattering of the Slater, Erlanger, Cabeus and Hermite-A crater . The polarimetric parameters like Entropy, Alpha angle and Anisotropy in L-band DFSAR also gave a constructive result in identifying the scattering behaviour in these craters. All the scenes which covered the craters namely Erlanger, Cabeus and Hermite-A showed the entropy value more than 1 and the alpha angle around 45 and the anisotropy around 0 showed volume scattering which was also scened in the other decomposition techniques. The two PSR regions of the Cabeus crater showed low entropy and low alpha angle as when compared to the Barnes decomposition technique and H-A-alpha decomposition technique these regions also were not showing volume scattering as some parts in the region showed a mix of surface and double-bounce scattering. From, this it can be concluded that the craters which showed high volume scattering and high CPR and required values of polarimetric parameters can be a probable location of water-ice deposits. This study also included the characterization of Rimae Sulpicius Gallus which is a lunar rille.

The identification of this lunar rille was based on the literature of the previous studies done in this region. As the previous study used radar data to characterize and obtain the values of CPR. This study gave an attempt to characterize the region with polarimetric SAR data of LRO Mini-RF of the S-band. The rille showed high volume scattering in the region and high CPR values which were around 1.17 in the regions where volume scattering was dominant. For future studies, this study recommends that a dielectric model can be used for multi-frequency datasets for identifying the regions of water-ice deposits. The craters can be identified for surface characterization and identification of lunar volatiles, surface and subsurface features present in the lunar regolith, which can be an advancement for the future exploration of these areas.

LIST OF REFERENCES

Arnold, J. R. (1979). Ice in the lunar polar regions. *Journal of Geophysical Research*, *84*(B10), 5659. https://doi.org/10.1029/JB084iB10p05659

Bhandari, N., & Srivastava, N. (2014). Active moon: evidences from Chandrayaan-1 and the proposed Indian missions. In *Geoscience Letters* (Vol. 1, Issue 1, p. 11). SpringerOpen. https://doi.org/10.1186/s40562-014-0011-y

Bhattacharya, A., Porwal, A., Dhingra, S., De, S., & Venkataraman, G. (2015). Remote estimation of dielectric permittivity of lunar surface regolith using compact polarimetric synthetic aperture radar data. *Advances in Space Research*, *56*(11), 2439–2448. https://doi.org/10.1016/j.asr.2015.10.007

Bhavya, K. B. (2013). *Polarimetric Modeling of Lunar Surface for Scattering Information Retreival using Mini-SAR data of Chandrayaan-1* [University of Twente, Enschede, The Netherlands]. http://essay.utwente.nl/84659/1/kausika.pdf

Bhiravarasu, Sriram S., Chakraborty, T., Putrevu, D., Pandey, D. K., Das, A. K., Ramanujam, V. M., Mehra, R., Parasher, P., Agrawal, K. M., Gupta, S., Seth, G. S., Shukla, A., Pandya, N. Y., Trivedi, S., Misra, A., Jyoti, R., & Kumar, R. (2021). *Chandrayaan-2 Dual-Frequency SAR (DFSAR): Performance Characterization and Initial Results*. http://arxiv.org/abs/2104.14259

Bhiravarasu, Sriram Saran, Chakraborty, T., Heggy, E., & Kumar, R. (2020). *CHARACTERIZING THE SCATTERING PROPERTIES OF THE MOON WITH THE LRO MINI-RF AND CHANDRAYAAN-2 DFSAR RADARS*. *February*, 1–3.

Boerner, W. (2004). Basics of Radar Polarimetry Introduction : A Review of Polarimetry. *Sensing And Imaging*, *October*, 21–22.

Calla, O. P. N., Mathur, S., & Gadri, K. L. (2016). Quantification of Water Ice in the Hermite-A Crater of the Lunar North Pole. *IEEE Geoscience and Remote Sensing Letters*, *13*(7), 926–930. https://doi.org/10.1109/LGRS.2016.2554282

Calla OPN, Mathur Shubhra, J. M. (2014). Analysis of Dielectric constant & density of Apollo 17 samples. *International Journal of Remote Sensing & Geoscience(IJRSG)*, *3*(5, Sept.), 18–22.

Calla, P. N., Mathur, S., & Jangid, M. (2014). Study of equatorial regions of Moon with the help of backscattering coefficient obtained from LRO data. *Journal of Earth System Science*, *123*(2), 433–443. https://doi.org/doi.org/10.1007/s12040-014-0407-2

Campbell, B. A. (2002). *Radar remote sensing of planetary surfaces*. Cambridge University Press.

Carter, L., Goswami, J., Heggy, E., Kirk, R., Misra, T., Nozette, S., Robinson, M., Thompson, T., Thomson, B., & Ustinov, E. (2009). The MiniSAR Imaging Radar on then Chandrayaan - 1 on the Moon. *Lunar and Planetary Science Conference*, *40*(1098), 7–8.

Carter, L. M., Campbell, B. A., Hawke, B. R., Campbell, D. B., & Nolan, M. C. (2009). Radar remote sensing of pyroclastic deposits in the southern Mare Serenitatis and Mare Vaporum regions of the Moon. *J. Geophys. Res*, *114*, 11004. https://doi.org/10.1029/2009JE003406

Chin, G., Brylow, S., Foote, M., Garvin, J., Kasper, J., Keller, J., Litvak, M., Mitrofanov, I., Paige, D., Raney, K., Robinson, M., Sanin, A., Smith, D., Spence, H., Spudis, P., Stern, S. A., & Zuber, M. (2007). Lunar reconnaissance orbiter overview: The instrument suite and mission. *Space Science Reviews*, *129*(4), 391–419. https://doi.org/10.1007/s11214-007-9153-y

Colaprete, A., Schultz, P., Heldmann, J., Wooden, D., Shirley, M., Ennico, K., Hermalyn, B., Marshall, W., Ricco, A., Elphic, R. C., Goldstein, D., Summy, D., Bart, G. D., Asphaug, E., Korycansky, D., Landis, D., & Sollitt, L. (2010). Detection of water in the LCROSS ejecta plume. *Science*, *330*(6003), 463–468. https://doi.org/10.1126/science.1186986

Crawford, I. A. (2015). Lunar resources: A review. *Progress in Physical Geography*, *39*(2), 137–167. https://doi.org/10.1177/0309133314567585

E.M., S., M.S., R., & E.M., E. (1994). The South Pole Region of the MOON as seen by Clementine. *American Association for the Advancement of Science*, *266*(5192), 1851–1854. https://doi.org/DOI: 10.1126/science.266.5192.1851

Earth and Moon Once Shared a Magnetic Shield | NASA. (n.d.). Retrieved April 5, 2021, from https://www.nasa.gov/feature/earth-and-moon-once-shared-a-magnetic-shield-protecting-their-atmospheres

Eke, V. R., Bartram, S. A., Lane, D. A., Smith, D., & Teodoro, L. F. A. (2014). Lunar polar craters – Icy, rough or just sloping? *Icarus*, *241*, 66–78.

https://doi.org/https://doi.org/10.1016/j.icarus.2014.06.021

Fa, W., & Cai, Y. (2013). Circular polarization ratio characteristics of impact craters from Mini-RF observations and implications for ice detection at the polar regions of the Moon. *Journal of Geophysical Research E: Planets*, *118*(8), 1582–1608. https://doi.org/10.1002/jgre.20110

Fa, W., Wieczorek, M. A., & Heggy, E. (2011). Modeling polarimetric radar scattering from the lunar surface: Study on the effect of physical properties of the regolith layer. *Journal of Geophysical Research E: Planets*, *116*(3), 1–33. https://doi.org/10.1029/2010JE003649

Feldman, W. C., Maurice, S., Lawrence, D. J., Little, R. C., Lawson, S. L., Gasnault, O., Wiens, R. C., Barraclough, B. L., Elphic, R. C., Prettyman, T. H., Steinberg, J. T., & Binder, A. B. (2001). Evidence for water ice near the lunar poles. *Journal of Geophysical Research E: Planets*, *106*(E10), 23231–23251. https://doi.org/10.1029/2000JE001444

Flahaut, J., Carpenter, J., Williams, J. P., Anand, M., Crawford, I. A., van Westrenen, W., Füri, E., Xiao, L., & Zhao, S. (2020). Regions of interest (ROI) for future exploration missions to the lunar South Pole. *Planetary and Space Science*, *180*, 104750. https://doi.org/10.1016/j.pss.2019.104750

Gaddis, L. R., Pieters, C. M., & Ray Hawke, B. (1985). Remote sensing of lunar pyroclastic mantling deposits. *Icarus*, *61*(3), 461–489. https://doi.org/https://doi.org/10.1016/0019-1035(85)90136-8

Gaddis, L. R., Staid, M. I., Tyburczy, J. A., Hawke, B. R., & Petro, N. E. (2003). Compositional analyses of lunar pyroclastic deposits. *Icarus*, *161*(2), 262–280. https://doi.org/10.1016/S0019-1035(02)00036-2

Harvey, B., Smid, H. H. F., & Pirard, T. (2010). Emerging Space Powers. In *Emerging Space Powers*. https://doi.org/10.1007/978-1-4419-0874-2

Hayne, P. O., Aharonson, O., & Schörghofer, N. (2020). *Micro Cold Traps on the Moon*. https://doi.org/10.1038/s41550-020-1198-9

HEIKEN, G. H., VANIMAN, D. T., & FRENCH, B. M. (1991). Lunar Sourcebook. In *Cambridge University Press*.

Hurwitz, D. M., Head, J. W., & Hiesinger, H. (2013). Lunar sinuous rilles: Distribution, characteristics, and implications for their origin. *Planetary and Space Science*, *79–80*(1), 1–38. https://doi.org/10.1016/j.pss.2012.10.019

In-Depth | Earth's Moon – NASA Solar System Exploration. (n.d.). Retrieved April 5, 2021, from https://solarsystem.nasa.gov/moons/earths-moon/in-depth/

Jozwiak, L. M., Head, J. W., Zuber, M. T., Smith, D. E., & Neumann, G. A. (2012). Lunar floor-fractured craters: Classification, distribution, origin and implications for magmatism and shallow crustal structure. *Journal of Geophysical Research: Planets*, *117*(E11). https://doi.org/https://doi.org/10.1029/2012JE004134

Kim, K. J., Dohm, J. M., Williams, J. P., Ruiz, J., Hare, T. M., Hasebe, N., Karouji, Y., Kobayashi, S., Hareyama, M., Shibamura, E., Kobayashi, M., D'Uston, C., Gasnault, O., Forni, O., & Maurice, S. (2012). The South Pole-Aitken basin region, Moon: GIS-based geologic investigation using Kaguya elemental information. *Advances in Space Research*, *50*(12), 1629–1637. https://doi.org/10.1016/j.asr.2012.06.019

Koeberl, C. (2004). *Remote sensing studies of impact craters : how to be sure ? 336*, 959–961. https://doi.org/10.1016/j.crte.2004.05.001

Kozlova, E. A., & Lazarev, E. N. (2010). Crater Cabeus as possible cold trap for volatiles near south pole of the moon. *41st Lunar and Planetary Science Conference*, 2–3.

Kumar, P. A., & Kumar, S. (2014). Estimation of optical maturity parameter for lunar soil characterization using Moon Mineralogy Mapper (M3). *Advances in Space Research*, *53*(12), 1694–1719. https://doi.org/10.1016/j.asr.2014.01.009

Lawrence, S. ., & Hawke, B. . (2008). LUNAR PYROCLASTIC DEPOSITS: AN ACCESSIBLE AND QUANTIFIABLE LUNAR RESOURCE. *39th Lunar and Planetary Science Conference*.

Li, S., Lucey, P. G., Milliken, R. E., Hayne, P. O., Fisher, E., Williams, J. P., Hurley, D. M., & Elphic, R. C. (2018). Direct evidence of surface exposed water ice in the lunar polar regions. *Proceedings of the National Academy of Sciences of the United States of America*, *115*(36), 8907–8912. https://doi.org/10.1073/pnas.1802345115

Liu, N., Fa, W., & Jin, Y. (2018). No Water–Ice Invertable in PSR of Hermite-A Crater Based on Mini-RF Data and Two-Layers Model. *IEEE Geoscience and Remote Sensing Letters*, *15*(10), 1485–1489. https://doi.org/10.1109/LGRS.2018.2852139

Lucey, P. G. (2004). Mineral maps of the Moon. *Geophysical Research Letters*, *31*(8). https://doi.org/10.1029/2003GL019406

Lucey, P. G., Taylor, G. J., Hawke, B. R., & Spudis, P. D. (1998). FeO and TiO$_2$ concentrations in the

South Pole-Aitken basin: Implications for mantle composition and basin formation. *Journal of Geophysical Research: Planets*, *103*(E2), 3701–3708. https://doi.org/10.1029/97JE03146

Meng, Z., Chen, S., Osei, E. M., Wang, Z., & Cui, T. (2010). Research on water ice content in Cabeus crater using the data from the microwave radiometer onboard Chang'e-1 satellite. *Science China: Physics, Mechanics and Astronomy*, *53*(12), 2172–2178. https://doi.org/10.1007/s11433-010-4159-y

Mohan, S., Das, A., & Chakraborty, M. (2011). Studies of polarimetric properties of lunar surface using Mini-SAR data. *Current Science*, *101*(2), 159–164.

Moriarty, D. P., & Pieters, C. M. (2018). The Character of South Pole-Aitken Basin: Patterns of Surface and Subsurface Composition. *Journal of Geophysical Research: Planets*, *123*(3), 729–747. https://doi.org/10.1002/2017JE005364

NASA - South Pole -- Aitken Basin. (n.d.). Retrieved March 9, 2021, from https://www.nasa.gov/mission_pages/LRO/multimedia/lroimages/lola-20100409-aitken.html

Nozette, S., Spudis, P. D., Robinson, M. S., Bussey, D. B. J., Lichtenberg, C., & Bonner, R. (2001). Integration of lunar polar remote-sensing data sets: Evidence for ice at the lunar south pole. *Journal of Geophysical Research E: Planets*, *106*(E10), 23253–23266. https://doi.org/10.1029/2000JE001417

Patel, V., Pabari, J., & Patel, J. (2014). Revisiting Lunar Water Ice Content Retrieval Using Lunar Remote Sensing Data. *IOSR Journal of Electrical and Electronics Engineering*, *9*(3), 14–18. https://doi.org/10.9790/1676-09331418

Patterson, G. W., Bhiravarasu, S. S., Carter, L. M., S Cahill, J. T., Chakraborty, T., Das, A., Heggy, E., Kumar, R., Morgan, G. A., Neish, C. D., Nypaver, C. A., Palmer, E. M., Pandey, D. K., Plescia, J. B., Putrevu, D., Stickle, A. M., Taylor, P. A., Thomson, B. J., Mini-RF, the, & teams, D. (2020). CHARACTERIZING THE SCATTERING PROPERTIES OF THE MOON WITH THE LRO MINI-RF AND CHANDRAYAAN-2 DFSAR RADARS. In *LPI* (Issue 2326). https://ui.adsabs.harvard.edu/abs/2020LPI....51.2507P/abstract

Petro, N. E., & Pieters, C. M. (2004). Surviving the heavy bombardment: Ancient material at the surface of South Pole-Aitken basin. *Journal of Geophysical Research E: Planets*, *109*(6), 1–13. https://doi.org/10.1029/2003JE002182

Putrevu, D., Das, A., Vachhani, J. G., Trivedi, S., & Misra, T. (2015). *Chandrayaan-2 dual-frequency SAR: Further investigation into lunar water and regolith*. https://doi.org/10.1016/j.asr.2015.10.029

Putrevu, D., Trivedi, S., Das, A., & Pandey, D. (2020a). *L- and S-band Polarimetric Synthetic Aperture Radar on Chandrayaan-2 mission. January*.

Putrevu, D., Trivedi, S., Das, A., & Pandey, D. (2020b). *L- and S-band Polarimetric Synthetic Aperture Radar on Chandrayaan-2 mission. 118*(January).

Raney Keith, R., Cahill, J. T. S., Patterson Wesley, G., & Bussey, D. B. J. (2012). The m-chi decomposition of hybrid dual-polarimetric radar data with application to lunar craters. *Journal of Geophysical Research E: Planets*, *117*(5). https://doi.org/10.1029/2011JE003986

Rilles and Rilles: Sinuous, Straight, and Arcuate | Lunar Reconnaissance Orbiter Camera. (n.d.). Retrieved September 22, 2021, from http://lroc.sese.asu.edu/posts/1147

Shahsavarhaghighi, S., Sahebi, M. R., Valdanzoej, M. J., & Haddadi, G. A. (2013). A Comparison of IEM and SPM Model for Oil Spill Detection Using Inversion Technique and Radar Data. *Journal of the Indian Society of Remote Sensing*, *41*(2), 425–431. https://doi.org/10.1007/s12524-012-0217-4

Shearer, C. K., & Papike, J. J. (1993). Basaltic magmatism on the Moon: A perspective from volcanic picritic glass beads. *Geochimica et Cosmochimica Acta*, *57*(19), 4785–4812. https://doi.org/https://doi.org/10.1016/0016-7037(93)90200-G

Shukla, S. (2019). *Spectroscopy and Bistatic Miniature Radar Lunar Regolith Characterization for Solar Wind Implanted Helium-3 using M3 Spectroscopy and Bistatic Miniature Radar. March*, 1–83. https://library.itc.utwente.nl/papers_2019/msc/gfm/shukla.pdf

Shukla, S., Kumar, S., & Tolpekin, V. A. (2019). Petrophysical Insights Into Lunar Mafic Extrusive Basalts Over Reiner Gamma Formation. *IEEE Journal of Selected Topics in Applied Earth Observations and Remote Sensing*, 1–17. https://doi.org/10.1109/jstars.2019.2909352

Spudis, P. D., Bussey, D. B. J., Baloga, S. M., Cahill, J. T. S., Glaze, L. S., Patterson, G. W., Raney, R. K., Thompson, T. W., Thomson, B. J., & Ustinov, E. A. (2013). Evidence for water ice on the Moon: Results for anomalous polar craters from the LRO Mini-RF imaging radar. *Journal of Geophysical Research: Planets*, *118*(10), 2016–2029. https://doi.org/10.1002/jgre.20156

Spudis, Paul D., Bussey, B., Plescia, J., Joset, J. L., & Beauvivre, S. (2008). Geology of Shackleton Crater and the south pole of the Moon. *Geophysical Research Letters*, *35*(14). https://doi.org/10.1029/2008GL034468

Sridharan, R., Ahmed, S. M., Pratim Das, T., Sreelatha, P., Pradeepkumar, P., Naik, N., & Supriya, G. (2010). "Direct" evidence for water (H2O) in the sunlit lunar ambience from CHACE on MIP of Chandrayaan I. *Planetary and Space Science*, *58*(6), 947–950. https://doi.org/10.1016/j.pss.2010.02.013

The Apollo Missions | NASA. (n.d.). Retrieved September 17, 2021, from https://www.nasa.gov/mission_pages/apollo/missions/index.html

Thomson, B. J., Bussey, D. B. J., Neish, C. D., Cahill, J. T. S., Heggy, E., Kirk, R. L., Patterson, G. W., Raney, R. K., Spudis, P. D., Thompson, T. W., & Ustinov, E. A. (2012). An upper limit for ice in Shackleton crater as revealed by LRO Mini-RF orbital radar. *Geophysical Research Letters*, *39*(14), 2–5. https://doi.org/10.1029/2012GL052119

Thomson, B. J., Bussey, D. B. J., S Cahill, J. T., Neish, C., Patterson, G. W., & Spudis, P. D. (2011). The Interior of Shackleton crater as revealed by Mini-Rf orbital radar. *Science*, 10–11.

Tomar, K. S. (2015). *Hybrid Polarimetric Decomposition for Aboveground Biomass Estimation Using Semi- Empirical Modelling*. 70.

Vashishtha, A., & Kumar, S. (2020). Characterization of geomorphological features of lunar surface using Chandrayaan-1 Mini-SAR and LRO Mini-RF data. *Quaternary International*, *August*. https://doi.org/10.1016/j.quaint.2020.08.018

Vondrak, R., Keller, J., Chin, G., & Garvin, J. (2010). Lunar reconnaissance orbiter (LRO): Observations for lunar exploration and science. *Space Science Reviews*, *150*(1–4), 7–22. https://doi.org/10.1007/s11214-010-9631-5

Woodhouse, I. H. (2006). Introduction to microwave remote sensing LK - https://ut.on.worldcat.org/oclc/60796272. In *TA - TT -*. Taylor & Francis. http://bvbr.bib-bvb.de:8991/F?func=service&doc_library=BVB01&doc_number=016333240&line_number=0001&func_code=DB_RECORDS&service_type=MEDIA

Yamaguchi, Y., Moriyama, T., Ishido, M., & Yamada, H. (2005). Four-component scattering model for polarimetric SAR image decomposition. *IEEE Transactions on Geoscience and Remote Sensing*, *43*(8), 1699–1706. https://doi.org/10.1109/TGRS.2005.852084

Yingst, R. A., & Head, J. W. (1999). Geology of mare deposits in South Pole-Aitken basin as seen by Clementine UV/VIS data. *Journal of Geophysical Research: Planets*, *104*(E8), 18957–18979. https://doi.org/10.1029/1999JE900016

Zou, B., Zhang, Y., Cao, N., & Minh, N. P. (2015). A four-component decomposition model for PolSAR data using asymmetric scattering component. *IEEE Journal of Selected Topics in Applied Earth Observations and Remote Sensing*, *8*(3), 1051–1061. https://doi.org/10.1109/JSTARS.2014.2380151

Zuber, M. T., Head, J. W., Smith, D. E., Neumann, G. A., Mazarico, E., Torrence, M. H., Aharonson, O., Tye, A. R., Fassett, C. I., Rosenburg, M. A., & Melosh, H. J. (2012). Constraints on the volatile distribution within Shackleton crater at the lunar south pole. *Nature*, *486*(7403), 378–381. https://doi.org/10.1038/nature11216

APPENDIX-1

The data scene details of DFSAR of Chandrayaan-2 used in the mosaic of the South Pole for the figure 10.

Table 5 Data scene details used in the mosaic of the South Pole for Chandrayaan-2 data

Data ID	Date of acquisition	Azimuth and Range Resolutions (Meters)	look angle	Scene centre Coordinates (Lat, Long)	Spacecraft Altitude (Meters)
ch2_sar_ncxl_20191019t215745372_d_fp_d18	19-10-2019	10.80 & 19.98	26.0011	-85.70, -28.74	90508
ch2_sar_ncxl_20191022t065522035_d_fp_g26	22-10-2019	0.49 & 9.59	26.0001	-85.72, -59.41	97387
ch2_sar_ncxl_20191022t124900235_d_fp_g26	22-10-2019	0.49 & 9.59	25.99	-85.54, -63.85	96720
ch2_sar_ncxl_20191024t133923631_d_fp_gds	24-10-2019	0.57 & 9.59	26.001	-86.008, -102.82	85658
ch2_sar_ncxl_20191026t025014780_d_fp_d18	26-10-2019	0.52 & 9.59	26.001	-86.07, -131.55	102432
ch2_sar_ncxl_20191115t193611197_d_fp_d18	15-11-2019	0.49 & 9.59	26.0003	-85.35, -24.77	95841
ch2_sar_ncxl_20191021t091904787_d_fp_gds	21-10-2019	0.49 & 9.59	25.999	86.49, -51.05	97242
ch2_sar_ncxl_20191103t150253267_d_fp_d18	03-11-2019	0.59 & 9.59	26.000	-86.57, 132.15	89041
ch2_sar_ncxl_20191104t143620990_d_fp_d18	04-11-2019	0.58 & 9.59	26.002	-86.51, 120.98	86859
ch2_sar_ncxl_20191105t002515688_d_fp_gds	05-11-2019	0.58 & 9.59	25.99	-85.96, 119.23	87573
ch2_sar_ncxl_20191105t061840362_d_fp_d18	05-11-2019	0.58 & 9.59	25.99	-85.87, 115.55	88198
ch2_sar_ncxl_20191108t125103090_d_fp_d18	08-11-2019	0.59 & 9.59	26.001	-86.01, 50.56	90868
ch2_sar_ncxl_20191112t185801514_d_fp_d18	12-11-2019	0.58 & 9.59	26.0002	-85.66, 11.08	87511
ch2_sar_ncxl_20191023t122001838_d_fp_gds	23-10-2019	0.57 & 9.59	26.004	-84.83, -75.48	86780
ch2_sar_ncxl_20191103t205613651_d_fp_g26	03-11-2019	0.58 & 9.59	26.0024	-86.64, 129.40	87778
ch2_sar_ncxl_20191104t024936157_d_fp_g26	04-11-2019	0.58 & 9.59	26.000987	-86.58, 127.03	87094

The data scene details of DFSAR of Chandrayaan-2 used in the mosaic of the Nouth Pole for the figure 16.

Table 6 Data scenes details used in the mosaic of the North Pole for Chandrayaan-2 data

Data ID	Date of acquisition	Azimuth and Range Resolutions (Meters)	look angle	Scene centre Coordinates (Lat, Long)	Spacecraft Altitude (Meters)
ch2_sar_ncxl_20191026t113849791_d_fp_m65	26-10-2019	0.50 & 9.59	26.000499	87.57, -100.38	98194
ch2_sar_ncxl_20191103t120442214_d_fp_d18	03-11-2019	0.55 & 9.59	26.001475	87.85, 115.72	109978
ch2_sar_ncxl_20191103t175805919_d_fp_mad	03-11-2019	0.56 & 9.59	26.001832	87.84, 113.02	111405
ch2_sar_ncxl_20191105t150651511_d_fp_d18	05-11-2019	0.55 & 9.59	26.002280	87.66, 101.74	109495
ch2_sar_ncxl_20191108t213931684_d_fp_m65	08-11-2019	0.55 & 9.59	26.000272	88.20, 74.24	108860
ch2_sar_ncxl_20191111t122919492_d_fp_d18	11-11-2019	0.56 & 9.59	26.002133	87.80, 34.42	111695
ch2_sar_ncxl_20191112t100519040_d_fp_gds	12-11-2019	0.55 & 9.59	26.001229	87.86, 17.87	109567
ch2_sar_ncxl_20191102t043950913_d_fp_d18	02-11-2019	0.53 & 9.59	26.002499	87.91, 136.79	105240
ch2_sar_ncxl_20191009t132320814_d_fp_d18	09-10-2019	0.57 & 9.59	26.001190	84.26, 117.55	114020
ch2_sar_ncxl_20191012t160410765_d_fp_d18	12-10-2019	0.58 & 9.59	26.000105	88.29, 69.78	115115
ch2_sar_ncxl_20191012t215748426_d_fp_d18	12-10-2019	0.58 & 9.59	26.000289	88.32, 66.56	114685
ch2_sar_ncxl_20191014t190846230_d_fp_d18	14-10-2019	0.48 & 9.59	25.997859	87.73, 39.23	117994
ch2_sar_ncxl_20191017t115825864_d_fp_d18	17-10-2019	0.58 & 9.59	26.000811	87.506973, -14.519421	116072
ch2_sar_ncxl_20191019t011733461_d_fp_d18	19-10-2019	0.55 & 9.59	25.998984	87.586037, -34.181945	109500
ch2_sar_ncxl_20191022t213646453_d_fp_d18	22-10-2019	0.53 & 9.59	25.999746	87.860159, -80.426619	104200
ch2_sar_ncxl_20191101t105916773_d_fp_d18	01-11-2019	0.53 & 9.59	26.003334	87.747836, 145.764459	104008

ch2_sar_ncxl_20191106t144032517_d_fp_d18	06-11-2019	0.54 & 9.59	26.002042	87.942643, 98.568529	106446
ch2_sar_ncxl_20191107t161214271_d_fp_d18	07-11-2019	0.54 & 9.59	26.002902	88.130627, 89.910400	106331
ch2_sar_ncxl_20191108t095230000_d_fp_d18	08-11-2019	0.55 & 9.59	25.991862	88.006451, 82.219519	108535
ch2_sar_ncxl_20191108t154556810_d_fp_d18	08-11-2019	0.55 & 9.59	26.002017	88.008182, 79.774392	108992
ch2_sar_ncxl_20191109t151947658_d_fp_d18	09-11-2019	0.54 & 9.59	26.002091	88.161332, 67.066511	107827
ch2_sar_ncxl_20191109t211314716_d_fp_mad	09-11-2019	0.54 & 9.59	26.000353	88.122131, 64.201509	107514
ch2_sar_ncxl_20191113t212534045_d_fp_d18	13-11-2019	0.55 & 9.59	25.999351	87.425005, -11.574374	108860
ch2_sar_ncxl_20191115t104333906_d_fp_d18	15-11-2019	0.52 & 9.59	26.004897	87.710308, -33.925365	102898
ch2_sar_ncxl_20191115t223022448_d_fp_d18	15-11-2019	0.52 & 9.59	26.000199	87.937800, -43.783440	102291